

## Reverse bias degradation of CIGS solar cells

Bakker, N.J.

**DOI**

[10.4233/uuid:d2d035ff-40ff-4867-9f4a-3d11fe9c8c62](https://doi.org/10.4233/uuid:d2d035ff-40ff-4867-9f4a-3d11fe9c8c62)

**Publication date**

2023

**Document Version**

Final published version

**Citation (APA)**

Bakker, N. J. (2023). *Reverse bias degradation of CIGS solar cells*. [Dissertation (TU Delft), Delft University of Technology]. <https://doi.org/10.4233/uuid:d2d035ff-40ff-4867-9f4a-3d11fe9c8c62>

**Important note**

To cite this publication, please use the final published version (if applicable).  
Please check the document version above.

**Copyright**

Other than for strictly personal use, it is not permitted to download, forward or distribute the text or part of it, without the consent of the author(s) and/or copyright holder(s), unless the work is under an open content license such as Creative Commons.

**Takedown policy**

Please contact us and provide details if you believe this document breaches copyrights.  
We will remove access to the work immediately and investigate your claim.



# REVERSE BIAS DEGRADATION OF CIGS SOLAR CELLS

Klaas Bakker



# Reverse bias degradation of CIGS solar cells

## **Dissertation**

for the purpose of obtaining the degree of doctor  
at Delft University of Technology  
by the authority of the Rector Magnificus prof.dr.ir. T.H.J.J. van der Hagen  
chair of the Board for Doctorates  
to be defended publicly on  
14 September 2023 at 15:00 o'clock

## **By**

Nicolaas Jacobus Bakker  
Master of Engineering Science in Photovoltaic Engineering,  
The University of New South Wales, Australia  
born in Drechterland, The Netherlands



This dissertation has been approved by the promotor.

Prof. dr. A.W. Weeber

Prof. dr. M. Zeman

Copromotor

Dr. M.J. Theelen

Composition of the doctoral committee:

Rector Magnificus	chairman
Prof. dr. A.W. Weeber	Delft University of Technology, promotor
Prof. dr. M. Zeman	Delft University of Technology, promotor
Dr. M.J. Theelen	TNO partner in Solliance, copromotor

Independent members:

Prof.dr. J. Poortmans	KU Leuven / IMEC, Belgium
Dr. N. Barreau	U. Nantes, France
Em.prof.dr. W.C. Sinke	U. of Amsterdam
Prof.dr. L.D.A. Siebbeles	Delft University of Technology
Prof.dr.ir. O. Isabella	Delft University of Technology, reserve member

This work is supported by 'Netherlands Enterprise Agency' (RVO) and the Dutch Topteam Energy via the projects 'Performance and Electroluminescence Analysis on Reliability and Lifetime of Thin-Film Photovoltaics' with grant number TEUE116203 and "Building Integrated PhotoVoltaic Panels on Demand—in The Netherlands" under Grant TEID215005 and. Furthermore, the Early Research Program 'Sustainability & Reliability for solar and other (opto-) electronic thin-film devices' from TNO is acknowledged for funding.

Cover and layout design	Univorm, Nicky Vermeer
Printed by	Ridderprint
ISBN	978-94-6483-307-2





# Contents

## CHAPTER 1

**Introduction ..... 11**

1.1 Aim and outline of this dissertation ..... 14

1.2 Main contributions to the field ..... 15

## CHAPTER 2

**Experimental..... 19**

2.1 CIGS solar cells.....19

2.2 Characterization methods..... 23

## CHAPTER 3

**Reliability implications of partial shading on  
CIGS photovoltaic devices: A literature review ..... 31**

3.1 Introductions ..... 32

3.2 Origin of reverse bias..... 34

3.3 Different scenarios for shading tests ..... 37

3.4 Shading tests on modules..... 40

3.5 Thermoelectrical models on CIGS cells and modules..... 42

3.6 Reverse bias induced defects ..... 43

3.7 Reverse characteristic of single cells ..... 45

3.8 Non-permanent effects ..... 49

3.9 Conclusions ..... 50

3.10 Research topics for this dissertation ..... 50

3.11 Acknowledgments..... 51

## **CHAPTER 4**

---

### **Material property changes in defects caused by reverse bias exposure of CIGS solar cells..... 55**

4.1	Introduction .....	55
4.2	Materials and methods.....	56
4.3	Results and discussion.....	58
4.4	Discussion on propagation mechanism.....	66
4.5	Conclusions .....	67

## **CHAPTER 5**

---

### **Propagation mechanism of reverse bias induced defects in Cu(In,Ga)Se<sub>2</sub> solar cells ..... 71**

5.1	Introduction .....	72
5.2	Materials and methods.....	73
5.3	Experimental results .....	77
5.4	Discussion.....	88
5.5	Conclusions .....	96

## **CHAPTER 6**

---

### **How the absorber thickness influences the formation of reverse bias induced defects in CIGS solar cells ..... 101**

6.1	Introduction .....	101
6.2	Experimental.....	102
6.3	Results.....	106
6.4	Discussion.....	111
6.5	Conclusions .....	113

## **CHAPTER 7**

---

### **Determining the decomposition voltage of $\text{Cu}(\text{In}_{1-x}\text{Ga}_x)\text{Se}_2$ ..... 117**

7.1	Introduction .....	117
7.2	Experimental .....	118
7.3	Result and discussion.....	119
7.4	Summary.....	123

## **CHAPTER 8**

---

### **Fundamental mechanisms behind the reverse characteristic of $\text{Cu}(\text{In,Ga})\text{Se}_2$ solar cells..... 127**

8.1	Introduction .....	128
8.2	Experimental .....	129
8.3	Results and discussion.....	130
8.4	Conclusions .....	142

## **CHAPTER 9**

---

### **Conclusions and Outlook ..... 147**

9.1	Conclusions .....	147
9.2	Outlook .....	148

<b>References.....</b>	<b>151</b>
<b>Summary .....</b>	<b>157</b>
<b>Samenvatting .....</b>	<b>163</b>
<b>Appendix A .....</b>	<b>169</b>
<b>Appendix B .....</b>	<b>174</b>
<b>Appendix C .....</b>	<b>176</b>
<b>List of publications.....</b>	<b>178</b>
<b>Dankwoord.....</b>	<b>180</b>
<b>Curriculum Vitae.....</b>	<b>184</b>





**CHAPTER**

---

# Introduction





# Chapter 1

## Introduction

In the 21st century the photovoltaic (PV) industry has shown an explosive growth. Resulting, in March 2022, in a cumulative installed PV capacity exceeding 1 TWp [1]. The PV industry has learned to transfer increase in sales into a reduction in cost, this is expressed as the learning rate: “each time the cumulative PV module production doubled; the price went down by 25 % for the last 40 years” [2]. This learning rate is very impressive and much higher compared to other electricity supply technologies [3]. The cumulative PV module production used to determine the learning rate includes all commercially available PV technologies. Today roughly 95 % of the global annual PV production consists of wafer-based crystalline silicon (c-Si) solar cells [2], the remaining 5 % consists of thin-film solar cell technologies, including copper indium gallium selenide (CIGS) technology.

Thin-film solar cell technologies consume less material because the typical absorber thickness is between 1 and 3  $\mu\text{m}$ , much thinner than mainstream c-Si technology, which is about 150  $\mu\text{m}$  at the time of writing this dissertation. However, thin-film absorbers are not self-supporting and are therefore grown on a substrate or superstrate. The active material of a CIGS module is typically deposited on large glass plates ( $> 1 \text{ m}^2$ ), or long rolls of polyimide or steel foil. Currently the market for CIGS is moving towards products based on flexible substrates.

In Chapter 2 the detailed layer structure and the functionality of the different layers in a CIGS cell are described. Generally, a thin-film PV cell is built-up of at least an absorber material, that’s part of a light sensitive diode, sandwiched between two electrodes to extract the photo-generated current. To maximize absorption of light in the absorber material the electrode at the side where the light enters needs to be transparent, and is therefore made out of a transparent conductive oxide (TCO). Unfortunately, the transparency comes at the cost of reduced conductivity, resulting in relatively high lateral resistive losses in transporting the generated current. Since PV cells are high current and low voltage power generators, the area of the individual cells should be kept relatively small in order to be able to extract current without unacceptable lateral resistive losses.

Therefore, the large area coated with solar cell material is divided into smaller cells that are connected in series using an intricate interconnection scheme to create long and narrow cells. The series connection is created by scribes to selectively isolate and connect the top and bottom electrodes, and the design is called monolithically interconnection. Monolithically interconnected modules have, due to the high number of cells in series, a relative high voltage and low current output. An example of a typical thin-film module including a schematic representation of the monolithic interconnection scheme with the P1, P2, and P3 scribes is given in Figure 1-1. Furthermore, the insulating glass substrate is often used as an integral part of the module, in contrast to wafer-based modules that consist of larger individual cells that are electrically connected in series by wiring. In these modules the individual cells are packaged between two sheets of barrier material. Wafer-based module designs are not exclusively c-Si cells, it can also refer to modules that use large area thin-film PV cells, for example CIGS cells on a stainless steel substrate.

There is a big difference in the behavior of wafer-based and monolithically interconnected modules with respect to the tolerability of partly shading and reverse bias. When a small number of cells is shaded, these cells are forced to dissipate energy from the current generated by the non-shaded cells due to the electrical series connection. In a string of cells connected in series the current through all cells is equal, this will force the shaded cell (that generated less current) to operate at a negative voltage. This negative voltage is often referred to as reverse bias (voltage), and is explained in more detail in Chapter 3. Most solar cells are not designed to operate at reverse bias conditions, and during partial shading the dissipated power can locally be many times higher than the designed power during normal forward bias operation. This can lead to hotspots and degradation of solar cells [4]. The most common method to mitigate reverse bias exposure of solar cells is to include bypass diodes in the module. For wafer-based modules where the cells are individually connected, the integration of bypass diodes is relatively simple and standard practice. Therefore, this type of modules is much more resilient against damage as a result of partial shading and reverse bias compared to the monolithically interconnected modules.

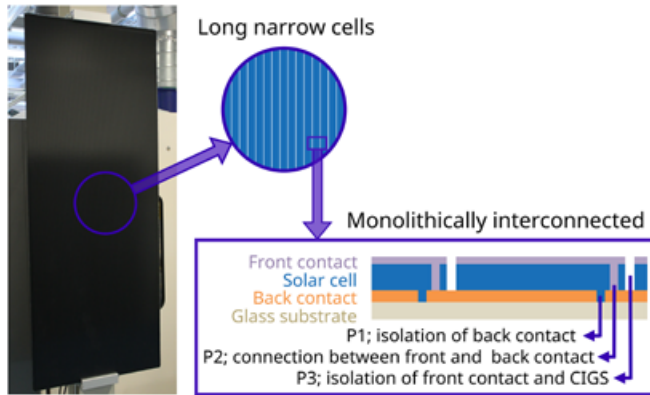


**Figure 1-1:** Picture of a monolithically interconnected module and a schematic explanation of the interconnection scheme. On the left is a picture of a commercially available monolithically interconnected module in the process hall at the TNO - partner in Solliance facilities in Eindhoven. The purple circle points to a schematic showing the direction of the long and narrow cells. The square in this schematic points to a schematic cross section showing the monolithic interconnection scheme with the P1, P2 and P3 scribes.

Monolithically interconnected modules make up the majority of the commercial thin-film PV modules, and they offer no protection of the individual cells against reverse bias. Partial shading is a major reliability concern that is recognized by manufacturers of monolithic modules. First Solar (CdTe) published a white paper [5] on the topic in which they describe allowed and not allowed shading scenarios. In the literature review of Chapter 3 the effect of partial shading of commercial CIGS modules is described. Partial shading of CIGS modules can lead to reverse bias induced defects, often referred to as wormlike defects. The name wormlike defects comes from trails of damaged material that have a distinct visual appearance. The size of the trails can vary from less than 0.1 mm to a network of tens of centimeters, meandering and branching to cover several square centimeters of the affected CIGS cell. The trails consist of small local defects that act as shunts and permanently reduce the power output of a PV module.

The main goal of this dissertation is to create a more fundamental understanding of the reverse bias behavior of CIGS solar cells and the formation of wormlike defects that are the result of reverse bias exposure on CIGS solar cells.

## 1.1 Aim and outline of this dissertation

The main aim is to gain knowledge that can be used to increase the stability of CIGS modules against partial shading with limited or no added cost. This dissertation starts with an experimental section in Chapter 2, which describes the physics of the CIGS solar cells and the fabrication methods and characterization techniques used in this dissertation. The origin of reverse bias in a PV module is described in detail in Chapter 3. This chapter also gives an overview of the literature that was published on the topic of partial shading and reverse bias of CIGS cells and modules. Based on this literature review the specific research topics of this dissertation are formulated at the end of this chapter. In Chapter 4 the morphology and composition of wormlike defects was studied in depth. Based on observed changes in material properties, a propagation model is proposed for the wormlike defects. This model explains why the hotspot that forms the wormlike defects is not stationary but moves over the cell area. This model is extended in Chapter 5 with the influence of the electric field on the propagation of the wormlike defects. The initial formation of wormlike defects and the role of the electric field on the formation is described in Chapter 6. The results of Chapter 5 and Chapter 6 show that there is a large influence of the electric field in both the propagation and formation of wormlike defects in CIGS solar cells. Therefore, an experiment was designed in Chapter 7 to study the influence of the electric field on the CIGS absorber only. In this chapter it is shown that the CIGS absorber decomposes under the influence of an electric field. The electrical behavior of CIGS cells at reverse bias voltages is studied in Chapter 8. This behavior is characterized by a sharp rise in current, comparable to the characteristics of an avalanche or Zener diode. The mechanism behind this sharp increase in current is best described by the Fowler–Nordheim tunneling mechanism. Finally in Chapter 9 the conclusions of the work presented in this dissertation are drawn and recommendations for future work are made.

## 1.2 Main contributions to the field

This dissertation has contributed to the field of CIGS PV technology in the following way:

- At the start of this work a detailed literature review was made on the impact of partial shading and reverse bias on CIGS solar cells and modules. This includes a generic description of the wormlike defects that are formed in the CIGS absorber as a result of exposure to reverse bias.
- The propagation mechanism of wormlike defects was explained by a comprehensive study of the propagation behavior of wormlike defects during reverse bias. This study resulted in a model that explains the propagation.
- The influence of the internal electric field in CIGS cells on both the propagation mechanism and the formation of wormlike defects was studied. The propagation of wormlike defects can be significantly reduced by reducing the resistance of the front electrode. Furthermore, it was shown that the formation of wormlike defects is a voltage driven process.
- For the first time it was shown that CIGS decomposes into copper- poor ordered vacancy complexes (OVC) and conductive  $\text{Cu}_2\text{Se}$  under the influence of an electric field.
- It was shown that Fowler–Nordheim tunneling is responsible for the large increase in current at high reverse voltages. The tunneling barrier is located in the complex stack between the AZO and the quasi-neutral bulk CIGS material. This insight improved the understanding of the fundamental mechanisms governing the electrical behavior of CIGS solar cells under reverse bias condition.





**CHAPTER**

# Experimental





## Chapter 2

# Experimental

In this chapter the experimental techniques used for the R&D work in this dissertation are described. All solar cells that were used for this research were fabricated at the TNO partner in Solliance facilities in Eindhoven or (partly) at the Institut des Matériaux Jean Rouxel of the Université de Nantes in Nantes, France. Since different deposition tools and process parameters were used for the samples described in the different chapters, only general information is given in this chapter. In the first section the functionality and the applied fabrication methods of the individual layers in the CIGS solar cells are described. In the next section the main techniques for characterizing the layers and samples are described.

### 2.1 CIGS solar cells

All the experiments were performed on non-encapsulated solar cells. This section is therefore limited to the solar cell only and does not include interconnection or packaging. Only methods and layers applied to cells in this dissertation are described. Since, materials, deposition technologies and layer thicknesses may vary between manufacturers and institutes, a direct comparison with results from others and generalization of the results presented in this dissertation requires more detailed research.

Figure 2-1 shows a cross section of a CIGS solar cell. All the individual layers starting from the sunny side up to, and including, the substrate are described in the next section.

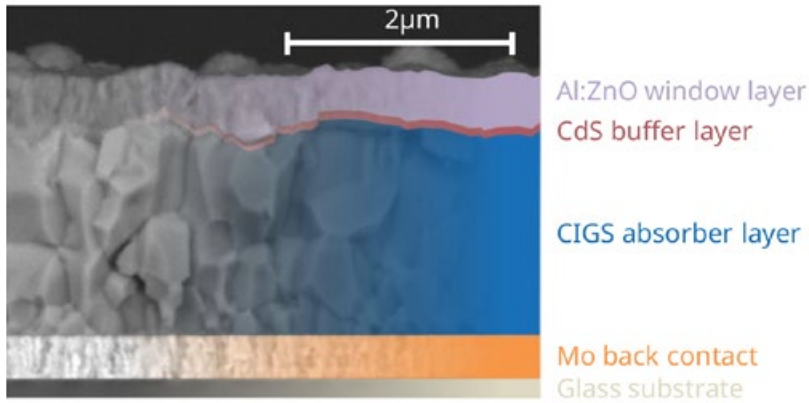


**Figure 2-1:** Cross-sectional SEM picture of CIGS cell showing the layer structure. (courtesy of dr. Marcel Simor, TNO - partner in Solliance)

### 1. Window layer

The first layer at which the light enters when illuminating a solar cell is called the window layer. This layer should have high transparency to allow the light to pass through and at the same time it should be conductive to extract and laterally transport the electric current generated in the solar cell. Therefore, the material properties of the window layer are a complex balance between good conductivity and high transparency. A thicker layer is more conductive, but results in more parasitic absorption. In the traditional monolithically interconnected CIGS modules no additional conductive layers to improve lateral transport are added therefore relatively thick window layers are applied to reduce resistive losses. The cells used in Chapter 4, Chapter 5 and Chapter 7 are designed to mimic the cells in such a module and therefore have a thick (1 to 2 μm) window layer. However, the cells used in Chapter 6 have a much thinner ( $\pm 200$  nm) window layer and the current collection is improved by adding a metal grid on top of the window layer.

The most common material used for the window layer is a transparent conductive oxide (TCO). For the cells used in this dissertation a combination of intrinsic zinc oxide (*i*-ZnO) and aluminum doped zinc-oxide (Al:ZnO or AZO) were applied. Both layers were deposited by sputtering. The main function of the thin ( $\pm 50$  nm) highly resistive *i*-ZnO is to prevent the formation of shunt pathways of the CIGS absorber with the low resistive AZO layer.

## 2. Buffer layer

The buffer layer is an n-type semiconductor layer between the window layer and the CIGS absorber. Applying this n-type layer on top of the p-type CIGS absorber creates the p-n heterojunction. For the cells used in this dissertation cadmium sulfide (CdS) was used as the n-type semiconductor. The thin ( $\pm 50$  nm) CdS layer was applied by chemical bath deposition (CBD).

## 3. Absorber layer

Light that has passed the window and buffer layers can be absorbed in the absorber layer. The CIGS absorber is a polycrystalline p-type compound semiconductor with composition  $\text{Cu}(\text{In}_{1-x}\text{Ga}_x)\text{Se}_2$ , that belongs to the chalcopyrite family, named after the mineral  $\text{CuFeS}_2$ . By varying the indium and gallium ratio the bandgap can be tuned between 1 (CuInSe<sub>2</sub>) and 1.71 eV (CuGaSe<sub>2</sub>) [6]. CIGS is a direct bandgap semiconductor and therefore has a high optical absorptance for photons with energy larger than the width of the bandgap and it enables the application of very thin ( $< 3\mu\text{m}$ ) layers. The CIGS absorbers used in this research were made by co-evaporation. For this process the metals (Cu, In and Ga) are simultaneously evaporated in a selenium atmosphere, while the substrates was held at 550 °C. The gallium content for the cells used, expressed as Ga/(Ga+In) or GGI is between 0.25 and 0.35. This gives a bandgap of approximately 1.15 to 1.25 eV and is around the optimum bandgap for single junction solar cells. During the co-evaporation process a natural grading in the GGI is created, this results in an electronic gradient comparable to the back surface field in c-Si solar cells, an example of the GGI profile is given in Figure 2-2.

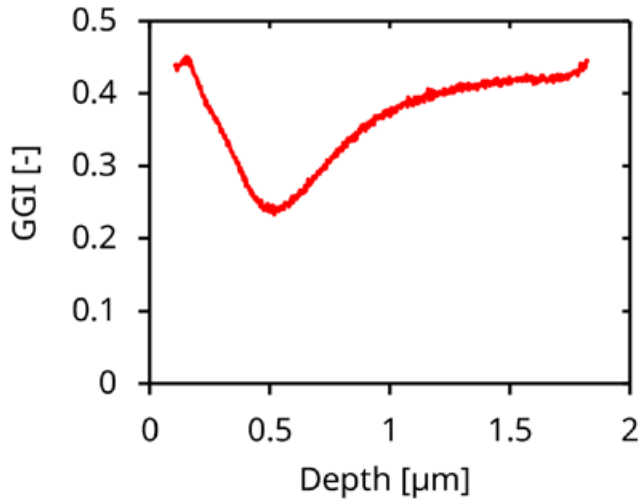


**Figure 2-2:** GGI profile of CIGS solar cell. (courtesy of dr. Marcel Simor, TNO - partner in Solliance).

#### 4. Back contact

The function of the back contact is to extract and transport the positive charges generated in the CIGS absorber. Molybdenum (Mo) is often used because it has good compatibility with the high temperature CIGS deposition process, and has an appropriate work function. None of the metals react with Mo, and during the deposition of the CIGS a thin intermediate layer of  $\text{MoSe}_2$  is formed that acts as an ohmic contact with the CIGS. Furthermore, molybdenum allows for elements to diffuse from the glass substrate into the CIGS absorber. Most of these elements, like the alkali ions which passivate grain boundaries, are beneficial for the CIGS solar cell efficiency. The Mo layer was sputtered onto the substrate with a typical thickness around 400 nm.

## 5. Substrate

The substrate is the start of the fabrication process, all layers are deposited on this substrate. The most common material used is soda lime glass (SLG). The substrate has to withstand the temperatures used during the subsequent deposition steps, and to minimize mechanical stresses it should also have a thermal expansion coefficient similar to CIGS. Soda lime glass is also used as a source of alkali ions ( $\text{Na}^+ + \text{K}^+$ ) for the cells in this dissertation, as these ions are known to be beneficial for the efficiency of CIGS solar cells.

## 2.2 Characterization methods

### 2.2.1 Electrical characterization

The most common electrical measurement for PV devices is the current voltage ( $IV$ ) measurement where a voltage sweep is applied and the current is measured. In order to compare devices of different area both current and resistance are normalized to the area of the solar cell, resulting in a current density  $J$  in  $\text{mA}/\text{cm}^2$  and resistance  $R$  in  $\Omega \times \text{cm}^2$ . The  $JV$  curve of a solar cell can be measured both under illumination and in the dark. Measuring the  $JV$  under illumination gives information on the solar cell during operation. Measuring it in the dark gives additional information (like diode quality), and also resembles the fully shaded condition. As an illumination source typically a solar simulator is used. A solar simulator simulates the sun's light on earth. The standardized (ISO 9845-1) illumination is level  $1000 \text{ W}/\text{m}^2$  with a spectrum close to AM1.5G, and the standard temperature is  $25^\circ\text{C}$ . However, for this dissertation also different illumination conditions and temperatures were used. These are described in the appropriate chapters.

When performing a  $JV$  measurement the voltage over the solar cell is swept and the resulting current is recorded. The  $JV$  curve can be measured in three quadrants, where the solar cell is either generating or dissipating energy. Therefore, a source measure unit (SMU) is used to record the  $JV$  curve. A SMU has a built-in power source that can generate and dissipate power.

Figure 2-3 shows a typical  $JV$  curve of a solar cell. The three quadrants of operation are marked with roman numerals. In Quadrants I and III the product of current and voltage is positive hence the solar cell is dissipating

energy. In the fourth quadrant the power is negative and the solar cell is generating power. Solar cells are designed as power generators and to operate at a positive voltage and negative current (quadrant IV).

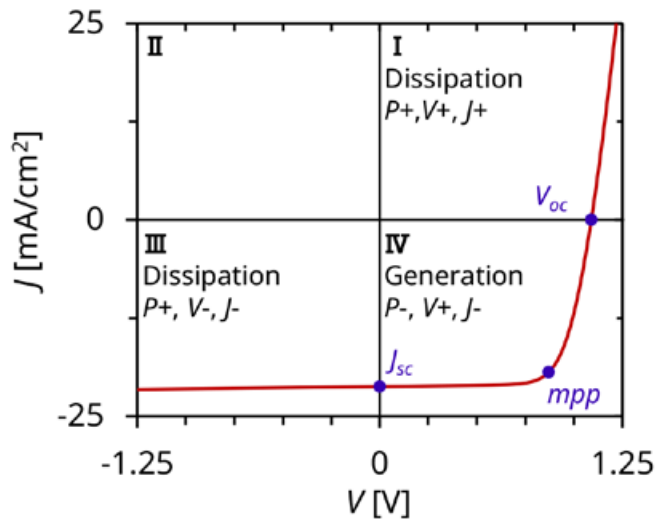


**Figure 2-3:** Illuminated  $JV$  curve of a solar cell showing the three quadrants in which the solar cell operates. On the x-axis the voltage is plotted, on the y-axis the current density is plotted.

The electrical behavior of a solar cell under illumination is best described by using the equivalent electrical circuit shown in Figure 2-3.

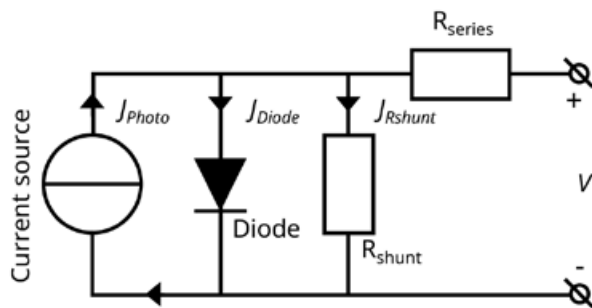


**Figure 2-4:** Equivalent electrical circuit of a solar cell.

Figure 2-4 shows the equivalent electrical circuit of a solar cell without any load connected to the output terminals. The current source represents the light-generated current or photocurrent  $J_{photo}$ . In general this current depends linearly on the illumination intensity. The photo current flows, for the situation depicted in Figure 2-4, through the diode  $J_{diode}$  and the shunt resistance  $J_{Rshunt}$ . For good solar cells the impact of the shunt resistance is minimal and the voltage is dictated by the voltage drop over the diode. Since there is no load connected to the solar cell there will be no current through the series resistance and the voltage drop over the diode will be the voltage over the solar cell. This voltage is called the open circuit voltage  $V_{oc}$ . In the  $JV$  graph of Figure 2-3 the  $V_{oc}$  is the intercept with the x-axis where the current is zero. The intercept with the y-axis represents the situation in which the solar cell is short circuited. The current corresponding to this situation is therefore called the short circuit current  $J_{sc}$  and is for good solar cells close to the light generated current. When applying different voltages the current is dictated by a combination of the diode and the series and shunt resistance and can be described by the following equation:

$$J = -J_{Photo} + J_0 \exp \left[ \frac{q(V - J R_{series})}{nkT} \right] + \frac{(V - J R_{series})}{R_{shunt}} \quad (2-1)$$

Where the  $J$  without subscript is the current at the terminals of the solar cell and  $V$  is the voltage applied to these terminals. Furthermore,  $J_0$  and  $n$  are the saturation current and ideality factor of the diode, respectively.  $T$  is the temperature,  $q$  is the elementary charge,  $k$  is the Boltzmann constant,  $R_{series}$  is the series resistance and  $R_{shunt}$  is the shunt resistance. Note that in the first term the photocurrent has a negative sign as this is the element that generates the current, in contrast to the currents in the second and third term (the diode and the shunt resistor) which are elements that dissipate energy. Equation 2-1 assumes the superposition principle, this means that the whole  $JV$  graph shifts with the photocurrent. The superposition principle does not hold for CIGS solar cells. Several reasons that could be responsible for this are:

- Voltage dependent collection of photocurrent.
- Light dependent diode and resistance parameters
- Non-uniform series resistance



Since a solar cell is designed to generate energy there is one more important point on the  $JV$  curve. This is the point at which the energy delivered by the solar cell is maximum and is referred to as, the maximum power point (mpp). This maximum power point is used to calculate the efficiency of the solar cell and the fill factor (FF). The efficiency of a solar cell is the ratio between incoming power from the incident light and the electrical output power. The FF is the ratio between the maximum power point and the product of  $V_{oc}$  and  $J_{sc}$ . The FF is mainly influenced by resistive losses (both series and shunt) and the quality of the diode, it also depends on  $V_{oc}$ .

The reverse  $JV$  characteristic is the part of the  $JV$  curve in quadrant III, where the cell is dissipating energy. The principle of measuring the reverse  $JV$  curve is the same as for the other quadrants, a voltage is swept over the cell and the resulting current is recorded. However, the behavior of a solar cell in reverse condition depends on the solar cell technology and detailed structure of the cells. Before the start of this doctoral research, the reverse characteristics of CIGS solar cells were not yet thoroughly described. However, to enhance the energy output of PV systems with CIGS modules it is important to understand the (electrical) behavior of shaded cells under partial shading conditions. More information on the reverse current behavior of CIGS solar cells is described in the literature review (Chapter 3).

## 2.2.2 Raman Spectroscopy

Raman spectroscopy is a non-destructive characterization technique that uses the principle of inelastic scattering. Inelastic scattering is a process in which the energy of an incident photon is not conserved. This means that the incident light from the Raman excitation laser interacts with vibrational, rotational or other modes present in the material, resulting in a shift of frequency of the scattered light. Therefore, a Raman spectrum has several distinct peaks that can act as a fingerprint for the material. For CIGS the peaks can be attributed to vibration modes of atomic bonds and can be used for instance to determine the gallium concentration. Since CIGS is an excellent absorber for the typical excitation laser wavelengths the penetration depth is limited, and depending on the excitation wavelength is in the order of 100 nm [7]. The excitation wavelength used in this dissertation to study the CIGS absorber is 632 nm, since this wavelength

has no interaction with the window and buffer layers on top of the CIGS absorber, because the ZnO and CdS are transparent for this wavelength.

### 2.2.3 Photoluminescence Measurements

The luminescence of a semiconductor is the result of band-to-band radiative recombination of carriers. In case of photoluminescence (PL) the carriers are generated by light. Two different types of PL were used for this dissertation: spatially and spectrally resolved PL. With spatially resolved PL a 2D image of the solar cell's quality is created based on the intensity of the PL signal. The PL signal shows an exponential dependence on the voltage as a result of the splitting of the quasi Fermi energies. Therefore, the PL image gives information on the local  $V_{oc}$ . PL imaging can be used to extract local solar cell parameters and can also give information on local series and shunt resistance if used in combination with different electrical biases.

For spectrally resolved PL, the whole emission spectrum is recorded over a larger spectral range. This spectrum gives information on the bandgap of the material, but can also reveal defect levels since point defects such as interstitials and antisites affect the position of the peaks [8].



CHAPTER

# Reliability implications of partial shading on CIGS photovoltaic devices: A literature review

This chapter is based on the following publication:

K. Bakker, A. Weeber, and M. Theelen, "Reliability implications of partial shading on CIGS photovoltaic devices: A literature review," *J. Mater. Res.*, vol. 34, no. 24, pp. 3977–3987, Dec. 2019, doi: 10.1557/jmr.2019.373.

## Chapter 3

# Reliability implications of partial shading on CIGS photovoltaic devices: A literature review

## GRAPHICAL ABSTRACT:

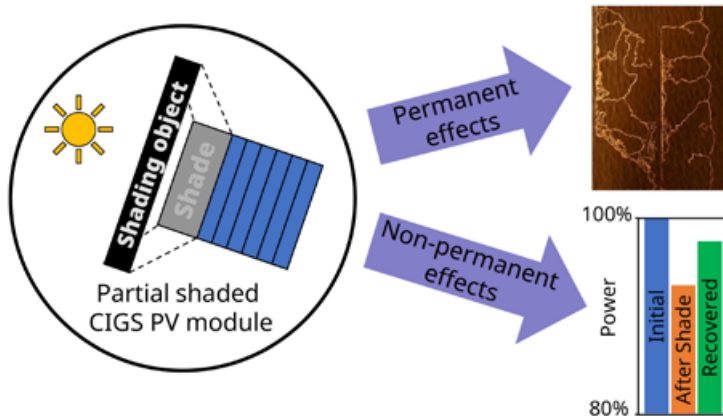


**Figure 3-1:** Graphical abstract as published with the online version of ref. [9].

**ABSTRACT:** Partial shading of  $\text{Cu(In,Ga)(Se,S)}_2$  (CIGS) photovoltaic (PV) modules is getting more attention, as is witnessed by the increase in publications on this topic in recent years. This review will give an overview of shading tests executed on CIGS modules and focuses on the more fundamental aspects that are often studied on cells. Generally, CIGS modules display very attractive performance under predictable row-to-row shading. However, potential damage could occur under nonoptimal shading orientations: module output after shading tests could reduce due to the formation of local shunts, often called wormlike defects.

The influence of many factors on the formation of these defects, including the internal currents and voltages and the shape and intensity of the shade, will be discussed. This review allows an increased insight in the degradation mechanisms caused by partial shading, which would ultimately lead to the introduction of more shade-tolerant CIGS PV products in the future.

### 3.1 Introductions

Photovoltaic (PV)-based electricity is playing an increasing role as a renewable energy source. Actually, in 2017, the total installed PV capacity was over 400 GWp [10], showing a rapid increase due to a dramatical decrease in cost and increase of efficiency. One of the PV technologies displaying rapid growth are devices based on thin-film  $\text{Cu(In,Ga)(Se,S)}_2$  (CIGS) absorbers. These devices contain absorber materials with a direct band gap, therefore allowing solar cell stacks with a thickness of only several microns. Currently, many studies are even working toward solar cells with submicron absorber thicknesses [11]. Moreover, at the moment of writing this dissertation record efficiencies up to 23.35 % [12] have been reported.

Key advantages of CIGS compared to, e.g., crystalline silicon devices include its attractive temperature dependency, a short energy payback time, and advantageous cost projections: due to the reduced amount of required material for thin-film solar cells and the possibility to use low-cost manufacturing techniques, a reduction of costs due to the further scale-up is expected [13].

Moreover, the possibility to deposit fully black PV devices on a large range of substrates, including glass, plastics, and metal foils, allows the usage of the CIGS technology in a large number of new applications: these include integration into vehicles, outer space astronautics, and portable devices, as well as building integrated PV (BIPV) [13].

A part of the attractive properties of CIGS has an effect on the levelized cost of electricity (LCOE), which is the dominant parameter for successful large-scale market introduction. Lifetime and degradation rates are important factors that influence the LCOE. These factors are, for the LCOE calculations of a PV system, usually based on the warrantee provided by the manufacturer [14]. Therefore, PV manufacturers, and their customers, need to be able to accurately predict the lifetime of their products. This is especially important due to the attractiveness of CIGS PV devices for

building and product integration, which can lead to an increase in the exposure to uncontrollable stress like partial shading.

Stress loads during partial shading events are 2-fold. First, the redistribution of (electric) power, within the PV module, causes the regions to heat up while other regions cool down. This type of stress is predictable and comparable in nature with other PV technologies. The second stress factor is the influence of the reverse bias potential on the solar cell, which can result in the formation of wormlike defects that are typical for the CIGS technology.

The impact of partial shading strongly depends on the design of the module that is getting exposed. Commercial CIGS modules can be divided into two classes:

- (i) Monolithically interconnected modules, consisting of long, small cells (e.g.,  $1200 \times 5 \text{ mm}^2$ ) connected in series by a (laser) interconnection process on an insulating substrate. This approach is chosen for most rigid commercial modules. These modules generally do not contain any mitigation measures to protect the individual cells from any negative effects of partial shading.
- (ii) Modules made up of separated large cells with a current collecting grid in either series or parallel connection. This approach is used by various producers of flexible modules and is in a design very similar to crystalline silicon-based PV modules. It allows the use of bypass diodes, so the impact of partial shading can easily be minimized. However, incorporation of bypass diodes in a module comes with a trade-off between added cost and improved electric yield.

The monolithically interconnected modules generally maintain a higher output power when partly shaded [15], especially when it comes to predictable row-to-row shading [16]. In that case, the loss in output power is lower in systems with monolithically integrated modules having vertically oriented narrow cells compared to systems with modules having separated large cells.

However, the reliability impact of partial shading and reverse bias on CIGS is a little-studied subject. From 2015, this topic has gained interest; one of the many reasons could be the announced change in the IEC test protocol [17]. The 2016 version of the IEC 61215 has more stringent



requirements on shade tolerability compared to the IEC 61646 which it is replacing. Another reason why this topic has gained interest in recent years is that the damage done by partial shading is limited when evaluated at standard test conditions. More recent publications revealed that the impact of degradation due to shading effects becomes more pronounced when the degraded module is measured at lower light intensities compared to standard test conditions [18,19]. The low light performance greatly influences the performance ratio (PR) of a PV system [19].

### 3.2 Origin of reverse bias

Upon shading, local shunts are formed in regions that were exposed to a reverse bias voltage. To explain the origin of the reverse bias, the reverse bias behavior of a single cell will be described first. Figures 3-2(a) and 3-2(b) show the equivalent circuit of a CIGS solar cell and the graphical representation of the position of one cell in a string of cells within a module, respectively. The light-generated current (blue) varies linearly with light intensity, while the dark current (orange) is the sum of the diode current and the parasitic current through the shunt resistance. The combined contribution of the photo ( $J_{Photo}$ ) and dark ( $J_{Dark}$ ) current dominates the  $JV$  curve at positive voltages, as can be seen in the  $JV$  graph of Figure 3-3. At negative voltages (reverse bias), there is a third contribution [20] that, besides the shunt resistance, dominates the  $JV$  curve, indicated with the green box named reverse bias current ( $J_{Reverse-Bias}$ ) in Figure 3-2(a). For CIGS solar cells, this element is responsible for the rapid increase in current at negative voltages. The onset of this increase is the transition voltage ( $V_{tr}$ ) and is indicated with a purple dot in the  $JV$  curves in Figure 3-3. The transition voltage is an indication of the voltage at which the solar cell transits from an isolating nature to a conducting nature. The reverse characteristic, which is the  $JV$  curve at negative voltages, is dominated by the transition and depends strongly on both temperature and illumination. It can be influenced by many parameters which will be discussed in Chapter 3.7. For better readability, all current and voltage values in this chapter will be treated as absolute numbers, e.g., a change in the transition voltage from 3 to 2 V will be called a reduction of  $V_{tr}$ .

The reverse characteristics of the individual cells in a module determine the internal distribution of voltage and current because a module consists

of a string of series connected solar cells. For the example given in Figure 3-4, shading is simulated in one cell in a string of ten. The purple dashed line gives the electrical condition at the maximum power point of the constructed  $JV$  with nine unshaded and one fully shaded cell. A negative power means that the device is generating energy, while a positive power implies that the device is dissipating energy. Due to the series connection of all cells, the current must be equal in all cells. When the constructed module is operating at the current indicated by the purple dashed line the constructed module is still delivering energy through the external load (negative power in the graph). This energy is supplied by the nine unshaded cells, and the shaded cell is forced to operate at a negative voltage, thus dissipating the majority of the energy generated by the nine unshaded cells. The magnitude of the dissipation can be altered when the reverse bias characteristic of the cell can be influenced.

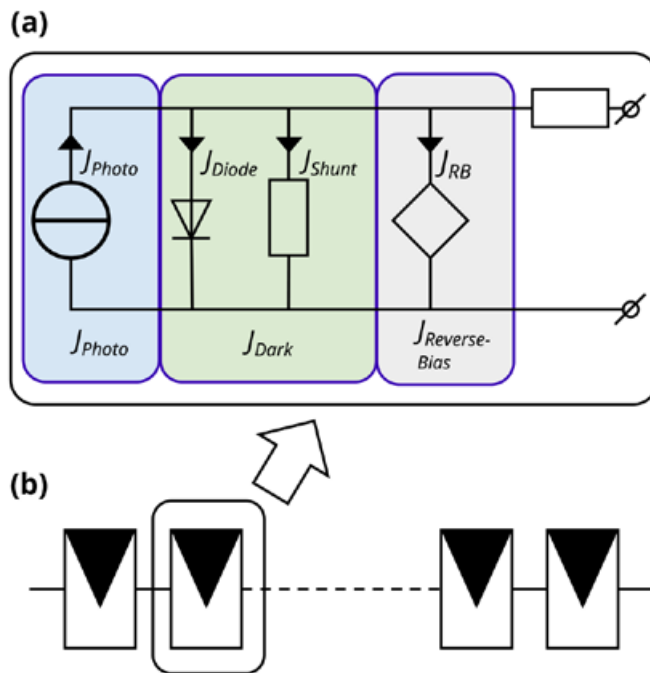


**Figure 3-2:** (a) Equivalent circuit of single cell and (b) representation of this cell in a string of cells as found in a PV module.

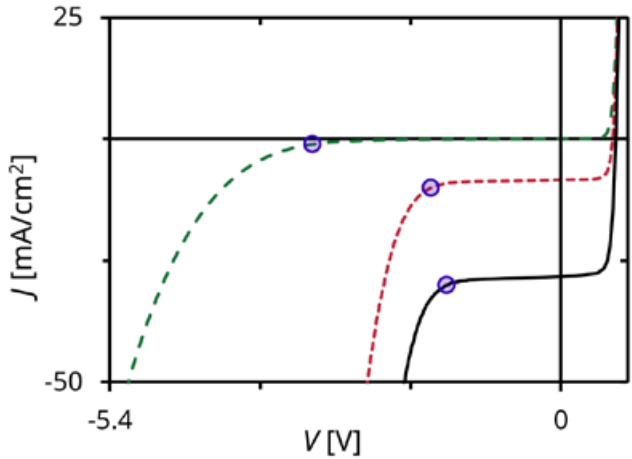


**Figure 3-3:**  $JV$  characteristic at different illumination intensities of a single cell. The black solid, red dotted, and green dashed lines represent 1 sun, 0.3 sun, and dark conditions, respectively. The transition voltage ( $V_{tr}$ ) is in each curve marked with a purple dot. Measurements performed on a standard cell, fabricated, and measured at the facilities of TNO partner in Solliance in Eindhoven.

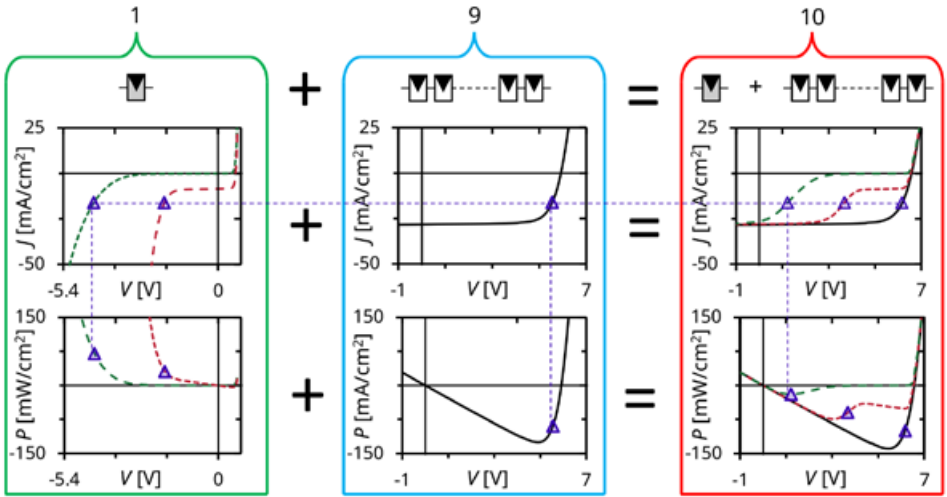


**Figure 3-4:** Constructed  $JV$  curve representing a module with 9 unshaded cells in series with 1 shaded cell. The graphs at the top are  $JV$  curves and the graphs at the bottom are  $PV$  curves. On the left the  $JV$  and  $PV$  curves are

plotted of 1 cell at different illumination intensities, the red dotted and green dashed lines represent respectively 0.3 sun and dark conditions. The  $JV$  and  $PV$  graphs in the middle are constructed from a 1 sun illuminated curve; here, the voltage is multiplied by 9 to get the equivalent  $JV$  curve of 9 unshaded cells in series. The graphs on the right are the sum of the graphs of the partly shaded cell and the nine unshaded cells together with (black) an unshaded 10 cell module. The purple symbols represent operating points based on the maximum power point current of the constructed module with 1 dark and 9 illuminated cells. The construction is based on the  $JV$  measurements from Figure 3-3.

### 3.3 Different scenarios for shading tests

In the field, shading can have any arbitrary form or intensity. Since not every thinkable shadow can be tested, Dongaokar *et al.* [21] introduced several shading scenarios for testing partial shading in monolithically interconnected thin-film modules. The layouts of the shading masks for these scenarios are depicted in Figure 3-5. Almost all reported shading tests can be categorized with these mask layouts, except for diagonal shading or shades that mimic a human body.

Besides the shape of the shading mask, also the opacity of the shading mask is an important parameter. Sometimes, a less opaque mask is used to simulate more realistic conditions: a shadow cast by a distant object, during clear sky conditions, blocks approximately 90 % of the incident light. Furthermore, shading tests are always executed under an electrical load or at short circuit conditions. Internal currents will flow as a result of externally extracted current from a partially shaded module, which causes internal power flow in the device under test. This can be large enough to cause permanent damage. At open circuit conditions, no current and power is drawn from the device, so no internal power flow is present.

Local differences in operating parameters are expected for each of the shading scenarios, which are listed in Table 3-1. Scenario 1 represents the normal operating condition with no shade. In case of symmetric shading (scenario 2), power generation of each cell is reduced equally and current and voltage in the shaded regions are uniformly reduced. In the third scenario (asymmetric shading), electrical energy is dissipated in the

shaded region because the photo-generated current is forced through the shaded cells. This results in a negative (or reverse) operating voltage of the shaded cells. During typical shading (scenario 4), an additional effect of unequal current distribution acts on the top of the stresses in scenarios 2 and 3. Since the effects are strongest when combined with reverse bias conditions, most shading tests are performed with  $L_{sh} \ll W_{sh}$ , and this is, unless otherwise stated, the operating condition when referring to the “typical” condition. An example of the temperature distribution for the typical scenario on a module during a field test can be seen in Figure 3-6.

**Table 3-1:** Expected changes in local operating parameters for the different shading conditions. Parameters are based on the authors’ interpretation of Refs. [20,22,23].

Scenario	region	Current	Voltage	Temperature
No shade	Illuminated	Normal	Positive	Normal
Symmetric	Illuminated	Normal	Positive	Normal
Symmetric	Shaded	Small	Positive	Cooler
Asymmetric	Illuminated	Normal	Positive	Normal
Asymmetric	Shaded	Normal	Negative	Normal
Typical ( $L_{sh} \ll W_{sh}$ )	Full cell illuminated	Normal	Positive	Normal
Typical ( $L_{sh} \ll W_{sh}$ )	Partial cell illuminated	Higher	Negative	Higher
Typical ( $L_{sh} \ll W_{sh}$ )	Partial cell shaded	Lower	Negative	Lower

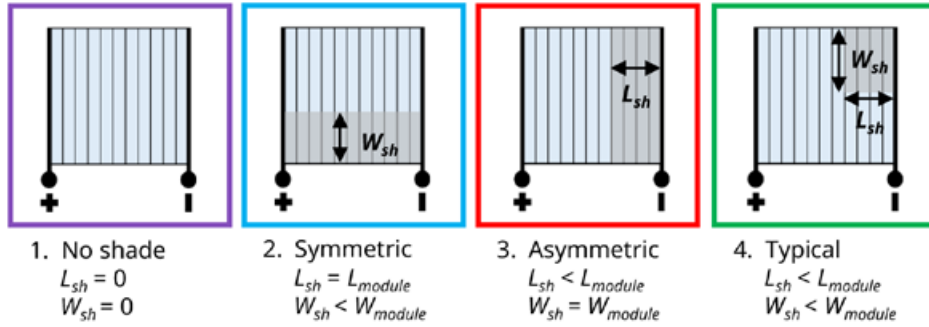


**Figure 3-5:** Different shading scenarios as introduced by Donaonkar *et al.* [21].

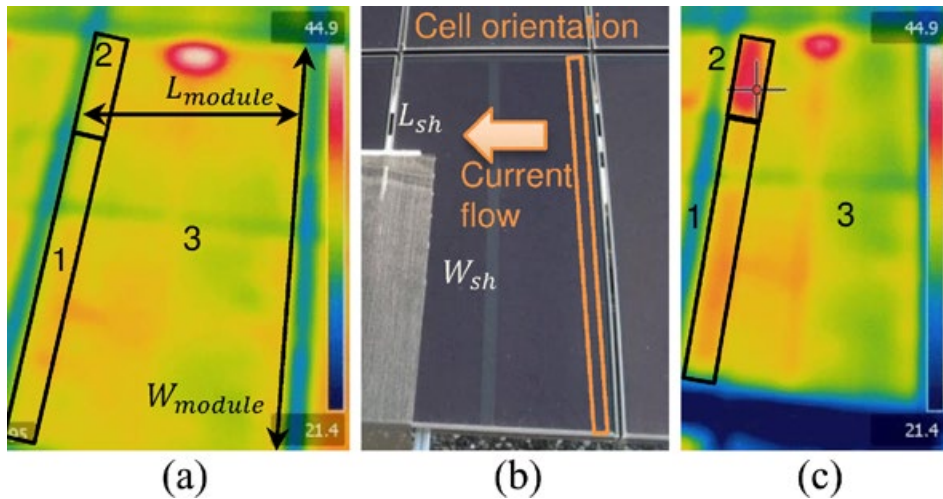


**Figure 3-6:** Outdoor measurements of a partially shaded CIGS (Shell Eclipse-80) module. **(a)** IR picture of module under normal operating condition. The hotspot on top of the module is due to the connectors that caused local heating. **(b)** Optical picture of module during shading test, with indications of current flow and cell orientation. **(c)** IR picture directly after the shading test. In **(a)** and **(c)** the regions of interest are numbered and indicated. A partly transparent shading mask was applied on region 1. The nonshaded region (region 2) of the shaded cells exhibit elevated temperatures due to the shading experiment. (Reprinted with permission from Ref. [21], © 2013 IEEE.)

### 3.4 Shading tests on modules

Several studies have been published on shading tests performed on monolithically interconnected CIGS modules. A list of them can be found in Table A-1 in Appendix A. Comparing results presented in the existing literature is challenging due to the following reasons:

- (i) Lack of uniformity in measurement conditions.
- (ii) Most sources report on tests executed on only one module or on a comparison of single modules from different types.
- (iii) Module manufacturers and types are often anonymized.
- (iv) Changes in efficiency and other electrical parameters are not always mentioned.
- (v) Large effect of metastabilities and pre-conditioning on module performance numbering alignment [17]. It is known that light soaking, electrical biases, and module temperature can temporarily influence the module performance [24]. Therefore, separation of the permanent effects of the partial shading tests and the temporary effects, which are often independent of the partial shading, is very complicated.

Besides the challenges, the main observation is that after shading tests, modules displayed a reduced efficiency, which is accompanied by the formation of local shunts. In all publications from 2015 till present (Table A-1), local shunts are described, which are commonly linked to the following observations:

- (i) Reduction of module efficiency due to a reduced fill factor, associated with local shunts.
- (ii) The formation of shunts is a very fast process, and hence, defects can form within one 10 ms single flash IV measurement [19] or after several 100 ms flashes [17].
- (iii) The occurrence of shunts does not stop with consecutive measurements, the damage adds up after each new stress exposure [18,25] The impact on module performance can, therefore, become severe, even though the individual effects of stress exposure are sometimes small.

- (iv) The defects causing the shunts are often referred to as wormlike defect, due to their distinct visual appearance. An example of the typical appearance of wormlike defects after a shading test can be found in Figure 3-7. More information on these defects is presented in Chapter 3.6.
- (v) The wormlike defects form in the region where a reverse bias voltage was present.

Another observation is that shading test lead to an initial change in performance, which is not stable over time. Some authors observed recovery after dark storage [26] or light soaking [27], but also mixed results were found with both improving and degrading modules after light stabilization treatment [18,28].

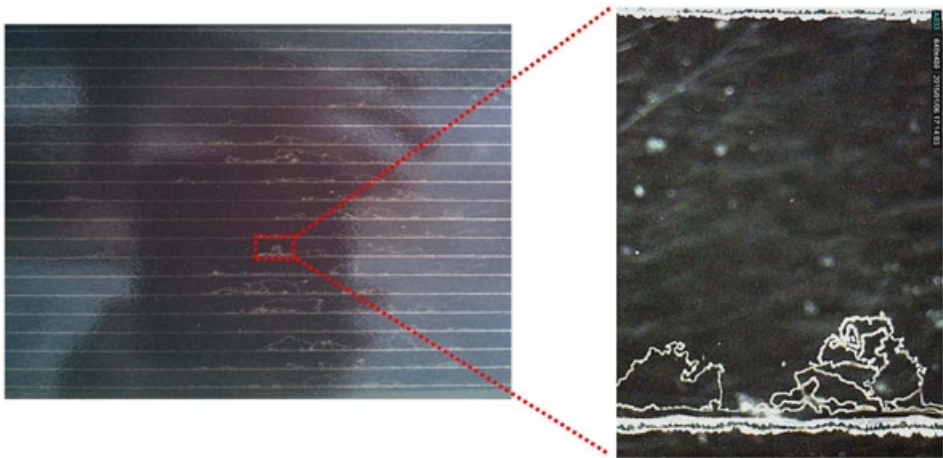


**Figure 3-7:** Pictures of wormlike defects in a CIGS module after shading stress test. (Reprinted with permission from Ref. [29].)



### 3.5 Thermoelectrical models on CIGS cells and modules

To estimate the stress loads during partial shading events, it is important to predict the internal voltage, current, and temperature profiles. Thermoelectrical modeling can, therefore, be used to explain the temperature differences during shading events, as would occur in the field (Figure 3-6). Specific models that are developed for CIGS devices have to take into account the nonlinear dependency of the reverse curve on illumination. This mechanism is responsible for the internal electrical current flow that is preferential in the illuminated area [22]. The following thermoelectrical models and how they included the light dependency for CIGS devices have been published:

- (i) Sun *et al.* [20] introduced the Poole–Frenkel mechanism to account for the light dependency of the reverse characteristic. The model uses a 2D SPICE simulation. The Poole–Frenkel principle was verified with the aid of cell measurements from another publication [30].
- (ii) Silverman *et al.* [22], used the Poole–Frenkel mechanism introduced by Sun *et al.* [20]. They validated the thermoelectrical model with temperature measurements on a commercial module. The model utilizes commercial Finite Element Analyses software.
- (iii) Carolus *et al.* [23], also used a thermoelectrical 2D SPICE model. The light dependency is accounted for by the use of measured *JV* curve both in the dark and under illumination. Verification of their model is a work in progress that has not yet been published.

Predictions do not always match reality as was shown by Silverman *et al.* [22] who compared the modeled and actual temperature data (Figure 3-8). The model correctly predicted an increase in temperature for the noncovered parts of the partly masked cells. However, their measurements showed small hotspots in both the covered and noncovered parts of the partially masked cells. These hotspots originate from already existing local shunts as well as the formation of new reverse bias induced defects. This type of defects has been successfully predicted by Nardone *et al.* [31], who included local weak spots in their model. These weak spots consumed all current in the shaded cells, causing local heating.

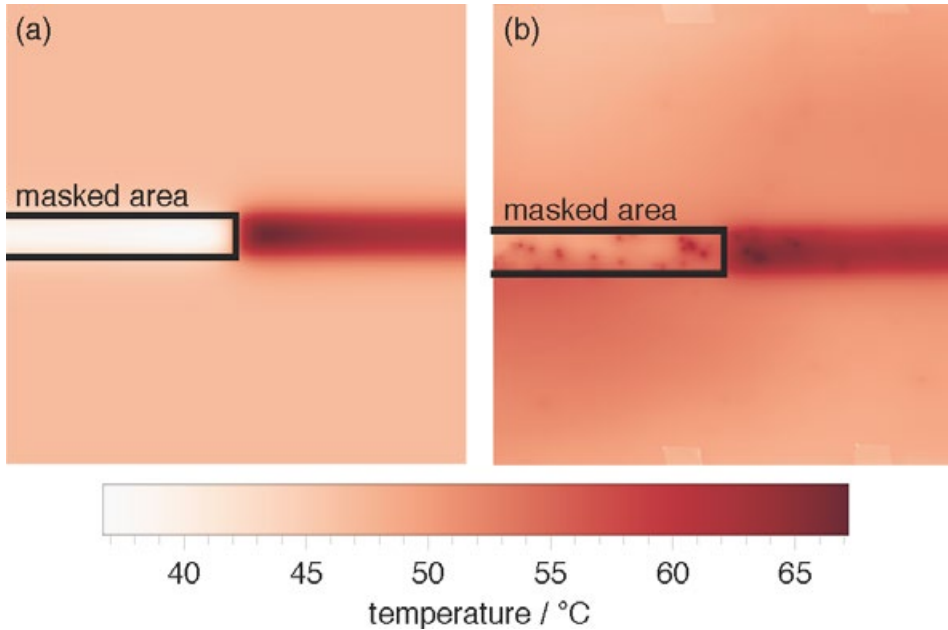


**Figure 3-8:** Simulated and measured maps of the back of the module temperature. The area inside the black line is the shaded area. **(a)** Simulation results of 100 cells in a  $0.5 \times 0.5 \text{ m}^2$  module. **(b)** Measurement of  $0.6 \times 0.6 \text{ m}^2$  portion of a larger commercial module. The large difference between simulated and measured data is caused by existing local shunts and the formation of reverse bias induced defects, not taken into account in the simulation. (Reprinted with permission from Ref. [22] , © 2015 IEEE.)

### 3.6 Reverse bias induced defects

In a module, the reverse bias induced defects act as local shunts and are often referred to as wormlike defects due to their distinct visual appearance. The first observation in 2007 was by van Dyk *et al.* [32]; however, they did not name them wormlike defects or linked them with the exposure to reverse bias. Introduction of the term wormlike defect came from Westin *et al.* [33] in 2009. Some descriptions that were given on the origin and nature of the wormlike defects are:

- (i) Formation has been observed as being a moving hotspot that moves toward the P1 scribe, while propagation along the P1 scribe is also observed [33–36].
- (ii) The origin is often an already existing weak spot like a small shunt [34–36].
- (iii) The absorber material has changed into a very porous structure [29,33,35] leading to changes in both composition and electronic properties. An example of the changed electronic properties is shown in the electron beam induced current (EBIC) image of Figure 3-9(a).
- (iv) Large voids were found at the interface of the transparent conductive oxide (TCO) and the CIGS material, as can be seen in Figure 3-9(b). Lifting the TCO layer gives the signature appearance [33,35].
- (v) The composition inside the defects has changed; zinc from the aluminum-doped zinc oxide TCO has been found to migrate into the CIGS absorber, while copper migrated toward the back contact. Brighter areas that were found in SEM cross-section are believed to be phase segregations [33].

Regardless of these studies, many questions about the origin and propagation mechanisms of these wormlike defects still exist. Explanations using thermoelectrical models are contradictory.

Richter *et al.* [37] concluded that neither diode-like defects nor ohmic shunts could generate sufficient heat to cause irreversible damage. Nardone *et al.* [31] on the other hand calculated that the current density in a local weak spot can reach approximately  $10^8$  A/m<sup>2</sup>, with accompanying peak temperatures above 900 K, enough to cause permanent material damage.

Experimental evidence exists that the wormlike defects originate in local weak spots like shunts [34–36]. However, Richter *et al.* [38] showed by using statistical analyses that the formation of wormlike defects is likely driven by an electric field rather than high local currents associated with local defects. The results from Richter *et al.* [38] are in line with the results from Puttnins *et al.* [39], who found a lower chance of forming wormlike defects when a thicker TCO was used.

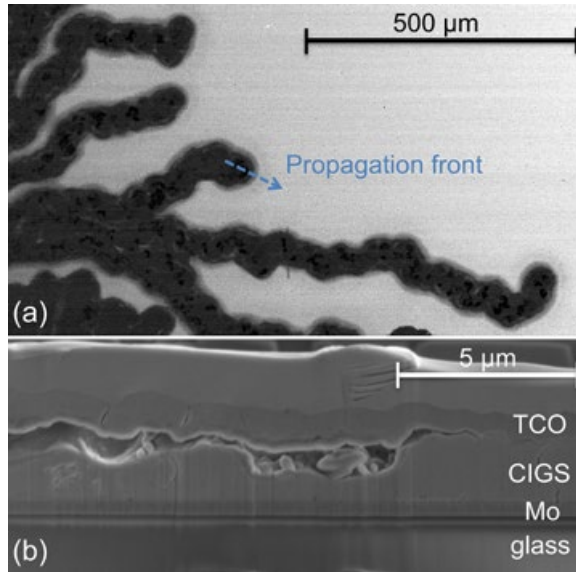


**Figure 3-9: (a)** EBIC picture of wormlike defect. Brighter colors represent more efficient current collection. The wormlike defect appears darker in this image, meaning that the defect has completely different electronic properties. **(b)** Cross-section of wormlike defect prepared with focused ion beam (FIB). Large voids were formed at the TCO–CIGS interface. (Reprinted with permission from Ref. [35].)

### 3.7 Reverse characteristic of single cells

One of the means to prevent reverse bias induced defects from forming is to limit the reverse bias voltage over a cell. This can be achieved by alternating the reverse characteristic in such a way that it acts as a built-in bypass diode. This requires a good understanding of the mechanisms behind the transition. Therefore, several studies have been published on the reverse characteristic [22,27,28,30,39–42].

A uniform description of the reverse characteristic is needed to be able to reliably compare studies from different sources. Unfortunately, the shape of the reverse characteristic has not been described thoroughly, which is in contrast with the forward region of the  $J/V$  curve. Here, the shape of the curve can be described by the combination of 5 parameters ( $V_{oc}$ ,  $J_{sc}$ ,

$FF$ ,  $R_{shunt}$ , and  $R_{series}$ ). The shape of the reverse characteristic seems more complex and is less studied. Often, one characteristic point on the reverse bias curve is used to compare samples within a study. The transition voltage is one of these points used to compare reverse characteristics. Two different approaches for the determination of the transition voltage have been published [40,41]. A more empiric method to compare the shapes of different reverse characteristics is to use the voltage needed to drive either a fixed current [12] (30 mA/cm<sup>2</sup> in the dark and 70 mA/cm<sup>2</sup> under illumination) or the photocurrent [27].

Several publications have reported on the influence of external conditions, like illumination intensity, spectrum of the light source, and temperature, on the reverse characteristic. The reported trends include the following:

- (i) A shift in transition voltages with illumination intensity [22,27,40]: a higher light intensity leads to a reduction in  $V_{tr}$ .
- (ii) Influence of the spectrum of the illumination source on the transition voltage. Several sources [27,30,40] reported that high energetic blue illumination reduces the transition voltage, while illumination with low energetic (red) light more resembled the behavior in the dark.
- (iii) The transition voltage increases when the temperature is reduced [30,40]. However, there seems to be a local maximum in the transition voltage around 200 K which depends on illumination wavelength [40]. Below this temperature, the transition voltage reduces again.

Besides external factors, the composition of the solar cell also influences the reverse characteristics; some reported compositional influences are as follows:

- (i) Effects of the buffer layer;
  - a. The buffer layer thickness influences the transition voltage, a thicker buffer layer leads to a higher transition voltage in the dark [30,39]. This is, however, not the case when illuminated with blue light [30], as is shown in Figure 3-10 for cells with a ZnSnO (ZTO) buffer layer with varying thickness.
  - b. No influence of the buffer layer material. Cells with CdS and

ZTO layers show the same behavior both in the dark [30,41] and with blue illumination [30].

- (ii) A higher sodium concentration in the CIGS layer reduces the transition voltage [40,42].
- (iii) The influence of the TCO layer thickness on the reverse characteristic is very small; however, a thicker TCO layer dramatically improved the survival rate of the cells from 25 to 75 % [39].
- (iv) The reverse characteristic reduces when the absorber layer thickness is reduced [28]. However a later study [43], that used more samples, showed that there is no influence of the absorber thickness on the reverse characteristic.

The observed trends are the basis of speculation on the mechanism behind the transition. Based on similarities with traditional semiconductor physics, the main mechanisms discussed are impact ionization (avalanche effect) or tunneling (Zener effect). Although also other mechanism (Poole-Frenkel and Fowler-Nordheim) were considered specifically for CIGS devices. The Poole-Frenkel mechanism in CIGS devices is well described in the paper of Sun *et al.* [20] and Fowler-Nordheim tunneling in CIGS devices is best described by Szaniawski *et al.* [41], the fundamental difference between the mechanisms is in the nature of the electron transport. For the Poole-Frenkel mechanism the electron transport occurs through defects while for the Fowler-Nordheim mechanism the electrons are transported by quantomechanical tunneling. The suggested mechanisms in chronological order of publication are as follows:

- (i) Mack *et al.* [27] concluded that the transition in the dark could be caused by either tunneling or avalanche currents, and the process is likely assisted by metastable interface charges.
- (ii) Szaniawski *et al.* [30] concluded that under illumination, tunneling is the exclusive mechanism behind the transition. However, in the dark, it could be either tunneling or a combination of tunneling and avalanching.
- (iii) Puttnins *et al.* [40] argued that in dark, it could be either tunneling or a combination of tunneling and avalanching.
- (iv) Silverman *et al.* [22] together with Sun *et al.* [20] introduced the Poole-Frenkel mechanism to account for the observed differences between dark and illumination behavior.

- (v) Nardone *et al.* [44] showed with semiconductor physic device simulations that the conventional mechanisms (including Poole-Frenkel) cannot adequately describe the reverse characteristic of CIGS cells.
- (vi) Szaniawski *et al.* [41] introduced the Fowler-Nordheim tunneling as the dominant mechanism in the dark.

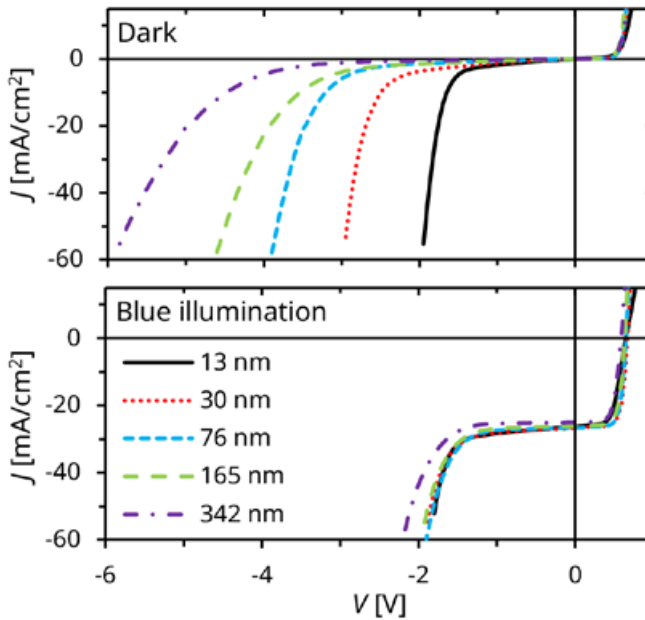


**Figure 3-10:** Influence of buffer layer thickness on both dark and (blue) illuminated  $JV$  curves. The top graph shows  $JV$  measurements in the dark with decreasing transition voltage with increasing buffer layer thickness (thickness increase from black solid to purple dashed dotted curve). Bottom graph shows  $JV$  measurements of the same cells with blue illumination. (Modified but based on Ref. [30].)

Over time, the more traditional Zener and avalanche mechanisms have been replaced by more complicated tunneling mechanisms. However, the mechanisms proposed do not fully explain the observed difference between the behavior under illumination and in the dark. The key in understanding the reverse characteristic of CIGS cells would be a mechanism that explains the discrepancy between light and dark. The Poole–Frenkel mechanism [20,22] could provide such an explanation. However, it was proven both experimentally [41] and theoretically [44] that the Poole–Frenkel mechanism is probably not responsible for the transition in the dark. So, despite all the efforts, there is still more research needed to fully understand the mechanism behind the reverse characteristic.

### 3.8 Non-permanent effects

While the formation of wormlike defects likely has the largest effect on device performance, various other effects have also been observed on single cells or small research modules:

- (i) Mack *et al.* (2008) [27], observed metastabilities caused by illumination and annealing at 160 °C in the dark. Light soaking and annealing reduces and increases the transition voltage, respectively.
- (ii) Westin *et al.* (2008) [33] observed degradation of  $V_{oc}$  and FF after combined exposure of cells to illumination and reverse bias. This was in contrast to cells that were only exposed to reverse bias in the dark, which only showed a reduction of the FF. They also reported that degradation of the  $V_{oc}$  could be recovered by light soaking.
- (iii) Szaniawski *et al.* (2013) [30] observed a very slow response of the current to changes in illumination for cells held at a constant negative voltage. In their study, it could take up to 5 min for the current to reach an equilibrium state after changes in illumination were applied.
- (iv) Theelen *et al.* (2016) [45] observed that during combined damp heat and illumination conditions, cells that were kept at a negative bias degraded more rapidly than the cells held at  $V_{oc}$ ,  $J_{sc}$ , or maximum power point over a period of 200 h.



- (v) Szaniawski *et al.* (2017) [41] observed that the reverse characteristic was shifting when repeating reverse  $JV$  measurements. They also described an increase in current over time when a cell is kept at a fixed negative voltage in the dark.
- (vi) Mortazavi *et al.* (2017) [46] observed a decrease in  $JV$  parameters for cells after a short (1 min) exposure to reverse bias voltages larger than 2 V. They also reported severe damage for cells after long (1 h) exposure to reverse voltages of 1.5 and 2 V, which could partly be recovered by light soaking.

### 3.9 Conclusions

The largest reliability impact of partial shading of CIGS modules is the formation of reverse bias induced wormlike defects. The appearance and morphology of these defects have been studied; nonetheless, the origin and exact mechanisms behind the formation and propagation remain unclear. Wormlike defects were found in most modules that were exposed to shading tests. It has to be mentioned that there was a change in the IEC norm, and it could be expected that newer products that enter the market will be much more shade-tolerant as it is required by this new IEC regulations. On top of that, both the published and ongoing research in this field will also contribute to the introduction of more shade-tolerant CIGS PV products.

### 3.10 Research topics for this dissertation

There are still some gaps in the existing state of the art research that were used to formulate these research questions and that will be discussed in more detail in the next chapters:

- (i) What is the mechanism behind the wormlike defects?
  - a. What is the mechanism behind the propagation of wormlike defects that give them this distinct patterns?
  - b. Can the propagation of wormlike defects be mitigated?
  - c. What are the conditions required to form wormlike defects?
- (ii) What is the mechanism behind the sharp increase in current in the reverse  $JV$  characteristic of CIGS solar cells?

### 3.11 Acknowledgments

I would like to thank Sourabh Dongaonkar, Timothy Silverman, Elizabeth Palmiotti, Steve Johnston, and Piotr Szaniawski for providing the original data files used to reproduce their figures.

CHAPTER 1
CHAPTER 2
CHAPTER 3
CHAPTER 4
CHAPTER 5
CHAPTER 6
CHAPTER 7
CHAPTER 8
CHAPTER 9



A large, stylized number '4' in a gradient of purple and blue, serving as a background for the chapter title.

**CHAPTER**

# Material property changes in defects caused by reverse bias exposure of CIGS solar cells

This chapter is based on the following publication:

K. Bakker, H. Nilsson Ahman, K. Aantjes, N. Barreau, A. Weeber, and M. Theelen, "Material Property Changes in Defects Caused by Reverse Bias Exposure of CIGS Solar Cells," *IEEE J. Photovoltaics*, vol. 9, no. 6, pp. 1868–1872, Nov. 2019, doi: 10.1109/JPHOTOV.2019.2940486.

## Chapter 4

# Material property changes in defects caused by reverse bias exposure of CIGS solar cells

**ABSTRACT:** Partial shading of  $\text{Cu(In,Ga)Se}_2$  modules can lead to the formation of reverse bias induced wormlike defects. These wormlike defects act as local shunts and permanently decrease module output. A good understanding of the formation and propagation mechanisms of these defects is needed in order to mitigate the negative effects, or to prevent these defects from forming. In this article, wormlike defects were formed on small non-encapsulated cells by exposing them to reverse bias conditions. Scanning electron microscopy-energy-dispersive X-ray spectroscopy measurements showed a rearrangement of elements: indium, gallium, and copper were replaced by cadmium, whereas selenium was replaced by sulfur in the area around the defect. Moreover, additional electronic-defect levels were found in that area with spectrally resolved photoluminescence spectroscopy. Based on the material changes in the area close to the wormlike defects, a propagation mechanism is proposed. The model assumes a chemical reaction as the driving force for propagation instead of melting as a result of ohmic heating.

## 4.1 Introduction

Partial shading of  $\text{Cu(In,Ga)Se}_2$  (CIGS) photovoltaic (PV) modules can result in potential harmful reverse bias conditions in the shaded region of the PV module. Reverse bias is the common term used for the negative (or reverse) operating voltage of the shaded cells in a partly shaded PV module. This operating condition is a consequence of the electrical series connection of all cells in a PV module. Because of the series connection, the photocurrent of the non-shaded cells is forced through the shaded cells.

This surplus of electric current results in the dissipation of energy within the shaded cell. This reverse flow of energy can result in the formation of reverse bias induced defects. These defects permanently decrease the output of the PV module. More defects can be created after consecutive shading events [18]. Shading, and the formation of reverse bias induced defects, can therefore have a negative effect on the long-term stability and operation in the field [19].

During shading events in both CIGS and CdTe local hotspots occur that can propagate within a cell [36]. The local hotspot leaves defects behind that act as local shunts. The difference between CdTe and CIGS is that in CIGS, the defects leaves trails that show a unique visual patterns [33] and are therefore often referred to as wormlike defects. Wormlike defects in CIGS have been observed in both packaged and unpackaged [35] CIGS devices. The composition of the absorber changes at the interface of the CIGS absorber with the transparent conductive oxide (TCO). The CIGS material expands and gets more porous [29]. This expanded porous material underneath the TCO film gives the wormlike defects its typical visual appearance. The structural appearance of wormlike defects was described in detail [29,33,35]. However, the propagation mechanism of these defects is still unclear. In order to answer the first sub-research question of Chapter 3 “What is the mechanism behind the propagation of wormlike defects that give them this distinct patterns?” a propagation mechanism for the wormlike defects is presented in this chapter based on compositional changes found at the edge of wormlike defects.

## 4.2 Materials and methods

Ten non-encapsulated small cells with an active area of approximately  $5 \times 7 \text{ mm}^2$  were used. The layout of these cells is specifically designed to mimic the geometry in a monolithically interconnected module, including analogues for the P1 and P3 interconnection scribes. A Schematic representation of the cell layout can be found in Chapter 5, Figure 5-3. The layer stack of the CIGS solar cells used is: 1 mm soda-lime glass, 500 nm DC-sputtered molybdenum,  $2 \text{ }\mu\text{m}$  co-evaporated CIGS, 50 nm chemical bath deposited cadmium sulfide, 65 nm DC-sputtered intrinsic zinc oxide, 1 or  $2 \text{ }\mu\text{m}$  DC-sputtered aluminum-doped zinc oxide, and 60 nm thermally evaporated gold contacts to the sides. A detailed description of the cell design and fabrication procedure can be found in [53].

In order to simulate partial shading in a module, which can result in the formation of wormlike defects, a reverse bias treatment was performed by sweeping a voltage in the dark from +0.7 till -10.0 V, using a Keithley 2400 source measure unit that was controlled by Tracer 3 software. Further analysis with scanning electron microscopy-energy-dispersive X-ray spectroscopy (SEM-EDX), spectrally resolved photoluminescence (sr-PL), and spatially resolved photoluminescence (PL) were performed with a JEOL JSM-6010LA IntouchScope, Horiba Labram Aramis Raman microscope equipped with a Symphony IR detector, and a 532-nm laser and a Greateyes LumiSolarCell LED-based EL/PL system, respectively. All instrument settings were kept constant throughout the experiment except for the integration time used during sr-PL measurement, this varied between 1 and 3 s dependent on signal strength. SEM-EDX measurements were performed at acceleration voltages of both 6 and 18 kV, the results of EDX point analyses are always the average of eight measurements.

In order to perform different analyses on the samples after formation of wormlike defect, an etching procedure was used. Figure 4-1 schematically shows the etching procedure, after the first step sr-PL measurements were performed, whereas SEM-EDX measurements were done after the second step. In order to allow for sr-PL, the conductivity of the Al:ZnO needs to be interrupted while leaving a thin layer of ZnO and CdS to protect the CIGS absorber material from photo-degradation during sr-PL measurements. This was accomplished by carefully removing the Al:ZnO with acetic acid. The sample was etched in several sessions of 30 s, checking the progress with PL after each session until the full non-degraded area exhibits a bright PL signal. In order to allow for EDX measurements on the bare absorber, a second etching step using 3 wt.% hydrochloric acid (HCl) was performed after the sr-PL measurements. The etch time for this final step was determined based on preliminary experiments. These experiments showed complete removal of CdS after 5 min in 3 wt.% HCl on the non-degraded parts. In this chapter, an etch time of 15 min was used in order to account for possible differences in etch rate in the degraded area.



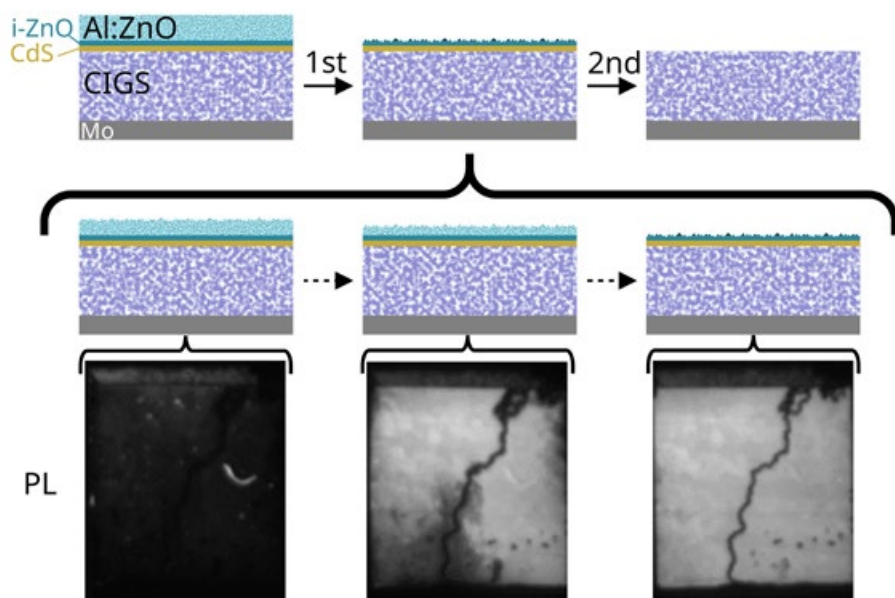


**Figure 4-1:** Schematic of etching procedure. First, etching step is to allow for sr-PL measurements. During the first step, the conductive Al:ZnO is removed with acetic acid, checking after every 30 s etch, with PL, until the full non-degraded area exhibits a bright PL signal. Second step is removal of the residual ZnO and CdS with HCl to obtain a clean surface for SEM-EDX.

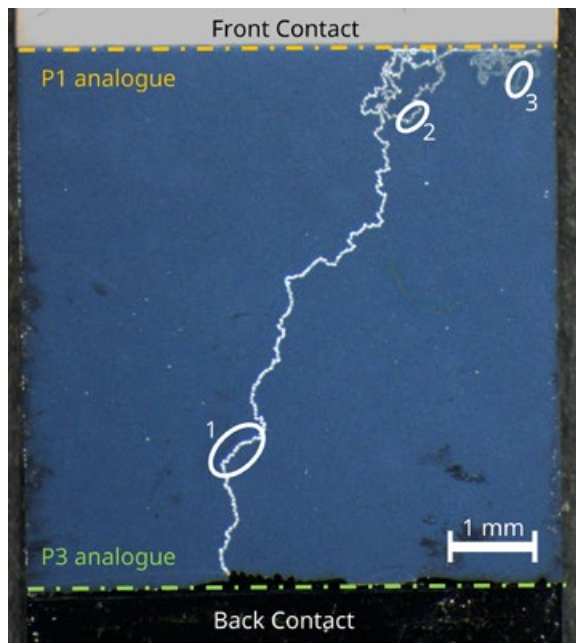
## 4.3 Results and discussion

### 4.3.1 Defect creation and appearance

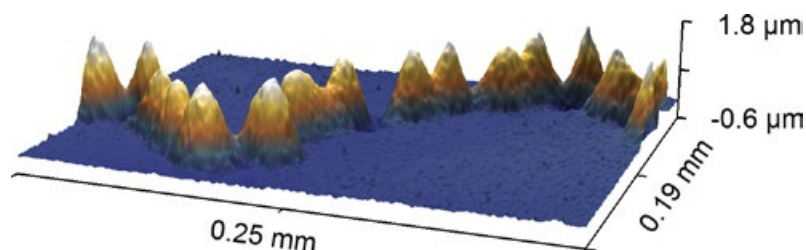
The reverse bias treatments resulted in the formation of wormlike defects in eight out of the ten samples. For the eight defected samples, the average efficiency was reduced from  $12.4 \pm 0.8$  % to  $0.4 \pm 0.6$  %. Moreover, for six out of these eight cells, the shunting was so severe that the electrical output was reduced to 0 %. More information on the *JV* results of these samples can be found in Chapter 5.3.

Figure 4-2 shows a microscope image of the surface of a severely shunted

cell after reverse bias treatment. In this figure, wormlike defects can be observed in the form of white meandering lines. Confocal microscopy shows that wormlike defects consist of small individual protruding mountains that are linked together (see Figure 4-3). No major differences were observed in confocal microscopy before and after etching. Furthermore, Figure 4-2 displays apparent differences in the brightness of the trails, indicated by the numbered white circles. Brighter trails (number 1) are wider and are made up of bigger individual islands than the darker trails (numbers 2 and 3). The results of the confocal microscopy will be discussed in more detail in Chapter 5.3. In addition, the trails seem to propagate along a line at the top of the picture. This line is indicated with a dashed orange line in Figure 4-2 and coincides with the P1 analogue, which is the border of the molybdenum layer underneath the solar cell. For all cells where the wormlike defects reached the P1 analogue, the efficiency was reduced to 0 %.



**Figure 4-2:** Microscope image of a cell with wormlike defects. Dashed lines indicate the positions of the P1 and P3 scribe analogues. Numbered white circles indicate different sizes of wormlike defects.



**Figure 4-3:** Confocal microscopy image of a wormlike defect (before etching).

### 4.3.2 Scanning electron microscopy-energy-dispersive x-ray spectroscopy

The SEM image of Figure 4-4 shows the bare CIGS material and the wormlike defect after the HCl etch. Inside the wormlike defect, the material is changed into a porous material. The border region of the wormlike defect appears darker compared with the surrounding CIGS material, indicating that the material close to the defect differs from the bulk material further from the wormlike defect.

EDX mapping showed changes in elements in this darker border region. To obtain more quantitative information on the changes in this border region, a number of EDX point analysis were performed. Even though the EDX is not calibrated, it is able to visualize trends compared with measurements performed on the bulk material taken millimeters away from the affected area. The results of the EDX measurements are shown in Figure 4-5. The values on the y-axis are in atom percent and are deviations from the bulk measurements. Furthermore, all datapoints are an average of eight measurements. Repeating the measurement process on different locations on the same sample yielded comparable results. Furthermore, the data shown were obtained with an acceleration voltage of 6 kV to probe close to the surface of the material. Table 4-1 lists the EDX deviations from the bulk for Cd and S for two different acceleration voltages. From the table it can be observed that measurements with a higher penetration depth, performed at 18 kV, showed the same trend; however, the deviations from bulk measurements were much smaller. This indicates that the observed changes mostly take place at the surface of the material.

From Figure 4-5, it can be observed that the composition started to change around 25  $\mu\text{m}$  from the edge of the defect, this coincides with the darker border region of the defect in Figure 4-4. This change seems to occur in two separate processes.

- (i) The exchange of selenium for sulfur: moving toward the defect, there is a simultaneous rise in sulfur content and a decline in selenium content that starts around 25  $\mu\text{m}$  from the edge of the defect.
- (ii) Indium, gallium, and copper are likely replaced by cadmium. The presence of cadmium is surprising, since etching with HCl is expected to result in complete removal of the cadmium sulfide layer. Therefore, it is likely that the cadmium is incorporated in the modified absorber material.

The onset of the second process occurs closer to the edge of the defect; therefore, it is likely that two separate processes are taking place.

In Table 4-2, the signals of Cu, In, and Ga from Figure 4-5 are listed and compared with the Cd signal. The decrease in the total (In + Ga + Cu) content appears similar to the increase in Cd content. It should be noted that the decrease in the copper signal only appears in close vicinity of the defect, further away there is even a slight surplus of copper. In contrast with the indium and gallium content that is reduced in a large area around the defect.

Cd is known to diffuse into CIGS under the influence of temperature [47]. A recent study by Biderman *et al.* [48] ruled out the diffusion by grain boundaries. They suggested that the Cd diffusion process is a combination of both substitutional-vacancy-based diffusion and interstitial-based diffusion. For both mechanisms, a Cd ion reacts with a vacancy to form substitutional cadmium ( $\text{Cd}_{\text{Cu}}$ ,  $\text{Cd}_{\text{In}}$ , or  $\text{Cd}_{\text{Ga}}$ ). In the case of the substitutional-vacancy-based diffusion process, the substitutional Cd jumps to a neighboring vacancy. In an interstitial-based diffusion process, the Cd ion diffuses through the lattice as an interstitial and reacts with a vacancy. Furthermore, Biderman *et al.* [48] stated that the Cd ions preferred to occupy copper vacancies. The results from this experiment however suggest that during reverse bias induced defect formation, the Cd is mostly replacing In and Ga. Possibly In and Ga and to a lesser extent Cu, during defect formation, migrate from the border region leaving vacancies

that are occupied by Cd ions, supplied from the CdS buffer layer. It is likely that the missing elements have migrated from the border region to the wormlike defect.

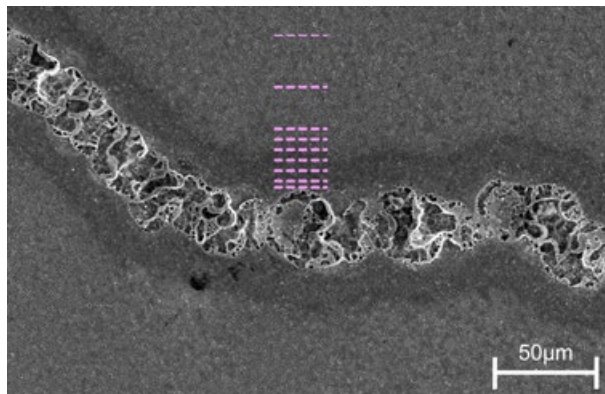


**Figure 4-4:** Top view SEM image of wormlike defect after HCl etch. The pink dashed lines indicate the approximate position of the EDX point measurements.

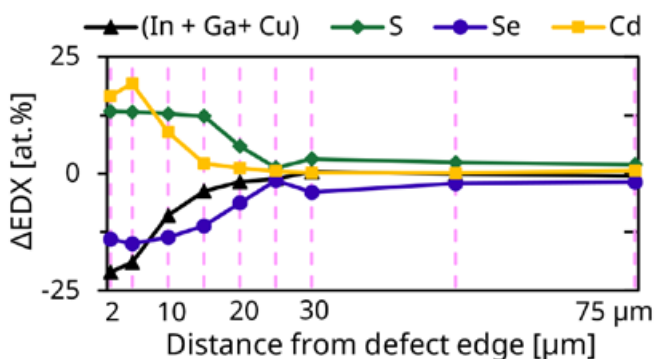


**Figure 4-5:** EDX deviation from bulk measurements with respect to distance from the edge of the wormlike defect. EDX measurements were performed with an acceleration voltage of 6 kV. The EDX results on the y-axis are in atom percent and are subtracted from the bulk measurements far away from the degraded area. The vertical pink dashed lines correspond with positions along the pink dashed lines of Figure 4-4 where the measurements were performed.

**Table 4-1:** Average  $\Delta$ EDX values for cadmium and sulfur on the measurement positions indicated with pink lines in Figure 4-4.

Position [μm]	$\Delta$ EDX [at%] Cd 6kV	$\Delta$ EDX [at%] Cd 18kV	$\Delta$ EDX [at%] S 6kV	$\Delta$ EDX [at%] S 18kV
Bulk	0	0	0	0
75	0.6	0.1	2.0	0.3
50	0.2	0.4	2.4	0.7
30	0.2	0.2	3.2	0.3
25	0.5	0.0	1.3	0.6
20	1.2	0.2	5.9	0.8
15	2.2	0.8	12.3	2.3
10	8.9	3.5	12.8	3.3
5	19.3	4.4	13.2	3.2
2	16.6	5.8	13.4	3.5

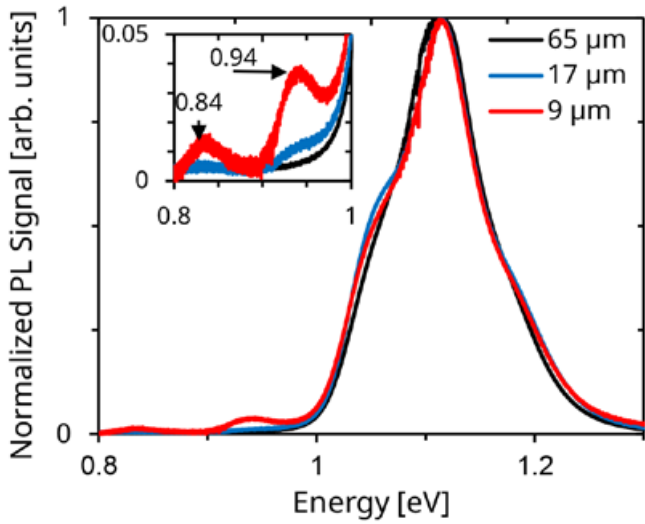
**Table 4-2:** Average  $\Delta$ EDX in atom percent for Cd, (In + Ga + Cu), In, Ga, and Cu on the measurement positions indicated with pink lines in Figure 4-4.

Position [μm]	$\Delta$ EDX [at%] Cd	$\Delta$ EDX [at%] (In+Ga+Cu)	$\Delta$ EDX [at%] In	$\Delta$ EDX [at%] Ga	$\Delta$ EDX [at%] Cu
Bulk	0.0	0.0	0.0	0.0	0.0
75	0.6	-0.5	0.6	-1.1	0.0
50	0.2	0.0	1.0	-1.0	0.0
30	0.2	0.4	1.8	-0.7	-0.7
25	0.5	-1.1	1.0	-0.9	-1.2
20	1.2	-1.8	1.7	-2.2	-1.3
15	2.2	-3.7	4.0	-5.7	-2.1
10	8.9	-8.9	1.2	-8.2	-1.9
5	19.3	-19.0	-4.3	-12.2	-2.6
2	16.6	-21.1	-7.7	-8.5	-4.9

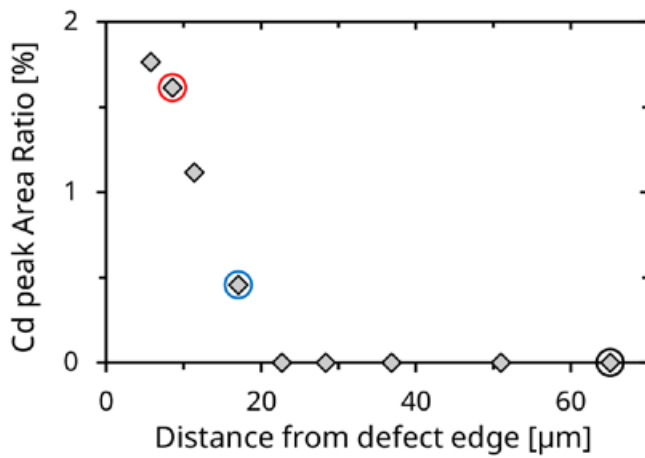
### 4.3.3 Spectrally resolved photoluminescence spectroscopy

Figure 4-6 shows normalized PL spectra obtained at several positions in the border region of the defect. Compared with the measurement in the bulk (65  $\mu\text{m}$  distance), two additional features were found in PL spectra measured closer to the defect (9 and 17  $\mu\text{m}$ ). The peak position of these additional features are not constant between samples and on different positions within one same sample, and are within the range of 0.84–0.87 eV and 0.94–0.97 eV. Peaks at lower energies are usually assigned to energy transitions between donor–acceptor pairs between different point defects, vacancies, interstitials, and substitutional vacancies. A peak around 0.94 eV has been described and some of the literatures have assigned the peak around 0.94 eV to  $\text{Cd}_{\text{Cu}}$  [8,49]. Although the exact nature of the peaks is unknown, substitutional cadmium could be a possibility because of the large amount of Cd found in the EDX measurements. Therefore, these peaks are assigned to the presence of cadmium. In Figure 4-7, the contribution of cadmium is expressed as the ratio between the areas of the 0.84 and 0.94 eV peaks and the area of the total spectrum. As can be observed from Figure 4-7, the onset of the Cd PL contribution takes place on the same distance scale as the compositional changes observed in the EDX measurement.

Inside the wormlike defect, no PL signal could be measured. Close to the edge of the defect, PL spectra could be obtained; however, with a much lower intensity compared with the unaffected bulk material. In general, a decrease in PL intensity is associated with a reduction of the local voltage and associated solar cell performance. Since there is a PL signal generated in the border region, the semiconductor material properties in that area are not completely lost. However, it is not yet possible to estimate the contribution of the deteriorated border region on the total shunt resistance of the defect.



**Figure 4-6:** Normalized PL spectra obtained at different distances from the edge of the defect. The inset shows a magnification of the region between 0.8 and 1.0 eV.



**Figure 4-7:** Contribution of the Cd peak area ratio from sr-PL as function of distance from the edge of the defect. The cadmium ratio is the area of the peaks at 0.84 and 0.94 eV divided by the area of the whole spectrum. The circled datapoints are the measurements displayed in Figure 4-6.



## 4.4 Discussion on propagation mechanism

Based on the compositional changes in the edge observed by both EDX and sr-PL measurements, a mechanism for worm formation and propagation is proposed. The proposed mechanism is based on the hypothesis that a (chemical) reaction is responsible for the observed compositional changes inside the wormlike defect. This reaction is fueled by the heat caused by the high current density in the defect. Reactants supplied from the surrounding region are required to sustain the growth of the defect. In order to get the reaction started, heat, electricity, and defected absorber material are probably needed simultaneously. Figure 4-8 displays a schematic of the propagation mechanism. In this proposed propagation model, the formation and propagation goes through the following steps.

- 0) Start at a small weak spot (e.g., a shunt).
- 1) The small weak spot becomes a local hotspot during reverse bias operation as it conducts more current than the surrounding area.
- 2) A reaction starts that changes the material inside the defect to the more porous composition. Reactants for the reaction are obtained from the surrounding area.
- 3) The defect expands and forms an “island”. The reactants that have left the border region leave vacancies that are filled up with elements from the buffer layer, creating a “Cd” rich region.
- 4) Multiple new weak spots are created in the Cd rich area, because of the reduced (electronic) material properties. One or a cluster of several of these newly formed weak spots form a new local hotspot where the conditions are favorable in order to start a new reaction site.
- 5) The process starts again at step 1 creating a new island and the old islands cools down as the reaction stops.

Since the wormlike defect appears to propagate in the direction of the P1 scribe, the origin of supplied electrical current implicates that electricity plays an important role in the process. Since the reaction mostly takes place at the surface [29] and the fact that the Al:ZnO layer stays intact supports the idea that electricity supplied by the TCO is needed for the reaction. The influence of the electric field will be discussed in Chapter 5.

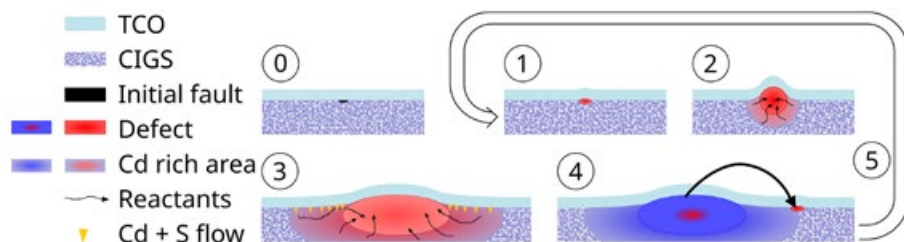


**Figure 4-8:** Schematic of the proposed propagation mechanism. Step 0 represents the initial starting point in the form of a local weak spot. In step 1, a reverse bias is applied and the weak spot becomes a hotspot. This hotspot expands in step 2 and start to attract reactants from the surrounding. In step 3, the defect has expanded and Cd and S from the buffer layer occupy the space left by the migrated reactants. In step 4, the hotspot shifts to a new location and the reaction starts again from the start in step 5.

## 4.5 Conclusions

A propagation method is proposed based on the discrete islands that make up the wormlike defects and compositional changes found in the region next to the defects. The compositional changes in the region close to the defects originate at the surface and include the exchange of metals (Cu + In + Ga) for Cd from the buffer. Additional sr-PL measurements suggested that cadmium from the buffer layer is occupying vacancies left by the metals. For the proposed propagation method, the wormlike defects start at an initial weak spot. During reverse bias, this weak spot becomes a local hotspot. Because of heat and an electric field, a chemical reaction is started in this hotspot. The hotspot expands and the reaction is partly fueled from material outside the wormlike defect. The hotspot moves to a next location because the original hotspot runs out of fuel and favorable conditions are created in the area of the new hotspot. This chapter revealed that there are still some open questions. The two most prominent examples are: first, the exact mechanism of the reaction inside the hotspot and second, the role of the electric field in the propagation of the wormlike defects. This is the first step in answering one of the main research questions “What is the mechanism behind the wormlike defects?”. More details on the mechanism behind the reaction that forms the wormlike defects can be found in Chapter 7. The influence of the electric field will be described in more detail in Chapter 5.



## CHAPTER

# Propagation mechanism of reverse bias induced defects in $\text{Cu(In,Ga)Se}_2$ solar cells

This chapter is based on the following publication:

K. Bakker, H. N. Ahman, T. Burgers, N. Barreau, A. Weeber, and M. Theelen, "Propagation mechanism of reverse bias induced defects in Cu(In,Ga)Se<sub>2</sub> solar cells," *Sol. Energy Mater. Sol. Cells*, vol. 205, p. 110249, Feb. 2020, doi: 10.1016/j.solmat.2019.110249.

## Chapter 5

# Propagation mechanism of reverse bias induced defects in Cu(In,Ga)Se<sub>2</sub> solar cells

## GRAPHICAL ABSTRACT:

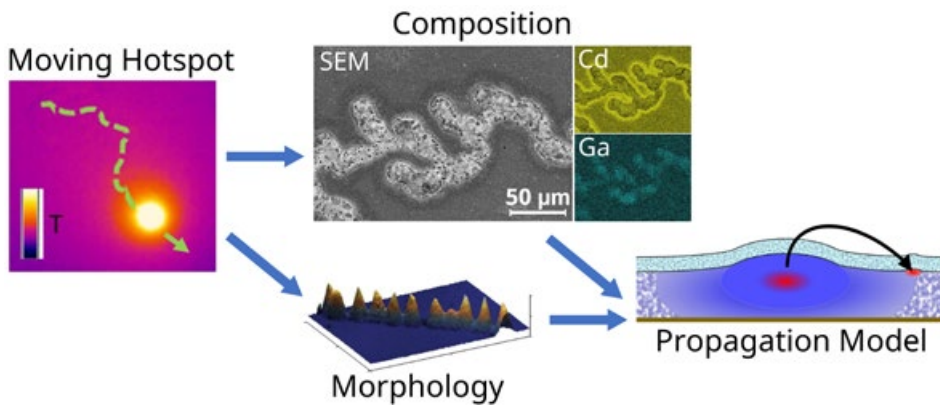


**Figure 5-1:** Graphical abstract as published with the online version of ref. [50].

**ABSTRACT:** In Chapter 4 a propagation method was introduced to explain the propagation of wormlike defects. In this Chapter the influence of the electric field on the propagation of wormlike defect is studied. Differences in observed propagation patterns caused by the lateral voltage drop over the TCO layer were observed. Furthermore, additional compositional measurements were performed at the edge of the defects. The influence of the electric field over the absorber layer is added to the propagation mechanism of Chapter 4.

## 5.1 Introduction

Worldwide installed photovoltaic (PV) capacity is growing and with this growth more PV is being installed in urban environments. Application of PV in urban environments has different requirements compared to land based PV farms. Properties like aesthetics for public acceptance and shade tolerance to increase annual output, are more important. Thin-film PV technologies including  $\text{Cu(In,Ga)Se}_2$  (CIGS) have potential advantages to these requirements compared to the mainstream wafer-based crystalline silicon (c-Si) PV modules that are currently dominating the market.

The typical CIGS PV module is of the monolithically interconnected type. These modules have a unique layout of strings of series connected, long and narrow cells. Major advantage of this design is that CIGS PV modules are, in general, much more shade tolerant with respect to power loss than c-Si modules [15]. However, the disadvantage of a monolithically interconnected PV module is that it is nearly impossible to integrate bypass diodes to protect the individual cells from reverse bias exposure [29].

Reverse bias occurs when one or multiple cells in a module are shaded. The shaded cell is, due to the electrical series connection, forced to conduct more current than it is generating. Due to this imbalance in currents the shaded cell will dissipate power and the operating point will shift toward a negative voltage. This operating condition is often called reverse bias.

Reverse bias in CIGS modules can lead to local defects, sometimes referred to as “wormlike” defects [33], because of their very distinct visual appearance. Reverse bias induced defects act as local shunts, permanently reducing the module output. These defects originate in local weak spots [34–36,51] and can be formed relatively easily when no mitigation measures are in place, for example by shades cast from humans or tools [18,28]. Propagation of defects as observed with thermal imaging [33,36] occurs in the form of a moving hotspot. This hotspot leaves a trail that consists of individual islands [33] of a porous material that are argued to start at the interface with the buffer layer [29]. However, up to now there is no real understanding of the mechanism behind the formation and propagation of these defects.

In this chapter the proposed propagation mechanism introduced in Chapter 4 is expanded with the influence of the electric field over the absorber. This expanded mechanism is based on extensive studies of propagation patterns and the composition of wormlike defects.

## 5.2 Materials and methods

### 5.2.1 Samples used

The layer stack of the CIGS solar cells used in this study consists of: 1 mm soda-lime glass (SLG), 500 nm DC-sputtered molybdenum (Mo), 2  $\mu\text{m}$  co-evaporated CIGS, 50 nm chemical bath deposited cadmium sulfide (CdS), 65 nm DC sputtered intrinsic zinc oxide (*i*-ZnO), 1 or 2  $\mu\text{m}$  DC sputtered aluminum doped zinc oxide (Al:ZnO) as transparent conductive oxide (TCO) and 60 nm thermally evaporated gold (Au) contacts. The cell layout used closely resembles a cell in a monolithically interconnected commercial module, including analogues for P1 and P3 scribes. The P1 equivalent was created by electrochemically etching part of the molybdenum back contact prior to CIGS deposition. Before gold deposition the P3 equivalent was made by scratching away the full layer stack from the molybdenum with a blade. The cell area is approximately 5×7 mm<sup>2</sup> and the cells are without grid, therefore the efficiency is lower compared to cells with metal contacts and very thin TCO. A schematic of the cell design is given in Figure 5-2. More information on the cell design and manufacturing process can be found in previous work [52,53] and a description of the 3-stage CIGS co-evaporation process is given by Couzinie-Devy *et al.* [54].

For this study ten samples from three different CIGS deposition runs were used. The variations between runs were:

- (i) Run I: 6 samples, standard processing and used as reference.
- (ii) Run II: 2 samples, slightly higher Cu flux during 2<sup>nd</sup> stage of the 3-stage CIGS co-evaporation deposition resulting in a different Ga profile.
- (iii) Run III: 2 samples, substrates with Na barrier and the same CIGS deposition conditions as run II. Additionally a Na post- deposition treatment (PDT) [13] was carried out.

To study the influence of the TCO on reverse bias behavior of the cells both the TCO layer thickness and deposition tools were varied. The sputter tools used for deposition are located at the Institut des Matériaux Jean Rouxel of the Université de Nantes in Nantes, France and at the TNO – partner in Solliance facilities in Eindhoven, the Netherlands. These sputter tools will be referred to as “Nantes” and “Solliance”, respectively. On half of the samples from run I a 1  $\mu\text{m}$  thick TCO layer was deposited with the tool



named “Solliance”, while on the other half a 2  $\mu\text{m}$  thick layer was deposited using the tool named “Nantes”. On all samples from CIGS runs II and III the standard 1  $\mu\text{m}$  thick TCO was deposited using the Nantes tool. An overview of the manufacturing parameters for all samples is presented in Table 5-1. The sample name starts either with the run number or with a T for samples with a 2  $\mu\text{m}$  thick TCO.

After reverse bias exposure the layers on top of the CIGS absorber of samples I-3 and T-2 were removed in two stages to allow further analyses. In the first stage a 1 wt% acetic acid (HAc) solution was used to remove the TCO by dipping for 3 and 6 min for the sample with 1 and 2  $\mu\text{m}$  thick TCO, respectively. The samples were subsequently etched using a 3 wt% hydrochloric acid (HCl) solution for 15 min to completely remove the remaining ZnO and CdS. This procedure was described in detail in Chapter 4.2.

### 5.2.2 Reverse bias exposure

Wormlike defects as observed in commercial CIGS solar modules were replicated on small solar cells by exposing them to a controlled voltage sweep in the reverse direction. The voltage sweep was executed by a Keithley 2400 source measure unit (SMU), controlled by a computer using the RERA Tracer 3 software. The sweep settings used are: start voltage +0.7 V; end voltage -10 V; step voltage 50 mV; scan speed 100 mV/s; current limit 100 mA. The reverse bias (RB) sweeps were carried out in the dark. The current limit of 100 mA was selected because it is the current generated in approximately 3  $\text{cm}^2$  of a neighboring cell that is fully illuminated. Furthermore, this value is in the range of currents (30–100 mA) observed during the formation of wormlike by Guthrey *et al.* [51].

### 5.2.3 Characterization

Solar cell parameters were recorded with current density – voltage ( $J/V$ ) measurements both under AM 1.5 illumination and in the dark using a Neonsee class AAA solar simulator. This system was calibrated with a Konica Minolta AK200 reference cell. Scanning electron microscopy (SEM) including elemental analyses with energy-dispersive X-ray spectroscopy

(EDX) were performed using a JEOL JSM-6010LA IntouchScope. Raman spectroscopy was executed using a Renishaw inVia Raman microscope with a 632 nm HeNe (Red) and a 514 nm Ar ion (green) laser. For optical and confocal microscopy a Leica MZ12.5 and a Leica DCM 3D were used, respectively. To generate the SEM-EDX image of Figure 5-7 an acceleration voltage of 10 keV was used. For the elemental maps the L, L, K, and K lines were used for Cd, In, Ga and Cu, respectively. The cross section of Figure 5-11(a) was made by Eurofins material science using a focused ion beam (FIB) and a FEI Nova 200 NanoLab system. Lock-in thermography was done on a system from Infratec that uses IR LEDs as excitation source.

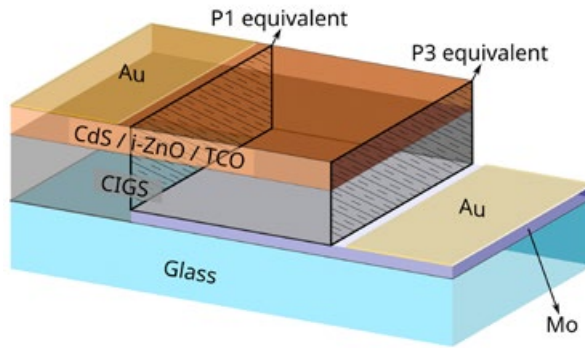


**Figure 5-2:** Schematic representation of the cell layout (not to scale). Active cell area is approximately  $5 \times 7 \text{ mm}^2$ , current collection from the Mo and TCO is done at the gold contacts. Hatched cross sections represent the P1 and P3 analogues as found in commercial monolithically interconnected modules.

**Table 5-1:** The most important process and sample parameters, the efficiency before and after reverse bias (RB), and information on defect formation. The values for current density ( $J_{t1}$ ) and voltage ( $V_{t1}$ ) just before electrical breakdown are presented as well.

Sample Name	CIGS run	CIGS variation	TCO sputter tool	TCO thickness [μm]	Initial η [%]	After RB η [%]	$J_{t1}$ [mA/cm <sup>2</sup> ]	$V_{t1}$ [V]	Defects
I-1	Run I	Standard	Solliance	1	11.9	0.0	7.5	6.5	Mobile
I-2	Run I	Standard	Solliance	1	12.4	12.6	...	...	None
I-3	Run I	Standard	Solliance	1	12.4	0.0	6.2	8.2	Mobile
T-1	Run I	Standard	Nantes	2	11.6	1.5	7.8	7.8	Stationary
T-2	Run I	Standard	Nantes	2	12.5	1.4	27.7	8.8	Stationary
T-3	Run I	Standard	Nantes	2	12.1	0.0	211.2	9.4	Stationary
II-1	Run II	Cu flux	Nantes	1	11.4	0.0	12.1	7.1	Mobile
II-2	Run II	Cu flux	Nantes	1	12.9	0.0	1.0	9.1	Mobile
III-1	Run III	Na PDT <sup>a</sup>	Nantes	1	15.0	13.5	6.9	7.0	None visible
III-2	Run III	Na PDT <sup>a</sup>	Nantes	1	14.3	0.0	1.2	7.0	Mobile

<sup>a</sup>PDT: Post-deposition treatment.

## 5.3 Experimental results

### 5.3.1 Reverse bias results

Figure 5-3 shows the  $J/V$  results of a reverse bias sweep for cells with (red) and without defect formation. The formation of a defect (between  $t_1$  and  $t_2$  in Figure 5-3) is a very fast process. It occurs during the acquisition of 1 datapoint (500 ms) and is characterized by a sharp increase in current. It is likely for the defects to be formed even faster, as Wendlandt *et al.* [19] reported the formation of wormlike defects in modules within one 10 ms  $J/V$  measurement. During the propagation phase (between  $t_2$  and  $t_3$ ), the measurement system is operating at a fixed current limit and the voltage is fluctuating. The propagation voltage is the average voltage during the propagation phase, and is an indication of the voltage needed for propagation. This voltage provides information on the electric field inside the defect during propagation.

The propagation voltage of all cells with visible wormlike defects is plotted in Figure 5-4. Samples with a thick TCO have a smaller propagation voltage compared to samples with a thin TCO. This implies that the propagation voltage is influenced by the TCO thickness and the associated change in lateral conduction of the TCO with layer thickness. Next to the TCO thickness, the CIGS absorber material properties also has an effect.

The solar cell efficiencies before and after reverse bias exposure are listed in Table 5-1. Two samples still have efficiencies above 10 % after the RB exposure and do not show visible wormlike defects, which is in contrast to the eight severely degraded cells that all showed visible defects. The current density ( $J_{t1}$ ) and voltage ( $V_{t1}$ ) just before the defect formation ( $t_1$  in Figure 5-3) are also listed in Table 5-1. The voltages at which the defects start to form are in the range of 6. To 9.4 V. The upper limit of this range is close to the limit of the  $J/V$  sweep (10 V). Therefore, the voltage needed to get a defect started for the surviving cell (I-2) is more than 10 V. The other cell (III-1) that did not exhibit a wormlike defect did lose some efficiency because a small shunt was formed at the edge of the cell after the reverse bias sweep. The current densities at which defects start to form are in general much lower than  $J_{sc}$ . This is in agreement with the results of Westin *et al.* [33] who created wormlike defects by injecting a current equivalent to the short circuit current.

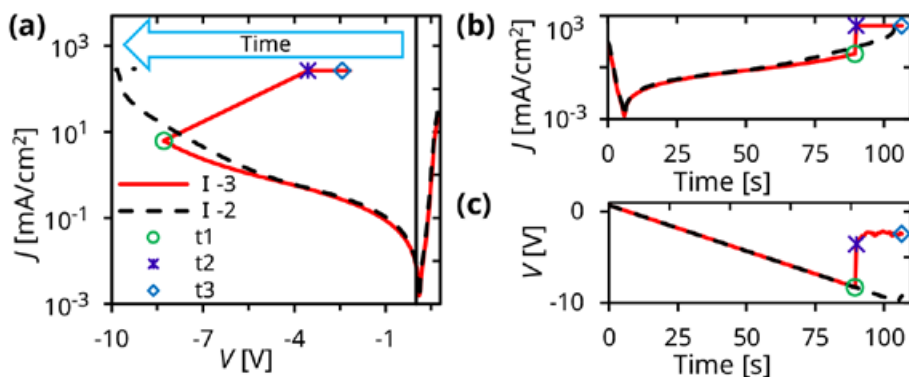


**Figure 5-3:** Results of the reverse bias treatment for samples I-3 (red line) and I-2 (black dashed line) with and without visible wormlike defect formation, respectively. The individual graphs display **(a)** the current density ( $J$ ) as function of voltage ( $V$ ), **(b)**  $J$  versus time and **(c)**  $V$  as function of time. Points of interest are marked. The starting point of the formation of the defect is point t1 (green circle), the first point after defect formation at current limit is point t2 (purple asterisk) and point t3 is the end of the sweep (blue diamond).

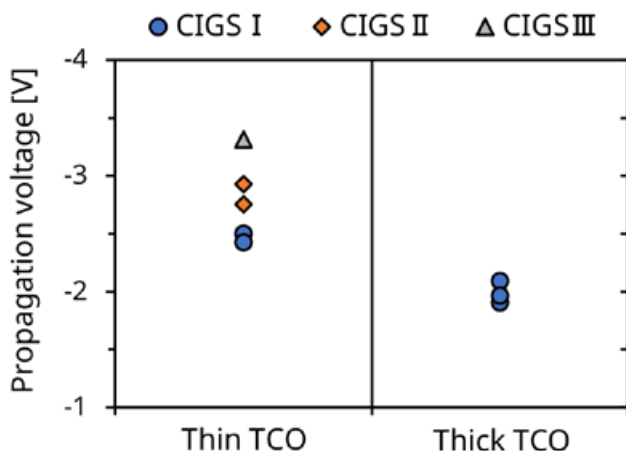


**Figure 5-4:** Voltage during propagation phase (average voltage between t2 and t3 in Figure 5-3) of all samples that showed visible wormlike defects. On the left samples with 1  $\mu$ m TCO thickness and on the right samples with 2  $\mu$ m thick TCO are shown. The blue circles, red diamonds and green triangles represent run I, run II and run III, respectively.

### 5.3.2 Optical microscopy

The visible defects show two distinctly different propagation patterns, which are classified as “mobile” and “stationary” wormlike defects. The visual observations after classification, for all cells, are included in Table 3-1 and pictures of representative examples of the two classes can be found in the cropped microscope images in Figure 5-5.

The stationary wormlike defects were found exclusively on the cells with thick TCO, and are not completely detrimental to the cell as long as they did not extend to the P1 analogue. Mobile defects were found on samples with thin TCO. All mobile defects extended to the P1 analogue, resulting in completely shunted cells. Furthermore, the mobile defects propagated along the P1 analogue as was also observed by Lee *et al.* [29] and Westin *et al.* [33]. The defects did not cross the P1 analogue into the region without molybdenum underneath the absorber, which means that the defects are only created in areas where an electric field is present between the molybdenum back and the TCO front contact.

The defect in Figure 5-5(a) seems to have originated at the border where the CIGS was mechanically removed (P3 analogue) at the right side of the picture. Several studies [34–36,51] showed that wormlike defects originate at local weak spots. A mechanically defined edge could be a local weak spot; though, only 3 out of 8 wormlike defects started at a mechanically defined edge.

Lock-in thermography was performed on the samples before and after reverse bias exposure. The thermal pattern shows that the traces of the wormlike defects are locally heated and thus locally shunted. However, no quantitative information can be obtained from these measurements.

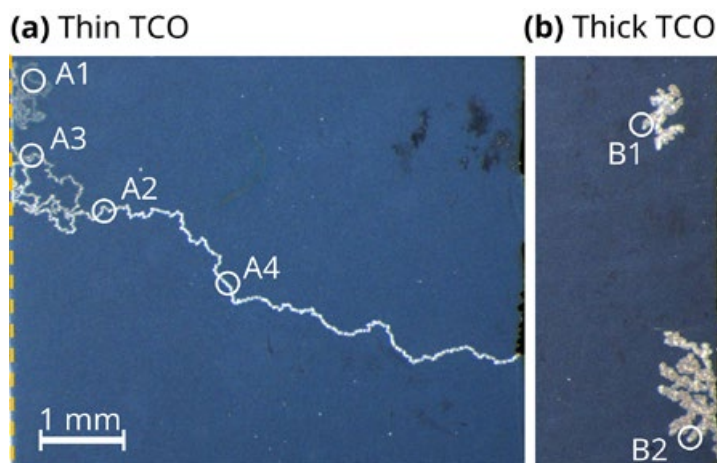


**Figure 5-5:** Cropped microscope pictures of two cells with wormlike defects that show different propagation patterns. **(a)** Sample I-3 with “mobile” wormlike defects and a thin TCO. **(b)** Sample T-2 with “stationary” wormlike defects and a thick TCO. The numbered circles (A1-A4 and B1+B2) are indications of the positions used for different analyses in the rest of this chapter. The orange dashed line on the left in **(a)** indicates the border between areas with and without wormlike defects, this line coincides with the area where the molybdenum stops underneath the absorber, and is analogue to the P1 scribe in a monolithically interconnected module. This line is not shown in **(b)** because it is located far away from the stationary wormlike defects and outside of the cropped area.

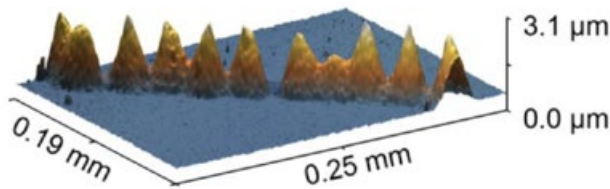
### 5.3.3 Confocal microscopy

Confocal microscopy revealed that wormlike defects consist of a chain of protruding “islands”, often higher than a micrometer above the original surface. Figure 5-6 shows confocal microscope images of samples with two different TCO thicknesses. The stationary wormlike defects (thick TCO) consists of much larger islands compared to the mobile wormlike defects. This trend was observed on all samples. In order to quantify the size of the trails, the islands size is measured at the base of the islands and the spacing between peaks of two islands is measured for a number of different spots.

The average sizes and distances between individual islands as well as the

height of the islands are listed in Table 5-2. On sample I-3 there is a large variation between the different spots. Measurements show that the size of the islands in the beginning of the mobile worm (spot A4) is larger than islands formed at a later stage (spot A1 and A3). A possible explanation for the difference in island size is that trails that have already been formed consume part of the total supplied energy. Therefore less energy is available for the growth of the newer individual islands during the formation of a new trail. The stationary wormlike defects of sample T-2 are, compared to samples with thin TCO, much wider and spaced further apart. This is an indication for a difference in island formation and propagation between the samples with different TCO thicknesses.

**(a)** Thin TCO spot A4



**(b)** Thick TCO spot B1

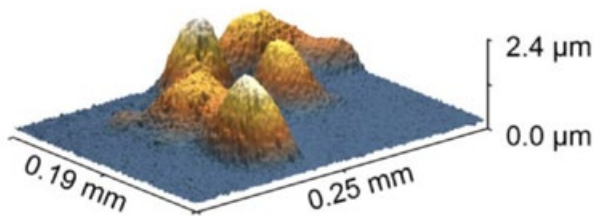


**Figure 5-6:** Confocal microscope pictures of wormlike defects on positions A4 and B1 indicated in Figure 5-5. **(a)** Spot A4 on sample I-3 with mobile wormlike defects and thin TCO. **(b)** Spot B1 is on sample T-2 with thick TCO and stationary wormlike defects.



**Table 5-2:** List of average island parameters obtained with confocal microscopy on the positions indicated with colored circles in Figure 5-5.

Sample	Position	Height [ $\mu\text{m}$ ]	Width [ $\mu\text{m}$ ]	Distance [ $\mu\text{m}$ ]
I-3	A1	$0.4 \pm 0.1$	$19 \pm 5$	$18 \pm 5$
I-3	A2	$1.5 \pm 0.1$	$27 \pm 3$	$28 \pm 6$
I-3	A3	$1.0 \pm 0.3$	$19 \pm 2$	$19 \pm 4$
I-3	A4	$2.2 \pm 0.3$	$31 \pm 3$	$27 \pm 5$
T2	B1	$1.7 \pm 0.4$	$66 \pm 15$	$61 \pm 7$
T2	B2	$1.5 \pm 0.2$	$70 \pm 5$	$63 \pm 4$

### 5.3.4 SEM analyses

SEM-EDX measurements were carried out to study the morphology and composition of the defects. Figure 5-7(a) shows a SEM picture of a wormlike defect after removal of the CdS, *i*-ZnO and Al:ZnO layers on top of the CIGS. The defect itself consists of a very porous expanded material. This material appears to be molten and re-solidified during formation. The defect has a very distinct border and the material in the border region appears slightly darker in the SEM image. Finally, the unaffected bulk of the CIGS material further away from the defect, this is used for comparison.

Compositional changes were identified with the aid of EDX. Elemental maps can be found in Figures 57(b)-(e). The elemental maps are an indication of the presence of the elements and can not be considered in a quantitative way. It should be noted that the peak at 3.29 eV assigned to indium in the EDX analysis also contains a contribution of a secondary cadmium signal. Therefore, the indium signal in Figure 5-7(c) is enhanced by the presence of cadmium. More details on quantitative analyses of the elements in the border region can be found in Chapter 4.3. The defect shows large areas with lower copper content. Since SEM is a surface technique, it is possible that the copper has migrated towards the back contact. This would agree with the findings of Westin *et al.* [33] who found higher copper concentrations at the bottom of defects in cross sections of similar defects. Furthermore, a higher gallium concentration is present in the wormlike defect and the indium seems locally depleted in the defect itself.

Furthermore, cadmium and sulfur (not shown) have piled up in the border region. The presence of these elements is surprising as the cadmium sulfide should have been etched away by the HCl. Some possible explanations are:

- (i) The CdS could have reacted to form a compound that is more resilient to the HCl etch.
- (ii) The CdS could have diffused into the CIGS material where it is more difficult to be etched

The pile-up of cadmium combined with the observed changes in composition show that the material in the border region was altered during formation of the defect. In order to study these changes in more detail Raman spectroscopy was performed on the border regions of several defects.

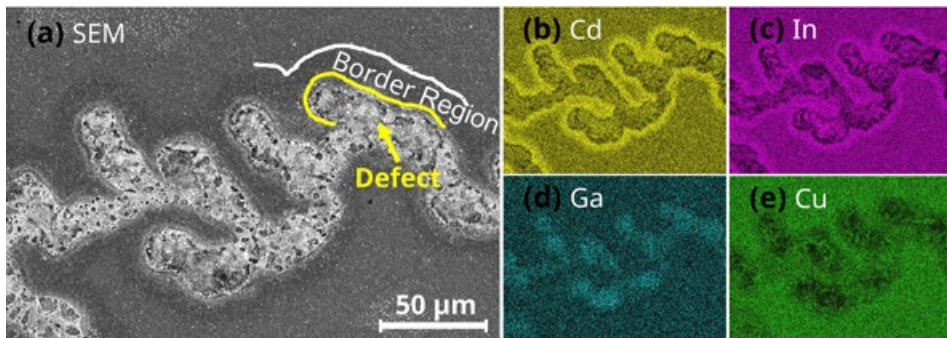


**Figure 5-7:** SEM-EDX images of a wormlike defect after HCl etching on sample with thin TCO on spot A3 in Figure 5-5. **(a)** SEM image. EDX images of elements **(b)** Cd, **(c)** In, **(d)** Ga, and **(e)** Cu.

### 5.3.5 Raman spectroscopy

Raman is a non-destructive technique that probes an area of approximately 1–2 μm in diameter with a laser. The material inside the wormlike defect changed to an extent that non-chalcopyrite Raman signals are introduced. These additional signals are non-uniformly distributed over

the wormlike defects and often combined into an incoherent mixture of all kinds of phases. However, Raman measurements in the border regions outside the defect give insight in compositional and structural changes that can be related to the propagation mechanism. In Figure 5-8 the results of a Raman line-scan are plotted. Raman signals away from the defect (top spectrum) are comparable with “as-deposited” (not shown) measurements taken before reverse bias exposure and show a typical Cu(In,Ga)Se<sub>2</sub> (CIGS) fingerprint. Features that are found in this CIGS spectrum include a dominant peak around 175 cm<sup>-1</sup>, two smaller peaks around 218 and 249 cm<sup>-1</sup>, and a very small feature at 305 cm<sup>-1</sup>. These peaks are commonly assigned to:

- (i) CIGS A<sub>1</sub> mode around 175 cm<sup>-1</sup> where its position has a linear relation with the gallium content of the absorber [55].
- (ii) Mixed B<sub>2</sub>/E acoustical vibration modes in CIGS [55], for these samples around 218 and 249 cm<sup>-1</sup>.
- (iii) The peak around 305 cm<sup>-1</sup> is associated either with the A<sub>1</sub> mode of Cu(In,Ga)S<sub>2</sub> [56] or the A<sub>1</sub> mode of CdS [57] and will therefore be referred to as the A<sub>1</sub>X peak.

The most obvious change in the spectra of Figure 5-8 is the emerging A<sub>1</sub>X peak when approaching the defect. This peak is still present but hardly distinguishable far away from the defect. Other changes, besides the A<sub>1</sub>X peak, were observed in the Raman spectra in the border regions. These changes are not directly visible in the spectra of Figure 5-8, therefore Raman parameters as function of distance from the edge of the defect are plotted in Figure 5-9. In this figure, four datasets are combined because the observed trends becomes more pronounced with additional data points. These trends are, to a lesser degree, also present in the samples with thick TCO. The black dashed line in all graphs of Figure 5-9 represents the as-deposited value, all three parameters start deviating from this line at a distance between 10 and 20 μm.

Figure 5-9(a) displays the position of the main CIGS A<sub>1</sub> peak versus the distance to the edge of the defect. In this graph it is observed that the peak position shifts towards lower wavenumbers for points closer to the edge. A shift in the CIGS A<sub>1</sub> peak position can be attributed to strain in the lattice [55] or changes in gallium [7,55] and copper [7] concentrations. Besides the position also the full width at half maximum (FWHM) of the CIGS A<sub>1</sub> peak

is changing. (Figure 5-9(b)). Broadening of the  $A_1$  peak is observed in the vicinity of the defect edge and can be caused by an increased amount of lattice-defects or reduced crystallinity [7].

In order to visualize the increasing magnitude of the  $A_1X$  peak, the ratio of the area of the  $A_1X$  peak to the main  $A_1$  CIGS peak is plotted with respect to the distance of the edge of the defect in Figure 5-9(c). It is clear that the contribution of the  $A_1X$  peak shows a strong increase, starting around 20  $\mu\text{m}$  from the edge, towards the edge of the defect.

One possible explanation for the emerging  $A_1X$  peak is the presence of CdS. Oliva *et al.* [57] stated that a green laser can be used to quantify CdS layer thickness by studying the peak at 600  $\text{cm}^{-1}$ . In order to investigate if the  $A_1X$  peak originates from the CdS additional Raman measurements with green laser excitation were performed, both before and after the solar cells were etched with HCl to remove the CdS and overlying layers.

Figure 5-10 shows normalized Raman data obtained with a green laser before and after etching. Before etching the spectra are dominated by the contribution of the CdS on both positions. The CdS contribution is accompanied by a strong reduction of the CIGS signal and characterized by two Raman peaks around 305 and 600  $\text{cm}^{-1}$ . An additional effect of excitation with a green laser is an enhancement of the (luminescent) background signal from the CdS. After etching the green laser Raman signal, up to 350  $\text{cm}^{-1}$ , is almost identical to the spectrum for the red laser (not shown). These results confirm that the CdS and its Raman contribution were successfully etched away in the region far away from the defect. However, close to the edge of the defect the CdS contributions at 305 and 600  $\text{cm}^{-1}$  are still present after etching. This means that CdS is still present close to the edge of the defect after etching, confirming the observations in the border region with the SEM-EDX measurements. Moreover, it was found that a high ( $A_1X/A_1$  CIGS) ratio measured with the red laser is accompanied by a dominant CdS Raman signal with the green laser after etching. Also a peak around 450  $\text{cm}^{-1}$  was observed for all measurements with the green laser after etching. The origin of this peak is still unknown but less relevant as this peak is also present in the bulk of the sample. Additionally to the Raman peak around 450  $\text{cm}^{-1}$ , also a reduction of the luminescent background signal was observed after etching for all measurements.

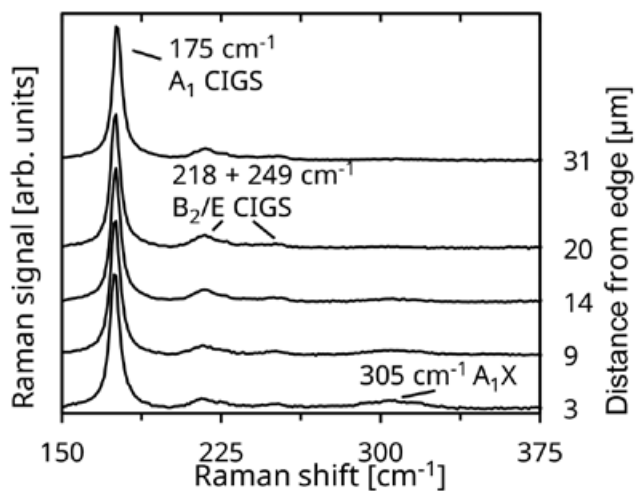


**Figure 5-8:** Normalized red laser Raman spectra after baseline correction. On the right axis the progressing distance from the edge of defect at spot A4 in Figure 5-5(a) is displayed.

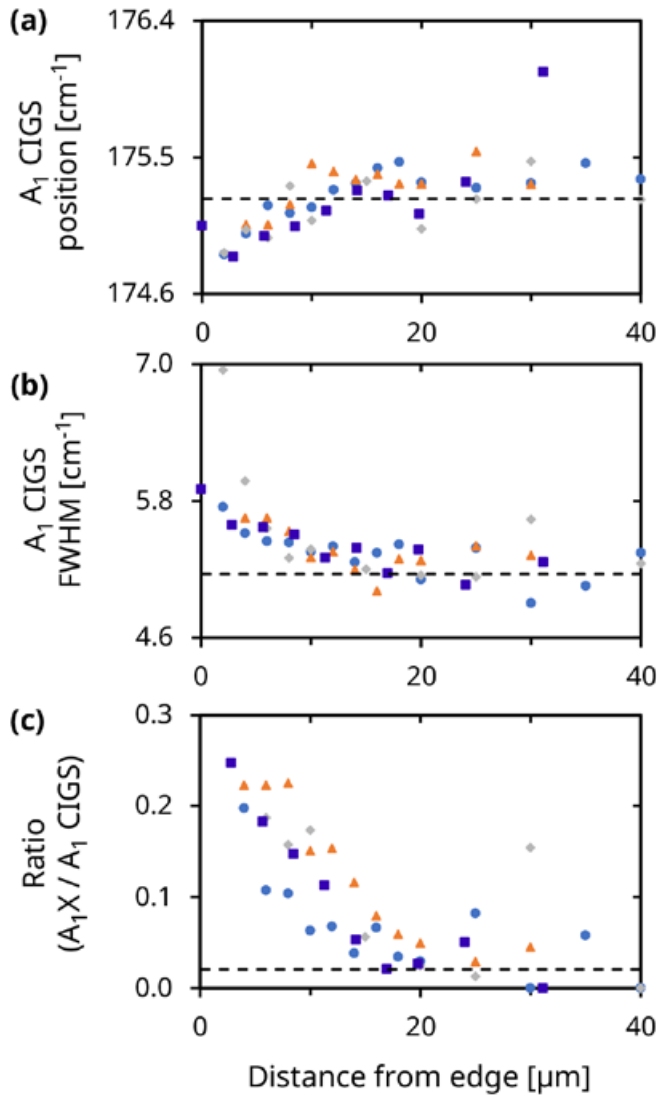


**Figure 5-9:** Raman parameters plotted versus distance to the edge of the defect, with on the y axis: **(a)**  $A_1$  CIGS peak position, **(b)**  $A_1$  CIGS FWHM and **(c)**  $A_1X$  to  $A_1$  CIGS area ratio. For all graphs the as-deposited values are represented by a horizontal black dashed line. Four datasets were measured on sample (I-3) with thin TCO, the positions are indicated in Figure 5-5(a). Each data set has a different color and symbol.

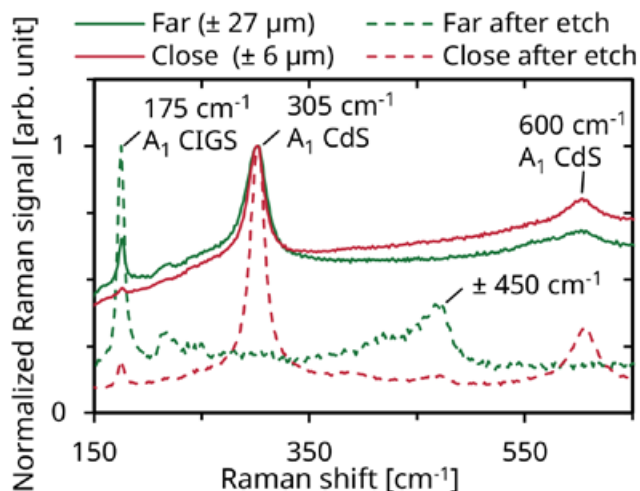


**Figure 5-10:** Normalized Raman spectra of measurements with green laser before and after HCl etching on a spot close to the edge of the defect and a spot far away from the edge of the defect. Solid lines represent measurements before etching, dashed lines represent measurements after etching. Red lines are near the edge ( $\pm 6 \mu\text{m}$ ) of defect A4 and green lines are measurements on a spot far ( $\pm 27 \mu\text{m}$ ) from the edge of the defect A4 of sample I-3.

## 5.4 Discussion

Ten samples were exposed to strong reverse bias conditions. Two of these cells survived the harsh reverse bias and did not exhibit wormlike defects. In eight samples wormlike defects were formed and the efficiency of these cells was severely reduced. In these cells a large variation in the electrical conditions related to the formation of wormlike defects were measured. Two distinct propagation patterns were observed: mobile wormlike defects in samples with thin TCO and stationary wormlike defects in samples with thick TCO layers. These different propagation patterns were linked to the propagation voltage and the lateral conductivity of the TCO. Therefore, it is likely that the propagation is depending on an electric field. Furthermore, it was observed that both mobile and stationary wormlike defects consists of individual islands. This points to a propagation process based on island hopping where the hotspot or epicenter jumps from one position to

another. The final important clue for the proposed propagation mechanism is the alteration of CIGS material properties in the border region at the edge of the defect.

#### 5.4.1 Compositional changes in the border region

A first indication of alterations in the CIGS material at the edge of the wormlike defects can be found in the strong presence of CdS signals in both Raman and EDX measurements. The cadmium sulfide is expected to be etched away during the HCl treatment. A potential explanation for its presence could be the diffusion of CdS molecules into the altered CIGS material during formation of the wormlike defect. Another clue for diffusion of CdS molecules into the absorber material is the reduction of the background signal in the Raman spectra after the HCl etching (Figure 5-10). The background signal in the spectrum before etching could originate from the luminescence of CdS on top of the CIGS. After etching, the CdS on top of the CIGS is removed and only the CdS that is diffused into the altered CIGS material is left. The luminescent signal of CdS embedded in CIGS is quenched and/or absorbed by the surrounding CIGS.

Another possibility is that cadmium and sulfur diffuse separately as ions. Cadmium is known to diffuse from the buffer layer into the CIGS absorber layer under the influence of heat. In Chapter 4 defect levels indicating Cd<sub>Cu</sub> antisites in the border regions of wormlike defects were described. Furthermore, Guthrey *et al.* [51] showed cadmium diffusion into the absorber in the propagation front of wormlike defects. Probably the presence of Cd is caused by a combination of diffused CdS molecules and cadmium ions. The diffusion of cadmium into the absorber will change the electrical behavior of the solar cell in the forward region [47]. At reverse voltages the buffer layer is known to play an important role in the reverse electrical characteristic [30,39]. Considering these two facts it is likely that the pile-up of CdS is changing the electrical behavior in the border region. Lee *et al.* [29] reported an involvement of the buffer layer (both CdS and Zn(O,S)) in the formation of wormlike defects by partial shading on commercial CIGS modules.

Besides changes in the buffer layer, also indications for compositional changes in the CIGS absorber layer in the border region of the defect were found. SEM EDX measurements showed a redistribution of elements, a



more detailed description of the EDX results is presented in Chapter 4.3. The redistribution of indium and gallium as observed in EDX was confirmed by Raman measurement in the form of a shift in  $A_1$  CIGS peak position. Furthermore, a broadening of the this main Raman peak was observed in the border region. Broadening of the FWHM of the main CIGS  $A_1$  peak in Raman indicates a change in the crystallinity and/or in the number of lattice defects. Therefore, the elemental changes are likely accompanied by changes in the crystal lattice.

Based on the measurements, it is likely that subtle changes took place in the border region. We assume that these changes altered the electrical and chemical properties, which makes the material in the border region more vulnerable to the start of a new island.

### 5.4.2 Electric field

There are two observations besides the propagation voltage that indicate a dependency of the propagation mechanism on the electric field over the CIGS material. Firstly, the field between Mo and TCO as the wormlike defects did not propagate into areas without Mo. This implies that an electrical connection (conductive path) between front and back contact is needed for the wormlike defect to propagate. Secondly, the difference in size and spacing of islands between the mobile and stationary wormlike defects. The stationary wormlike defects were found only on samples with thick TCO. A thicker TCO has a higher conductivity and therefore the voltage drop over the thick TCO in case of equal current is much lower compared to TCO with normal thickness and conductivity. Because of this reduced voltage drop in samples with thicker TCO the electric field between molybdenum and TCO will be smaller for these samples in the region close to the defect.

The electric field near the defect consists of several contributions. The main contributors are displayed in Figure 5-11 and are: voltage drop over TCO, voltage losses in interfaces, and voltage drop inside the defect. It should be noted that negligible contributions like the Mo resistance are omitted. Since the voltage drop over the defect can not be neglected, it is shown as equal in both cases and only the ratio of losses in the TCO and the interfaces was changed.

The voltage drop over the TCO is the only contribution to the electric field

that has a dependency on the distance to the defect. An estimation of the voltage distribution ( $V(r)$ ) over the TCO close to a point-defect can be made using the solution of the Laplace's equation with cylindrical coordinates [58] given in equation (5-1). Assuming that an isolated island in a wormlike defect acts as a point defect.

$$V(r) = \ln\left(\frac{r}{r_0}\right) \times \frac{I \times R_{sheet}}{2\pi} \quad (5-1)$$

In this equation  $r$  is the distance from the center of the point-defect in meter,  $r_0$  is the radius of the point-defect in meter,  $I$  is current through the defect in Ampère and  $R_{sheet}$  is the sheet resistance in Ohm. From equation (5-1) it can be concluded that the size of the defect ( $r_0$ ) has a large influence on the voltage gradient in the TCO: a bigger defect gives less voltage loss in the TCO. A calculation of the influence of the sheet resistance on the voltage drop over the TCO with respect to the distance of the defect is plotted in Figure 5-12. The sheet resistance has a linear relation to the voltage loss in equation (5-1). In Figure 5-12 it is observed that the voltage drop is doubled when the resistance is reduced by 50 %.

Another major contribution to the electric field near the defect are the resistive losses at the interfaces, as shown in Figure 5-11. These are both 'defect – TCO' and 'Mo – defect' interfaces. It should be apparent that when the island grows and becomes more porous, the interface between the layers will change. For instance, the contact area between the defect and the TCO is reduced due to voids between the defect and the TCO when the CIGS material expands and become more porous. An increase in contact resistance is expected for larger islands due to the relative loss in contact area and the changed (electrical) interface properties. Figure 5-11(c) shows an estimation of the relative contribution to the electric field close to the defect for cells with thin and thick TCO. The voltage loss over the TCO is smaller for cells with a thick TCO layer. This can be explained by the higher conductivity of the thicker TCO layer and the larger size ( $r_0$  in equation (5-1)) of the islands, that were observed on samples with thick TCO. Therefore, a relation of the interface resistance with the size of the islands would explain why the islands have to expand more to get the same electric field required for propagation. The larger size of the individual islands increases the contribution of the contact resistance to reach the required voltage needed for island hopping.

The last contribution to the electric field is the voltage loss in the defect itself. The CIGS solar cell material has the biggest influence on this contribution as should be clear from Figure 5-4, that shows the dependency of the propagation voltage on the different CIGS runs. The current flow in the defect is a combination of current flowing through the altered material at the edge of the defect and through the epicenter itself. For the propagation mechanism that is proposed in the next section, the majority of current has to flow through the epicenter. In this study a constant current was supplied during defect formation. Therefore, the current density in the edge would drop as the area of affected material at the edge grows when an islands expands. When more islands are created during the formation of a wormlike defect the current would be diluted, consequently the ohmic heating would spread out over a larger area. Because of this a propagation mechanism where the majority of the supplied current flows through the edge seems less likely. Ohmic heating at the edge of the defect would also not explain the difference in propagation mechanism between the two different TCO layers. A mechanism where after the epicenter has hopped to a new island the old island cools down and the current flow through the old island is reduced is more likely.

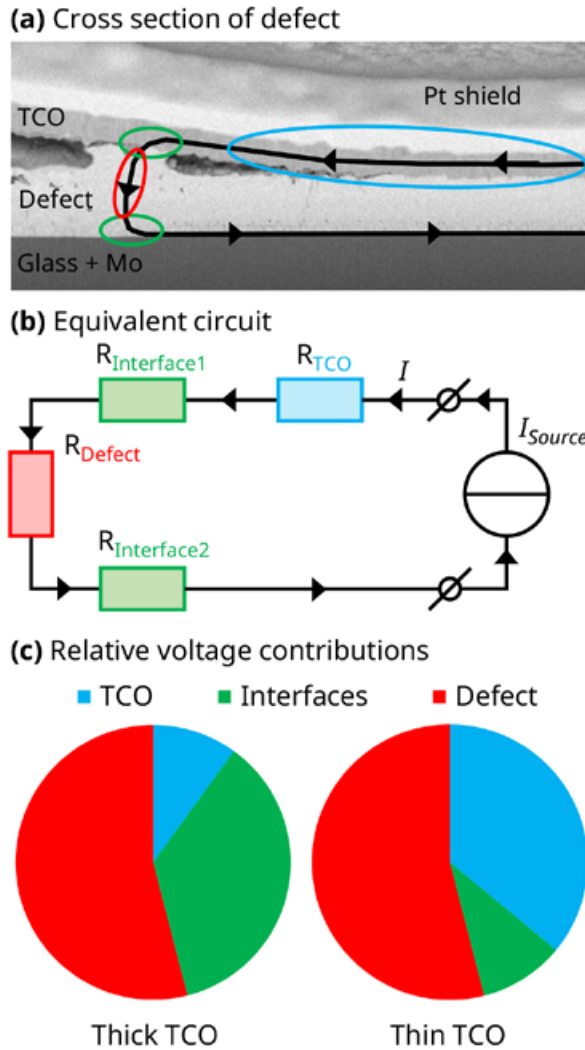


**Figure 5-11:** Visualization of voltage losses inside and near the defect. **(a)** SEM cross-section of a wormlike defect with indications of current flow and resistive losses. **(b)** Equivalent circuit showing the resistive elements indicated in (a). **(c)** Pie charts showing an estimation of the contribution of the different voltage losses to electric field close to the defect for cells with thick and thin TCO. The current flow in (a) and (b) is indicated with a black line and the direction of the current is given with arrows. In all figures the colors blue, green, and red represent the TCO, the interfaces with the defect, and the defect itself, respectively.

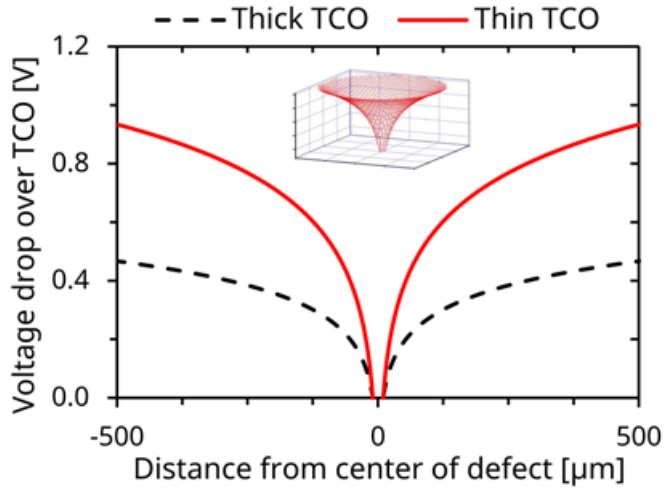


**Figure 5-12:** Voltage loss over TCO as function of distance to the center of the defect. Calculated from equation (51), assumptions made for current and the radius of defect are 100 mA and 10  $\mu\text{m}$ , respectively. The center of defect is at 0, the voltage inside the defect is not plotted. Two different sheet resistances are used: thick TCO (black dashed line) 7.5  $\Omega$  and thin TCO (red line) 15  $\Omega$ . The inset shows a 3D representation of the voltage drop over the TCO, for the calculation of the sample with thin TCO. Both horizontal axis show distance and the vertical axes shows the voltage drop.

### 5.4.3 Proposed propagation mechanism

In order to explain the formation of wormlike defects two effects need to be explained:

- (i) The formation and expansion of the individual islands.
- (ii) The hopping of an islands to a neighboring region.

For the proposed mechanism the formation and expansion of the individual islands is based on a chemical reaction. This reaction forms the epicenter of the moving hotspot. The temperatures inside the epicenter are high. The origin of the heat generation could be the chemical reaction itself, ohmic heating due to the high current density, or a combination

of both heat sources. Furthermore, the reaction is responsible for the observed change in material properties inside the wormlike defect. The reaction requires at least:

- (i) Fuel, which is in the form of elements or reactants that are supplied from outside the epicenter.
- (ii) Electricity, the reaction needs a minimum electric field to get started and a current to sustain itself. This is, analogue to a plasma; a plasma needs a high voltage to ignite and current to maintain its state.

Heat generation during the island formation is considerable, it is less evident if the reactions requires heat to start or to sustain itself.

The hopping mechanism involves the creation of a nucleus, allowing the formation of a new island. Nucleation occurs in the neighboring region of the epicenter. This area is referred to as the nucleation zone. Key elements needed for the nucleation that are present in the nucleation zone are:

- (i) Poor material quality that provides plenty of seeds to start a nucleus: this is present in the modified material in the border region as evidenced by Raman spectroscopy and EDX measurements.
- (ii) Electric field: as shown with confocal microscopy, there is a strong dependence between the spacing of the islands and TCO thickness. The nucleation zone is shifted away from the epicenter in case of reduced field in cells with thick TCO.
- (iii) Heat: the nucleation is probably aided by the elevated temperature in the nucleation zone.

Figure 5-13 shows a schematic of the proposed propagation mechanism. The stages of propagation are:

- 1) Initial starting point. This could be a shunt or other local fault in CIGS material as shown by Palmiotti *et al.* [35].
- 2) Due to high current density the defect starts to heat up and becomes a local hotspot.
- 3) Due to heat and electricity a reaction starts. Reactants are provided by the neighboring material. The diffusion of reactants

- is boosted by the elevated temperature in the border region.
- 4) The island is expanding and the material in the border region is weakened. In the border region material changes take place due to the vacancies left by the diffused reactants. The supply of reactants gets more difficult over time since the border region starts to get depleted and reactants have to travel a greater distance. A nucleation zone with favorable conditions for propagation is formed. Favorable conditions include; heat, electric field and poor material quality.
  - 5) A new reaction site is created from a nucleus. The supply of reactants in this new region is fresh and the gravity of the electric current flow is redirected towards the new site and the old islands starts to cool.
  - 6) A new hotspot is formed and the reaction starts from 1.

This proposed propagation mechanism based on islands hopping explains the observed discrete islands that make up wormlike defects. Also, the dependency on electric field in the model can account for the difference between mobile and stationary wormlike defects in relation to the different TCO thicknesses on the cells.

## 5.5 Conclusions

In this chapter the propagation model introduced in Chapter 4 for the propagation of reverse bias induced “wormlike” defects in CIGS is extended. In this model, a moving hotspot leaves a trail of damaged CIGS material. The moving hotspot consists of a chemical reaction that hops from islands to island. Conditions required for island hopping are: poor material quality, electric field, and heat. The mobility of the hotspot can be influenced by altering the electric field near the defect by changing the TCO thickness. Thicker TCO confines the defects, the area affected is less big, and the wormlike defects do not always reach the interconnect. Power loss was less severe for wormlike defects that did not extend to the interconnection and two cells survived the harsh reverse bias exposure without the formation of wormlike defects. Hence, the negative impact on module output due to partial shading will be reduced when using cells with thicker TCO, this shows that the propagation of wormlike defects can

be mitigated.

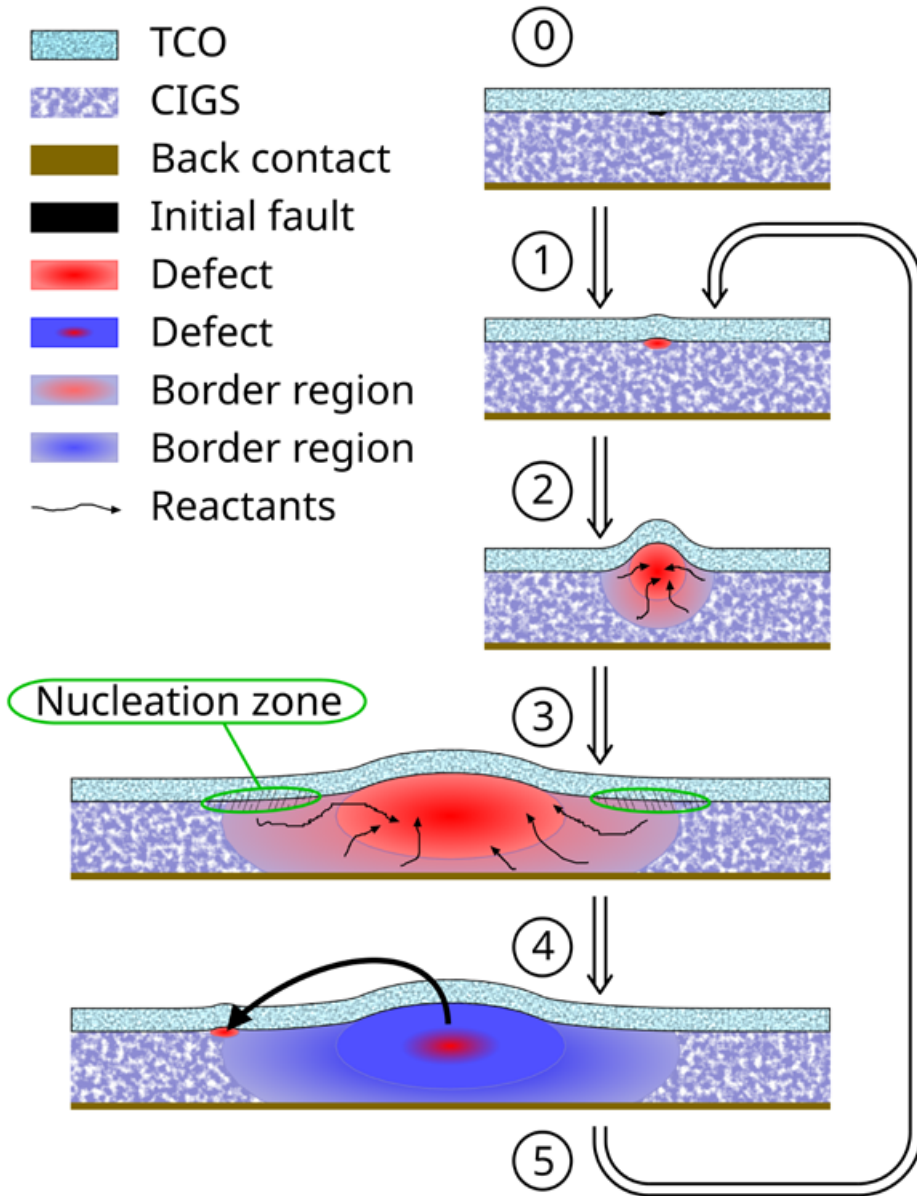


**Figure 5-13:** Schematic representation of the proposed propagation mechanism.







## CHAPTER

How the absorber  
thickness influences the  
formation of reverse  
bias induced defects  
in CIGS solar cells

This chapter is based on the following publication:

K. Bakker, A. Rasia, S. Assen, B. Ben Said Aflouat, A. Weeber, and M. Theelen, "How the absorber thickness influences the formation of reverse bias induced defects in CIGS solar cells," *EPJ Photovoltaics*, vol. 11, no. 9, Nov. 2020, doi: 10.1051/epjpv/2020006.

## Chapter 6

# How the absorber thickness influences the formation of reverse bias induced defects in CIGS solar cells

**ABSTRACT:** When a PV module is partially shaded, the shaded solar cells operate in a reverse bias condition. For  $\text{Cu(In,Ga)Se}_2$  cells this condition can cause defects that irreversibly reduce the output of these cells and the full module. In order to design robust shade-tolerant CIGS modules details need to be known of the conditions at which these defects will be formed. In this study a large number of cells were exposed to different reverse bias conditions. By using simple statistics the probability of the occurrence of defects as a result of reverse bias at any given voltage was determined. Based on our experiments we have found that the absorber thickness is one of the main parameters that affects the shade-tolerance: the thicker the absorber, the more shade tolerant the CIGS module will be.

### 6.1 Introduction

Partial shading of photovoltaic (PV) modules can lead to reverse bias voltages in the shaded cells. In  $\text{Cu(In,Ga)Se}_2$  (CIGS) modules this reverse bias condition can lead to the formation of reverse bias induced defects or wormlike defects [Chapter 3]. Wormlike defects act as local shunts and permanently reduce the output of a PV module.

Mitigation against reverse bias damage is often obtained by the integration of bypass diodes, especially in wafer-based crystalline silicon PV modules this is standard practice. However, the integration of bypass diodes in monolithically interconnected CIGS modules, the most commonly used type of CIGS modules, is almost impossible. Another possible mitigation option against reverse bias damage in CIGS is to utilize the CIGS solar cell itself as a bypass diode, as proposed by Silverman *et al.* [28]. This would

be feasible because the reverse characteristic of a CIGS solar cell shows a very steep incline in reverse current, like a Zener or avalanche breakdown [40,41]. From literature it is known that both the buffer layer thickness and composition have a strong impact on the reverse characteristic [30,39,41], as well as the sodium content in the absorber layer [40,42]. On the other hand, it has been observed that the absorber layer thickness does not have a large influence on the reverse characteristic [43]. In order to successfully utilize the CIGS cell as a bypass diode, the formation of wormlike defects should be prevented and therefore the reverse characteristic needs to be shifted to stay below the damage threshold. Recent studies presented in references [38,43] on the threshold conditions at which wormlike defects are formed are not conclusive and show huge variations in results. In this study a large number of cells with varying absorber layer thicknesses were exposed to extreme conditions in order to determine the impact of reverse bias on cell performance and simultaneously obtain sufficient statistics.

## 6.2 Experimental

The CIGS solar cells were fabricated using the three stage co-evaporation process [59]. The layer stack consists of: 400 nm direct current (DC) sputtered Mo, CIGS with varying thickness and composition, 50nm chemical bath deposited CdS, 60 nm DC sputtered intrinsic zinc oxide, 210 nm DC sputtered aluminum-doped zinc-oxide and a metal current-collecting grid (20 nm Ni, 600 nm Ag, 20 nm Ni) applied with e-beam evaporation. These layer stacks were deposited on 1 mm soda lime glass (SLG) substrates with a dimension of  $100 \times 100 \text{ mm}^2$  and manually divided in 162 individual cells, each with a dimension of approximately  $5 \times 10 \text{ mm}^2$ , with a scalpel.

In this study three groups of cells were used:

- Group I: 6 substrates, absorber thickness varying between 237 and 965nm. The composition and thickness distribution for this group is less uniform than the other two groups. Furthermore, the reverse bias measurements were performed 5 months after fabrication with a slightly lower scan speed than the other two groups.
- Group II: 3 substrates, thickness between 524 and 604nm. Furthermore 5nm of NaF was evaporated before CIGS deposition, to increase the initial efficiency.
- Group III: 6 substrates, thickness between 1479 and 1984 nm.

The average thicknesses of the individual substrates are included in Table 6-1.

*JV* measurements were performed in an automated setup that measures both in darkness and under illumination. As illumination source a Newport Xenon lamp with AM1.5 filter was used. To perform the *JV* sweeps in forward and reverse a Keithley 2400 source measure unit (SMU) was used. The SMU was set to automatically change the current range and the current compliance was set to 100 mA (200 mA/cm<sup>2</sup>). The voltage step used for all *JV* sweeps was 20 mV, with the exception of the reverse sweep of group I which was 10 mV.

For the reverse *JV* sweeps in the dark (DRB) the start voltage was +0.72 V and end voltage was -6 or -15 V for the substrates of group I and II and group III, respectively. For the illuminated reverse *JV* sweeps (LRB) the start and end voltages were +0.72 and -6 V, respectively.

The calculations of average, standard deviation and normal distribution were performed with the built-in functions of Excel. The damage parameters are determined from the derivative curve using a Matlab script that had a manual control and correction option built-in.

**Table 6-1:** List of substrates used including for each substrate the average absorber thickness, solar cell efficiency, and damage voltage for both the dark (DRB) and illuminated (LRB) reverse bias sweeps. The average values are based on at least 22 measurement points per substrate, the error bar presented is the standard deviation. Several values are missing in the last column (damage voltage in LRB), due to the low number of damaged cells ( $n < 20$ ) needed to give a reliable estimate. The table also displays the damage ratio in both dark reverse bias and illuminated reverse bias, together with the number of cells ( $n$ ) used to calculate this ratio

Substrate	Absorber thickness [nm]	Efficiency [%]	n cells DRB	DRB damage ratio [%]
Group I-a	262±12	7.3±0.4	76	100%
Group I-b	433±22	9.9±0.5	27	100%
Group I-c	468±23	8.0±0.4	60	100%
Group I-d	503±25	9.7±0.4	73	100%
Group I-e	517±25	9.0±0.3	76	100%
Group I-f	889±45	13.6±0.4	78	92%
Group II-a	545±10	11.7±0.4	47	100%
Group II-b	580±10	11.6±0.7	51	96%
Group II-c	586±11	11.4±0.4	69	94%
Group III-a	1567±37	13.2±1.1	36	97%
Group III-b	1585±39	13.6±1.5	36	97%
Group III-c	1696±47	12.2±0.9	36	100%
Group III-d	1721±38	13.2±0.9	35	100%
Group III-e	1787±38	13.7±0.5	35	91%
Group III-f	1910±43	15.3±1.2	36	97%

DRB damage voltage [V]	n cells LRB	LRB damage ratio [%]	LRB damage voltage [V]
2.5±0.4	22	100%	2.4±0.7
2.7±1.0	35	100%	3.0±0.2
2.9±0.4	43	98%	2.7±0.3
3.0±0.6	43	100%	3.2±0.4
2.9±0.7	50	100%	3.2±0.5
3.7±1.1	24	42%	...
4.0±0.9	17	12%	...
3.9±0.8	28	21%	...
3.9±0.8	34	38%	...
4.7±0.7	35	11%	...
4.6±0.6	36	6%	...
6.7±2.4	35	6%	...
7.8±1.9	36	0%	...
7.6±1.8	32	3%	...
6.7±2.0	31	0%	...



## 6.3 Results

In general, the formation of a wormlike defect during the  $JV$  sweep is accompanied by a sudden sharp increase in current (see Chapter 5.3) of which an example is given in Figure 6-1. At the moment the sudden sharp increase in current occurs, the cell will be irreversibly damaged. The parameters at this point are labeled as damage voltage and damage current density. Since not all cells got damaged by the sweep a damage ratio was defined as the number of damaged cells divided by the number of cells measured. A cell is considered to be damaged in the analysis in case the fill factor has been reduced by more than 3 % relative. Cells that were bad ( $<0.85$  times the efficiency of 11th best cell) before the reverse bias sweep were excluded from the statistical analysis. The average results of the damaged cells of each substrate are summarized in Table 6-1. Two clear trends can directly be observed from this table. First, the damage voltage in DRB shifts to lower negative voltages with increasing layer thickness. Second, the damage ratio in darkness and under illumination are different. The LRB damage ratio is decreasing with increasing absorber layer thickness. Furthermore, for the substrates with thicker absorbers almost no cells got damaged under illumination. In order to examine the trend in the DRB damage voltage for the individual cells, the damage voltage in DRB is plotted against the absorber thickness and presented in Figure 6-2. The efficiency is added in a color scale, and can be seen as an additional dimension to the plot. From this plot it is evident that there is a large variation in damage voltage, which was also observed by Mansfield *et al.* [43] and Richter *et al.* [38].

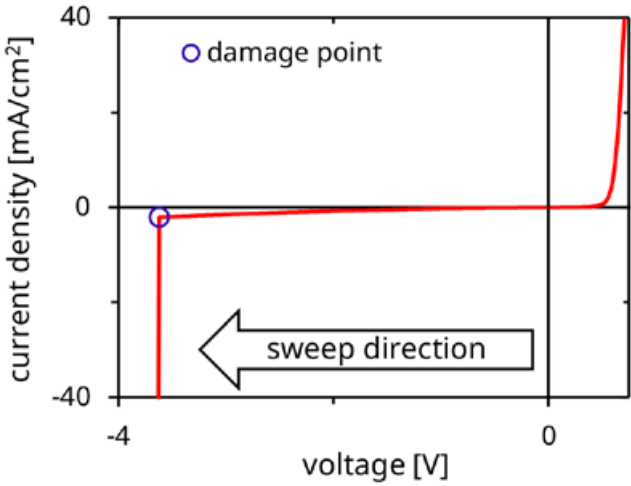


**Figure 6-1:** *JV* graph of a cell that was damaged during the *JV* sweep. The moment when the cell was damaged and a wormlike defect started to form is accompanied by a sharp increase in current. This damage point is indicated with a purple circle in the graph.

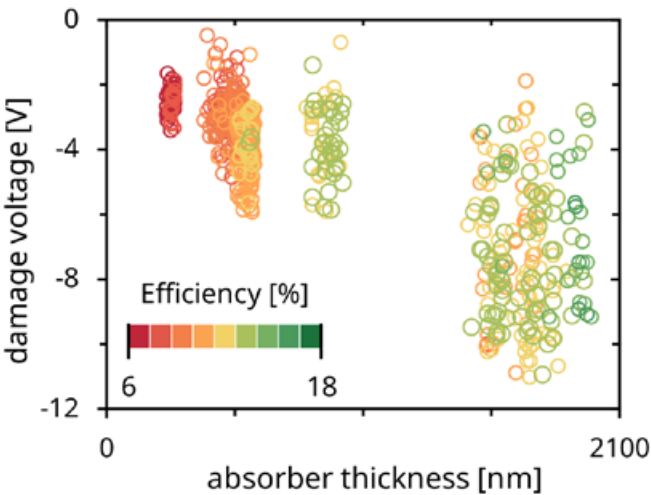


**Figure 6-2:** Damage voltage for dark reverse bias as function of absorber thickness. The initial efficiency of the individual solar cells is represented with a color scale.

The variations for the three groups of substrates including their fitting to normal distribution curves are plotted in the histograms of Figure 6-3. In order to validate if this normal distribution can be used to estimate the damage probability additional DRB measurements until -6 V were performed on 425 cells of the group III substrates. The measured damage ratio of the  $JV$  sweep until -6V is 28.0 %, while the damage probability calculated from the normal distribution in Figure 6-3, is 28.4 %. Because these two percentages are in very good agreement we propose that fitting the occurrence of failure to a normal distribution can be used to determine the probability of having cells damaged due to reverse bias at any given voltage.

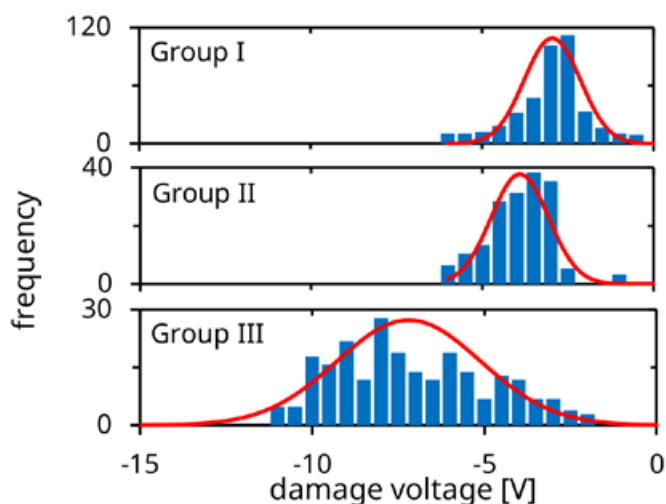


**Figure 6-3:** Histograms of damage voltage in dark reverse bias sweep and the normal distribution curve based on average and standard deviation for all three groups of substrates.

Figure 6-4 shows a typical reverse  $JV$  curve in the dark and under illumination together with the damage probability curve in the dark for each group of cells. From this figure it can be seen that the reverse curves under illumination and in darkness are completely different. Both curves have a steep incline in current, however, this transition happens at much higher negative voltages in the dark. This behavior is also observed by

references [30,40]. One possible strategy to reduce reverse bias damage is to shift this transition to more positive voltages. All cells used in this study have a very late transition in the dark ( $< -6$  V). However, the illuminated curves can be used in order to assess if a shift of the transition towards a more positive voltage reduces the probability of reverse bias damage.

The SMU is limiting the current density to  $200 \text{ mA/cm}^2$ , therefore the voltage during the sweep cannot exceed the voltage at  $200 \text{ mA/cm}^2$ . As an example, the voltage at  $200 \text{ mA/cm}^2$  is  $-3.5 \text{ V}$  when using the illuminated curve from Figure 6-4. The calculated damage probabilities at  $-3.5 \text{ V}$  are 74.9 %, 31.3 % and 3.9 % for group I, group II and group III, respectively. These numbers agree well with the actual damage ratios for group II and III, especially when considering that there is also a large variation in the voltages at  $200 \text{ mA/cm}^2$ . The results of group I are influenced by the substrate Group I-f, this substrate has a thicker absorber and thus a much lower average damage voltage and damage ratio.

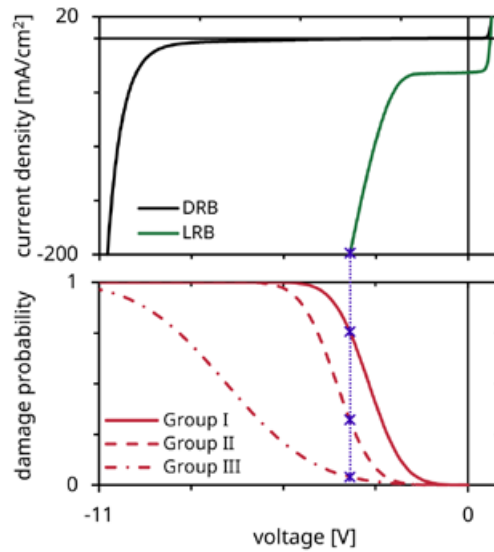


**Figure 6-4:** The top graph shows typical  $JV$  curves of illuminated and dark reverse characteristic. The red curves plotted on the bottom graph represent the damage probability in the dark. The damage probability is the accumulated normal distribution from DRB measurements, a damage probability of 1 means a 100 % chance of failure due to reverse bias. The purple dotted line shows the voltage at the current limit of the LRB  $JV$  curve.

A closer inspection of the current densities at which the cells fail is given in the histogram of Figure 6-5. This histogram shows that a large number of cells got damaged at current densities of  $-2$  and  $-20$  mA/cm<sup>2</sup>. This coincides with the change in measurement range of the SMU (1 and 10 mA). This implies that the SMU could have an influence on the damage voltage. Because of the loss of measurement accuracy at a fixed current range, the SMU was not set to a fixed current range. Additional measurements (Appendix B) showed that the average damage voltage shifts less than 0.5 V when a fixed current range is used instead of a changing. Furthermore, there is a good agreement between dark and illuminated damage voltage while there is no changeover during illuminated measurements due to the additional light generated current. These observations give sufficient confidence in the validity of the damage voltage determined from reverse *JV* sweeps with a SMU that is set to automatically change the current range.

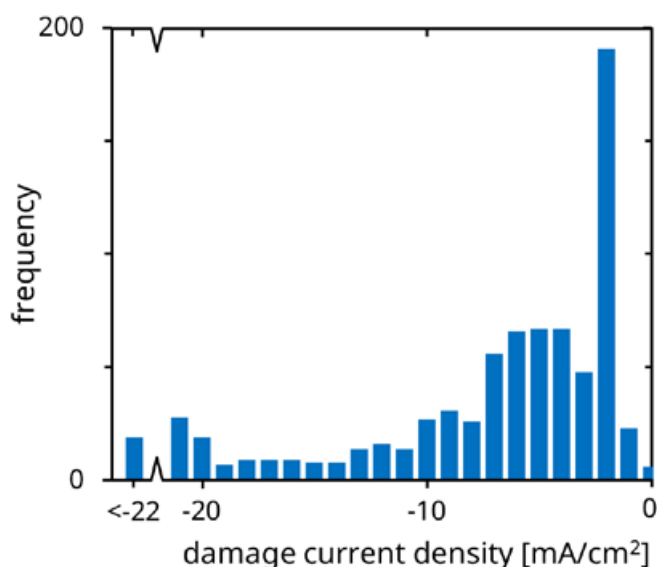


**Figure 6-5:** Histogram of damage current density in dark reverse bias sweeps for all samples. The last bin (most left) represents the total number of cells with a damage current density smaller than 22 mA/cm<sup>2</sup>.

The value of  $200 \text{ mA/cm}^2$  to limit the current density is much higher than realistically can be expected in real life modules. However, this value does indicate the robustness of the cells, especially given the low damage ratios in the group III illuminated reverse bias measurements. Figure 6-5 reveals that only 15 out of the 676 cells exhibit a damage current exceeding  $22 \text{ mA/cm}^2$  absolute. This indicates that the damage mostly appears in the flat part of the curve. Combined with both the relation of the damage voltage in the dark and the damage ratio under illumination with absorber thickness makes us conclude that the mechanism for damage is voltage driven rather than current.

## 6.4 Discussion

In the result section it is described that the formation of wormlike defects is a voltage driven process and that there is a correlation between the damage voltage in the dark and the absorber thickness. The reason for thinner cells to be more prone to damage might be inherent to the layer thickness but can also be an indirect consequence of the absorber growth process. For example, sodium concentration, gallium gradient and grain size distribution could all be different for thinner absorbers.

An inherent difference between absorbers with different layer thickness is the internal electric field. This is the applied potential difference between the front and back electrode distributed over the absorber layer. The exact distribution is hard to predict and requires extensive electrical device modeling. Mansfield *et al.* [43] hypothesized that the enhanced electric field in devices with thin absorbers would assist the tunneling mechanism responsible for the transition in the reverse curve. Therefore, thinning the absorber would alter the reverse characteristic to have an earlier transition, limiting the voltage and preventing damage by reverse bias. Their study showed no correlation between transition and layer thickness. However, they have found an apparent correlation between damage voltage in the dark and absorber layer thickness. In this respect, the results of Mansfield *et al.* are in agreement with the results presented in this study, even though Mansfield *et al.* described “the trend to be not perfect”. In this study, a large number of devices were measured, in order to obtain more confidence in the results. It is likely that the enhanced electric field in thinner absorbers is at least partly responsible for the increased sensitivity to reverse bias damage.

Besides the electric field, other factors, mostly related to device characteristics, change as well when making the absorber thinner. A major factor is the reduced absorption in thinner absorbers, which is responsible for the reduced  $J_{sc}$  observed for thinner cells. However, this is not expected to directly influence the damage voltage in darkness. Changes in device quality, due for example to enhanced recombination at the back contact, often result in reduced  $V_{oc}$  and FF. The product of the  $V_{oc}$  and FF is therefore a good metric to assess the quality of the device. Figure 6-6 shows the  $V_{oc} \times FF$  value for all the cells that were damaged during dark reverse bias sweeps. This figure shows a very large spread as well as a large number of cells with a low  $V_{oc} \times FF$  value in group I. The lower efficiency of the group I cells was the initial motivation to add group II, with higher efficiency cells and thin absorbers, to this study. As can be observed in Figure 6-6 the  $V_{oc} \times FF$  value for group II are in the same range as group III (cells with thicker absorbers). From the difference between group I and II in terms of  $V_{oc} \times FF$  values and damage voltage in the dark, it can be concluded that the device quality could be a factor contributing to the damage voltage. However, group II and III show different damage voltage but similar  $V_{oc} \times FF$ , which suggests that the absorber layer thickness is probably the dominant factor for the damage voltage in the dark.

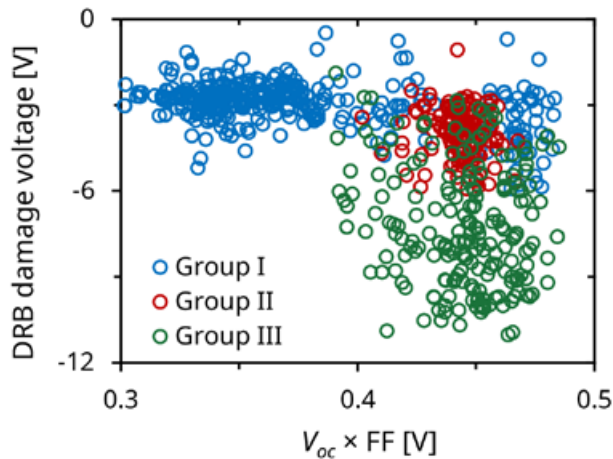


**Figure 6-6:** Plot of all cells of groups I, II and III, that were damaged during a dark reverse bias sweep. On the x-axis the  $V_{oc} \times FF$  value, and on the y-axis the damage voltage in the dark is plotted.

Another factor is the structural quality of the device itself. It is known that wormlike defects often originate at local weak spots, such as small pits, craters and cracks [35,51]. It could be expected that during the growth of the absorber layer the material quality improves. Therefore, more of these defects could be expected in thinner cells. However, 84 % (683 from the 812) of the wormlike defects found in the group I cells originated at the mechanically defined border. This indicates that, although wormlike defects do originate from local weak spots, these weak spots are likely mechanically induced rather than the result of imperfect absorber growth.

## 6.5 Conclusions

A large number of CIGS solar cells were exposed to reverse bias conditions in darkness or under illumination. It was demonstrated that the absorber layer thickness has a large influence on the voltage at which reverse bias induced defects are formed in CIGS cells and irreversibly damage the cells. Under illumination the damage ratio is influenced by the absorber thickness, where cells with thinner absorber layers are more prone to damage. In the dark the absorber thickness has a relation to the voltage at which wormlike defects are formed, thicker cells get damaged at higher absolute voltages. From the measurements in the dark the probability of the formation of wormlike defects at any reverse bias voltage could be estimated using simple statistics. It was shown that the damage probability for illuminated reverse bias estimated using the normal distribution of the measurements in the dark was in good agreement with the actual measured values.

The results of this chapter show that a voltage is required to form wormlike defects. The magnitude of the voltage required to form wormlike defects depends on the quality and thickness of the absorber layer.





## CHAPTER

# Determining the decomposition voltage of $\text{Cu}(\text{In}_{1-x}\text{Ga}_x)\text{Se}_2$

This chapter is based on the following publication:

K. Bakker, J. C. Matas, J. Bosman, N. Barreau, A. Weeber, and M. Theelen, "Determining the decomposition voltage of  $\text{Cu}(\text{In}_{1-x}\text{Ga}_x)\text{Se}_2$ ," in *2022 IEEE 49<sup>th</sup> Photovoltaics Specialists Conference (PVSC)*, Jun. 2022, pp. 0381–0383, doi: 10.1109/PVSC48317.2022.9938940.

## Chapter 7

# Determining the decomposition voltage of $\text{Cu}(\text{In}_{1-x}\text{Ga}_x)\text{Se}_2$

**ABSTRACT:** Partial shading of CIGS modules can lead to permanent damage of the module in the shaded area. This is caused by harmful reverse bias voltages in the shaded area which lead to reverse bias induced defects, also known as wormlike defects. A lot is already known about the origin and propagation of wormlike defects. However, the fundamental question: “why is CIGS so sensitive to reverse bias damage?” has not yet been answered. In this study we show that CIGS semiconductor material in the presence of an electric field will spontaneously decompose.

### 7.1 Introduction

Partial shading of CIGS modules can lead to permanent damage in the shaded area. The literature review of Chapter 3 showed that permanent damage was found in CIGS modules for all studies that performed electroluminescence (EL) measurements after the execution of shading tests. In EL images, these defects appear as shunts. Closer visual inspection learns that the defects have a very distinct appearance and are therefore often called wormlike defects. Wormlike defects are caused by a large negative voltage (reverse bias) and are trails of damaged material left behind by a propagating hotspot. They act as local shunts that permanently decrease module performance.

Research to the origin of these defects, Chapter 4 and Chapter 5, showed that a chemical reaction is responsible for a change in composition, and that the reaction propagates to a new spot when the material is consumed. In Chapter 5 it was observed that the TCO conductivity influences the propagation patterns and it was concluded that the electric field over the absorber layer has an important contribution in the formation and

propagation of wormlike defects. Further evidence for the influence of the electric field can be found in Chapter 6 that describes a study between the relation of absorber thickness and reverse bias voltage required to start wormlike defects. In this study it was shown that thinner cells have a much lower voltage threshold to form wormlike defects.

The observed dependency on the electric field made us hypothesize that the chalcogenide CIGS structure decomposes under influence of a large electric field to the copper-poor ordered vacancy compound (OVC) and copper selenide. The reaction would be  $\text{Cu}(\text{In}_{1-x}\text{Ga}_x)\text{Se}_2$  decomposes in  $\text{Cu}(\text{In}_{1-x}\text{Ga}_x)_3\text{Se}_5 + \text{Cu}_2\text{Se}$  or  $\text{Cu}(\text{In}_{1-x}\text{Ga}_x)_5\text{Se}_8 + 2\text{Cu}_2\text{Se}$ . This hypothesis is further supported by the fact that several studies on the compositional changes in wormlike defects observed Cu rich islands in the damaged material [33,51].

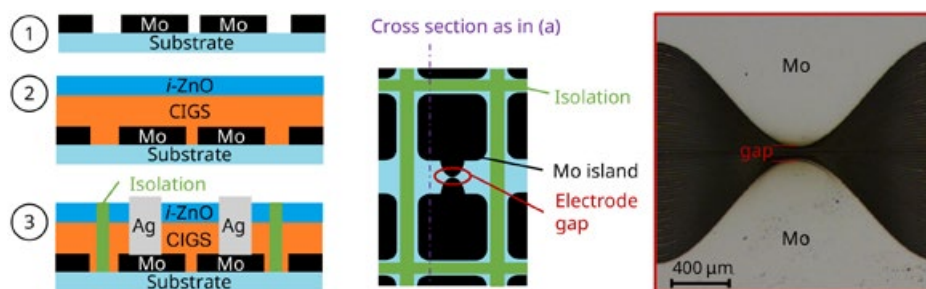
The conditions of the initial reaction that forms wormlike defects in CIGS solar cells is complicated to detect. In this study the decomposition of CIGS semiconductor material used in solar cells under the influence of an electric field is determined, using a dedicated sample configuration. With this sample configuration the conductivity of the CIGS material can be measured using a simple one-dimensional approach. By varying the electric field changes in conductivity can be detected and linked to changes in the CIGS material. To the best of our knowledge this is the first time that it is shown that CIGS decomposes when a large electric field is applied. This is an important step towards understanding the complex mechanism behind the formation of wormlike defects.

## 7.2 Experimental

A dedicated sample configuration was developed to measure the conductivity of CIGS semiconductor material with different compositions. Figure 7-1 shows a schematic representation of the sample layout as well as a microscope picture of the molybdenum electrodes. The process steps shown in Figure 7-1(a) are:

- 1) Deposition and laser structuring of the 400 nm Mo layer.
- 2) Coevaporation of 2  $\mu\text{m}$  3-stage CIGS and sputtering of a 150 nm *i*-ZnO capping layer.
- 3) Isolating of CIGS and opening the contacts by manually removing CIGS with a scalpel. Contacting with silver paint.

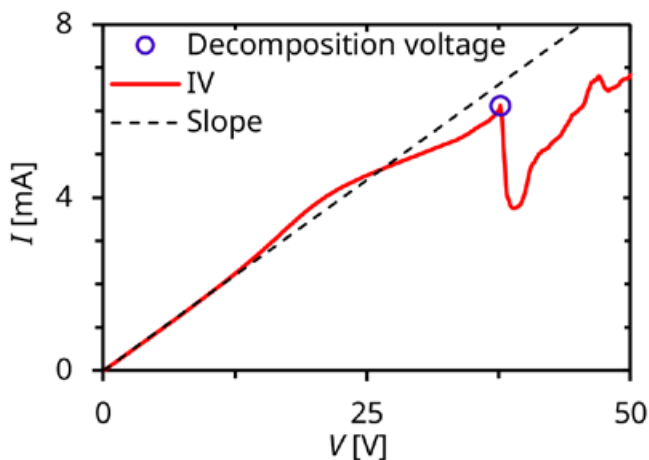
The  $i\text{-ZnO}$  capping layer is added to protect the CIGS and does not play a role in the electrical characterization. The laser pattern is designed to leave a gap between rounded electrodes, that has a defined distance. Two different laser patterns were used with a gap between electrodes of 32 or 86  $\mu\text{m}$ . Electrical characterization was performed by an  $IV$  sweep from 0 to 50 V in the dark with a Keithley 2400 source measure unit controlled by Rera tracer III software. After contacting, the sample was kept in the dark for a minimum of 60 seconds before performing the  $IV$  sweep.



**Figure 7-1:** Schematic and microscope photo of sample layout. In **(a)** a schematic cross section is given with from top to bottom the process steps 1 to 3. A schematic top view is drawn in **(b)** to indicate the approximate shape of the Mo islands after step 1 and the position of the isolation scribes after step 3. **(c)** Shows a microscope image of the electrode gap after laser scribing (step 1).

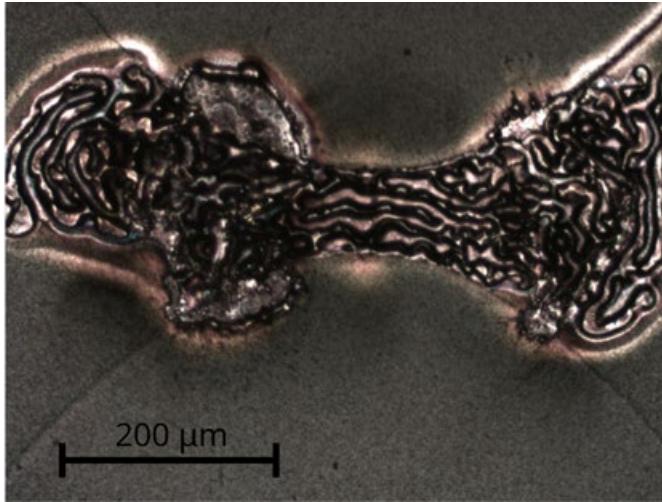
### 7.3 Result and discussion

Figure 7-2 shows a typical  $IV$  curve of an electrode pair with a gap of 86  $\mu\text{m}$ . At low voltages the  $IV$  curve follows a straight line, showing Ohmic behavior. At higher voltages the behavior deviates from the straight line, followed by a sharp change in current. This change in current could be both positive or negative and indicates a change in material properties. Therefore, we propose the term decomposition voltage for this point on the  $IV$  curve, because after this point visual compositional changes appear similar to wormlike defects.



**Figure 7-2:** *IV* curve of sample with a 86  $\mu\text{m}$  electrode gap. The measured *IV* curve is plotted as a red solid line. The black dotted line is an extrapolation of the average slope between 0 and 10 V to indicate ohmic behavior. The decomposition voltage is indicated with a purple circle.

The sharp change in current observed during the *IV* sweeps is very similar to the increase in current during the formation of wormlike defects as described in Chapter 6. The visual appearance after decomposition is also very similar to the visual appearance of wormlike defects. A microscope picture of a sample after an *IV* sweep can be found in Figure 7-3. The composition of the defects has not been studied in detail yet. However, initial microscopy and Raman measurements showed similarities with wormlike defects, created by reverse bias in CIGS solar cells. Just like in studies of wormlike defects no traces of OVC or  $\text{Cu}_2\text{Se}$  were found. The reaction is so aggressive that it is likely that the initial reaction products ( $\text{OVC} + \text{Cu}_2\text{Se}$ ) are consumed in a sequential reaction that gives the wormlike defects its distinct appearance.



**Figure 7-3:** Microscope picture of decomposed CIGS between two electrodes with a gap of  $86\ \mu\text{m}$ .

Because of the 1D approach the measurements are very reproducible. A large number of samples with CGI (copper/(gallium + indium)) varying from 0.795 to 0.894 was examined. All measurements showed the same behavior, as can be seen in Figure 7-4 where all measurements with a  $32\ \mu\text{m}$  electrode gap are plotted up to the decomposition voltage. The different shades of blue represent the copper content. From Figure 7-4 it can be seen that both slope and decomposition voltage depend on the CGI. Therefore, the dependency of the normalized resistance and normalized decomposition voltage on the CGI is given in Figure 7-5. The normalized resistance has a logarithmic dependency on CGI. The normalized decomposition voltage, or electric field, is depending linearly on the CGI, with the larger gap being less sensitive to the difference in copper concentration. This might be a geometric effect caused by the shape of the electrodes. The distance used for the normalization is the minimum distance between the electrodes. In reality, current will not flow in a straight line and will be distributed over a 3 dimensional area. Therefore, the geometry of the electrodes might influence the effective distance and thus introduce different errors in the determination of the electric field for the two gaps between the electrodes. The exact relationship between absorber layer quality and decomposition voltages is still unclear.



However, the conductivity is depending on carrier density and mobility so it is not unlikely that the semiconductor parameters have a large influence on the decomposition properties.

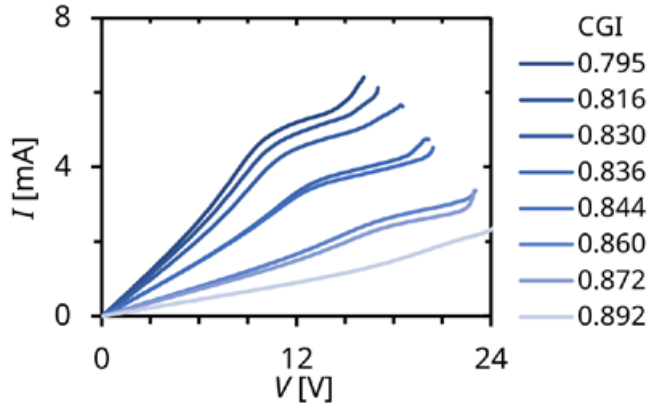


**Figure 7-4:** *IV* curves of all samples with a 32  $\mu\text{m}$  electrode gap up to the decomposition voltage. The CGI of each sample is plotted in different shades of blue, with the darkest color being the lowest CGI.

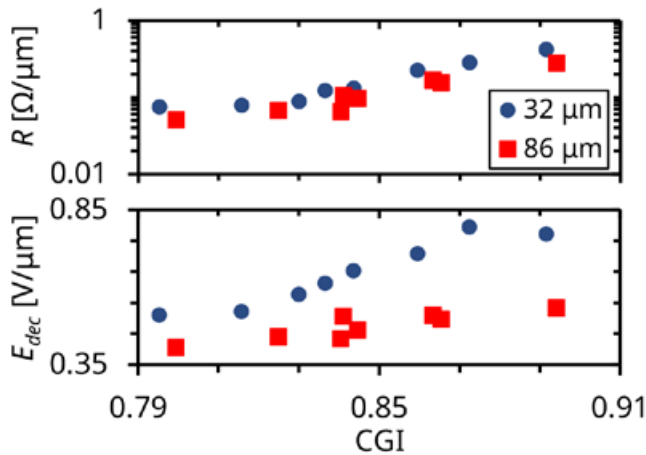


**Figure 7-5:** Resistance and decomposition voltage normalized to electrode distance plotted against CGI for two different electrode gaps. In all graphs the 32 and 86  $\mu\text{m}$  gaps are represented by dark blue circles and red squares, respectively.

## 7.4 Summary

The formation of wormlike defects during reverse bias is a major reliability concern for CIGS solar cells and modules. One of the unknown parameters required to predict the formation and propagation of wormlike defects is the sensitivity of the CIGS absorber material towards an electric field. This is difficult to determine in the traditional rather complicated CIGS solar cell stack. Therefore, a dedicated device structure was developed to measure the influence of an electric field on the CIGS absorber material used in solar cell. *IV* measurements on these structures showed that CIGS material is spontaneously decomposing. We proposed the term decomposition voltage for the electrical voltage required for decomposition. The decomposition voltage was found to be depending on CGI. The approach used in this study changed the puzzle of decomposition of CIGS from the complicated solar cell stack to a simple one-dimensional approach and proved that CIGS is unstable in the presence of a large electric field. Therefore, CIGS solar cells need to be protected against the harmful effects of reverse bias.

The results of this chapter show that the main mechanism behind the formation of wormlike defects in CIGS solar cell is the decomposition of the CIGS absorber material under the influence of an electric field in copper-poor ordered vacancy compounds and copper selenide.



**CHAPTER**

# Fundamental mechanisms behind the reverse characteristic of $\text{Cu(In,Ga)Se}_2$ solar cells

This chapter is based on the following publication:

K. Bakker, S. Assen, A. Rasia, N. Barreau, A. Weeber, and M. Theelen, "Fundamental Mechanisms Behind the Reverse Characteristic of Cu(In,Ga)Se<sub>2</sub> Solar Cells," *IEEE J. Photovoltaics*, pp. 1–6, 2022, doi: 10.1109/JPHOTOV.2022.3196827.

## Chapter 8

# Fundamental mechanisms behind the reverse characteristic of Cu(In,Ga)Se<sub>2</sub> solar cells

## GRAPHICAL ABSTRACT:

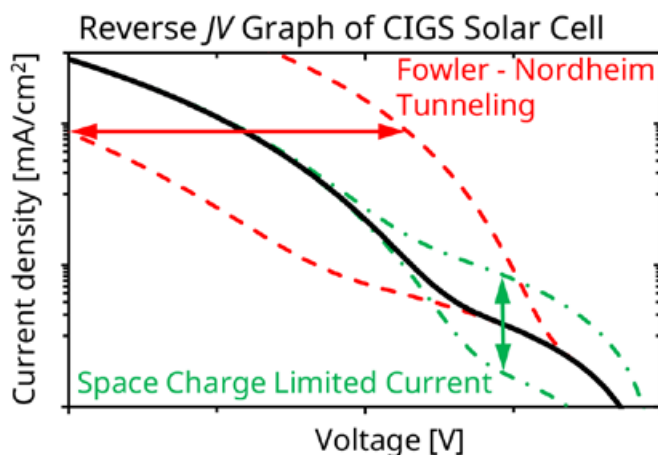


**Figure 8-1:** Graphical abstract as published with the online version of ref. [60].

**ABSTRACT:** Partial shading of PV modules can lead to degradation of the shaded cells. The degradation originates from a reverse bias voltage over the shaded cells. In order to mitigate reverse bias damage in Cu(In,Ga)Se<sub>2</sub> (CIGS) modules, a good understanding of the fundamental mechanisms governing the reverse characteristic is required. In this study, a model is introduced that describes this behavior for CIGS cells. In this model, the low and non-Ohmic leakage current is accounted for by the space charge limited current component. A sharp increase in current that is typically

observed in the CIGS reverse characteristics can be described by Fowler-Nordheim tunneling. This model was validated against measurements performed at different temperatures and illumination intensities, and is able to describe the dependencies of the reverse bias behavior on both temperature and illumination.

## 8.1 Introduction

Solar cells in partially shaded PV modules can be subjected to reverse bias voltages. In Cu(In,Ga)Se<sub>2</sub> (CIGS) solar cells, reverse bias voltages can lead to reversed bias induced defects, also known as wormlike defects [Chapter 3]. Exposure to reverse bias can in general be mitigated by the inclusion of bypass diodes. However, most commercial CIGS modules are of the monolithic interconnected type where it is difficult to integrate bypass diodes to protect individual cells due to the layout of the module [29,61]. Therefore, several authors have suggested to use the CIGS solar cell itself as a bypass diode [28,43], [Chapter 6]. This would be possible because the current density versus voltage ( $J/V$ ) characteristic at negative voltages shows an increase in current, such as a Zener or avalanche diode. This sharp increase resembles a transition between an insulating and conducting nature. The voltage at which this transition occurs, the transition voltage, strongly depends on illumination conditions [Chapter 6], [20,22,27,30,40]. This is partly due to the increased photoconductivity in the buffer layer as the color of illumination is an important parameter [27,30,40]. Low wavelength (blue) light, which is absorbed in the buffer layer, shifts the transition voltage to less negative voltages. This in contrast to high-wavelength (red) light, for which the buffer is transparent. Cells illuminated with red light show similar behavior in a reverse bias scan as cells in the dark. Other parameters shown to have a large influence on the reverse characteristic are temperature [30,40], buffer layer properties [30,39,41], and sodium concentration [40,42].

Discussion exists in literature on the mechanism behind the transition. In the earlier publications [30,40], the mechanism behind the transition in the dark is described to be the result of impact ionization (avalanche effect), tunneling (Zener effect), or a combination of avalanche and tunneling that may be assisted by defects or metastable interface charges [27]. Understanding the mechanisms and transferring them into a model is

essential for predicting the behavior of PV modules under partially shaded conditions [22,23], and in the end mitigate the impact.

The first model that was able to simulate the reverse characteristic was introduced by Sun *et al.* [20]. This model was used to simulate the electrothermal behavior of monolithically interconnected CIGS modules under partial shading [20,22]. This model explained the reverse characteristic by using tunneling through defects [Poole–Frenkel (PF) mechanism] and was also able to explain the light dependency by introducing a preexponential factor. Szaniawski *et al.* [41] introduced a model based on fitting of the reverse characteristic of several CIGS cells. The model of Szaniawski *et al.* [41] uses a combination of the PF mechanism and the Fowler–Nordheim (FN) mechanism. The FN mechanism describes tunneling through a triangular energy barrier, which Szaniawski *et al.* [41] assumed to be the buffer layer. In this model, FN tunneling is the dominant mechanism and the PF mechanism is used to explain the discrepancy at lower currents. However, this model is not able to explain the light dependency of the reverse characteristic. In the study presented in this Chapter, the reverse characteristic at different temperatures and illumination conditions was measured. Based on these measurements, we propose a model that explains both the temperature and illumination dependence of the reverse characteristic of CIGS cells.

## 8.2 Experimental

The single cell, described in this study, survived all measurement sequences, and has been used in previous studies Chapter 4 and Sample I-2 in Chapter 5. The measurement sequence for this cell was given as follows:

- 1) initial *JV* scan, 20 months after fabrication;
- 2) variable irradiance measurements (VIR), 12 days after initial *JV*;
- 3) dark temperature scan, 158 days after initial *JV* scan;
- 4) illuminated temperature scan, 168 days after initial *JV*.

The cell was stored in an inert environment in between measurements. The design of this cell resembles a cell in a monolithically interconnected module and, therefore, has no grid. To reduce series resistance losses, a thicker transparent conductive oxide is used, which makes the cell more robust against reverse bias damage [39]. The downside of this design is that



the efficiency is slightly lower. The layer stack is made out of: 1 mm soda-lime glass, 500 nm DC-sputtered molybdenum (Mo), 2  $\mu\text{m}$  coevaporated CIGS, 50 nm chemical bath deposited cadmium sulfide (CdS), 65 nm DC-sputtered intrinsic zinc oxide (*i*-ZnO), 1  $\mu\text{m}$  DC-sputtered aluminum doped zinc oxide (AZO), and 60 nm thermally evaporated gold (Au) contacts to the sides [Chapter 5].

An initial reverse *JV* scan was performed in a dark enclosure using a Keithley 2400, ranging from +0.7 to -10.0 V with the compliance set to 100 mA (294 mA/cm<sup>2</sup>) and a scan speed of 100 mV/s. The *JV* measurements for VIR and temperature scans were carried out with a Neonsee class AAA AM1.5G solar simulator type IV-SS-30V. The wide range irradiance control option of this simulator allows for attenuation of the irradiance while maintaining AM1.5G spectrum and was used to control the irradiance for both VIR and temperature scans. For the temperature scans, the sample was mounted in a Linkam THMS600 stage. Scan settings for VIR: from +0.7 to -9.3 V, compliance of 50 mA (147 mA/cm<sup>2</sup>), and a scan speed of 147 mV/s. The *JV* sweeps for the temperature scans were performed with a scan speed of 273 mV/s from +0.7 to -6 V and a current limit of 17.5 (51.5 mA/cm<sup>2</sup>) and 25 mA (73.5 mA/cm<sup>2</sup>) for the dark and illuminated measurements, respectively.

## 8.3 Results and discussion

### 8.3.1 Components of the model

Szaniawski *et al.* [41] proposed a model based on the work of Sun *et al.* [20] in which the FN mechanism is responsible for the large increase in current after the transition. Furthermore, they also observed an increase in current already before the transition. Szaniawski *et al.* [41] explained this by the PF model, where Sun *et al.* [20] used the space charge limited current (SCLC) [62,63] to explain this non-Ohmic current.

**Table 8-1:** Constants and variables used in simulations

Parameter	Definition	Value and Unit
$C_{FN}$	Correction factor for Fowler-Nordheim	...
$q$	Elementary charge	$1.602 \times 10^{-19}$ C
$E$	Electric field	V/m
$m^*$	Effective mass of electron in CIGS	$9.109 \times 10^{-32}$ kg
$m_e$	Mass of electron	$9.109 \times 10^{-31}$ kg
$\Phi_{FN}$	Fowler-Nordheim barrier	eV
$h$	Planck constant	$6.626 \times 10^{-34}$ Js
$\mu$	Electron mobility	$1 \times 10^{-2}$ m <sup>2</sup> /(Vs)
$N_C$	Density of states in the conduction band	$2 \times 10^{24}$ m <sup>-3</sup>
$\Phi_{PF}$	Poole-Frenkel barrier	V
$\epsilon_i$	Dielectric constant of CIGS	13
$\epsilon_0$	Permittivity of free space	$8.854 \times 10^{-12}$ F/m
$k_B$	Boltzmann constant	$1.381 \times 10^{-23}$ J/K
$T$	Temperature	K
$k$	Coefficient of SCLC component	A/V <sup>m</sup>
$m$	SCLC power factor	...
$V^*$	Voltage after series resistance losses	V
$d$	Thickness of buffer layer	m
$V$	Applied voltage	V
$J$	Current density through cell	A/m <sup>2</sup>
$J_{FN}$	Fowler-Nordheim current density	A/m <sup>2</sup>
$J_{PF}$	Poole-Frenkel current density	A/m <sup>2</sup>
$J_{SCLC}$	Space charge limited current density	A/m <sup>2</sup>
$J_{shunt}$	Shunt resistance current density	A/m <sup>2</sup>
$R_s$	Series resistance	$\Omega m^2$
$R_{shunt}$	Shunt resistance	$\Omega m^2$

The model used in this study is using the FN mechanism as the dominant mechanism. Furthermore, the PF and SCLC mechanisms are used to explain the non-Ohmic behavior before the transition that cannot be explained by the FN mechanism. The equations for the current density as a results of the FN ( $J_{FN}$ ) and PF ( $J_{PF}$ ) mechanisms are based on Szaniawski *et al.* [41] and are given as follows:

$$J_{FN} = C_{FN} \frac{q^3 E^2}{8\pi\Phi_{FN}} \frac{m^*}{m_e} \exp \left[ -\frac{8\pi\sqrt{2m^*}\Phi_{FN}^3}{3qhE} \right] \quad (8-1)$$

$$J_{PF} = q\mu N_c E \exp \left[ -\frac{q(\Phi_{PF} - \sqrt{\frac{qE}{\pi\epsilon_i\epsilon_0}})}{k_B T} \right] \quad (8-2)$$

A list of all constants and variables used can be found in Table 8-1. In (8-1) and (8-2),  $E$  is the electric field over the buffer layer, as described by Szaniawski *et al.* [41], which is given as follows:

$$E = \frac{V^*}{d} \quad (8-3)$$

Both mechanisms describe electron transport through the buffer layer in the presence of an electric field.

The FN equation (8-1) describes tunneling through a triangular barrier, and the only material-related parameter in this equation is the effective mass of the electron. The rest of the parameters are all physical constants. In order to incorporate changes in the device due to dependencies of light and temperature a preexponential factor  $C_{FN}$  was introduced.

The PF formula (8-2) describes trap-assisted electron transport, from the formula it can be seen that it depends on material parameters and temperature. The material parameters being conduction ( $q\mu N_c$ ) and the dielectric constant ( $\epsilon_i$ ). For this study, the conductivity was kept constant, and no preexponential factor was used. This would not directly change the outcome of the fit but would have an impact on the voltage barrier  $\Phi_{PF}$ , according to the rules for exponents ( $\exp^a \times \exp^b$ ) =  $\exp^{(a+b)}$ .

For all fittings, the CIGS material parameters from Szaniawski *et al.* [41] have been taken over. Since  $E$  is assumed to be the field over the buffer layer, it could be argued that material parameters for CdS would be more

appropriate. However, we found a constant difference in FN parameters ( $35.8 \pm 0.4$  % for  $\Phi_{FN}$  and  $-45.4 \pm 1.5$  % for  $C_{FN}$ ) when CdS parameters were used. Furthermore, the chi-square, used to determine the goodness of the fit, remained unchanged, and trends remain the same. Because of the constant difference, we can conclude that FN tunneling is the main mechanism responsible for the reverse bias behavior. The exact nature of the tunneling barrier will be determined by material properties of the complex stack between the AZO and the quasi-neutral bulk CIGS material. Therefore, the exact parameters are difficult to determine, and need further investigation.

For all equations,  $V^*$  is the voltage minus the series resistance losses and is given as follows:

$$V^* = |V| - (|J|R_s) \quad (8-4)$$

Note that for the fitting, the absolute values of voltage and current density were used.

Equations (8-5) and (8-6) give the current densities as results of the SCLC ( $J_{SCLC}$ ) and shunt resistance ( $J_{shunt}$ ), respectively, as follows:

$$J_{SCLC} = k(V^*)^m \quad (8-5)$$

$$J_{shunt} = \frac{V^*}{R_{shunt}} \quad (8-6)$$

The total current density through the cell at reverse bias is the sum of the contributions and given in (8-7), where  $J_{photo}$  is the light generated current.

$$J = -(J_{photo} + J_{FN} + J_{PF} + J_{SCLC} + J_{shunt}) \quad (8-7)$$

Each of the individual contributions can be omitted, or set to zero; for example,  $J_{photo}$  is zero for dark measurements and is used as a free fitting parameter for the illuminated measurements.

### 8.3.2 Pretransition mechanism

The pretransition mechanism is the mechanism responsible for the small non-Ohmic leakage current observed at low absolute voltages. Figure 8-2 shows the measurements and fits to different combinations of components for a dark reverse characteristic at 267 K. Cooling the cell attenuates the mechanism responsible for the transition [30,40]. Therefore, cooling allows for closer inspection of the small non-Ohmic leakage current. Figure 8-2(a) and (b) shows fits with  $J_{SCLC}$  set to zero in (8-7). As starting value for the fit 0.5 and 1.2 V were used for  $\Phi_{PF}$  for Figure 8-2(a) and (b), respectively. The results shown in Figure 8-2(a) and (b) show that the PF mechanism is not able to describe the small non-Ohmic prebreakdown current. The outcome is strongly depending on the starting conditions. Even when the FN contribution is fixed, the PF mechanism is at lower temperatures not able to describe the prebreakdown current accurately. Adding a preexponential correction factor, as described by Sun *et al.* [20] does not alter the shape of the curve. Furthermore, the numerical fitting procedure with a combination of PF and FN is not robust as the outcome strongly depends on the initial value of the parameters. In this case, the additional freedom of two variable parameters forces the FN contribution either to zero [see Figure 8-2(b)] or to contribute to the prebreakdown current [see Figure 8-2(a)]. Figure 8-2(c) shows the results for fits with a combination of  $J_{FN}$ ,  $J_{SCLC}$ , and  $J_{shunt}$ . As can be seen the SCLC fits the pretransition current almost perfectly. This implies that in the dark, the SCLC is the superior mechanism at all temperatures. In the next sections, all fits will be performed with a combination of  $J_{SCLC}$  and  $J_{shunt}$  for the pretransition current, and  $J_{FN}$  as the main transition current.

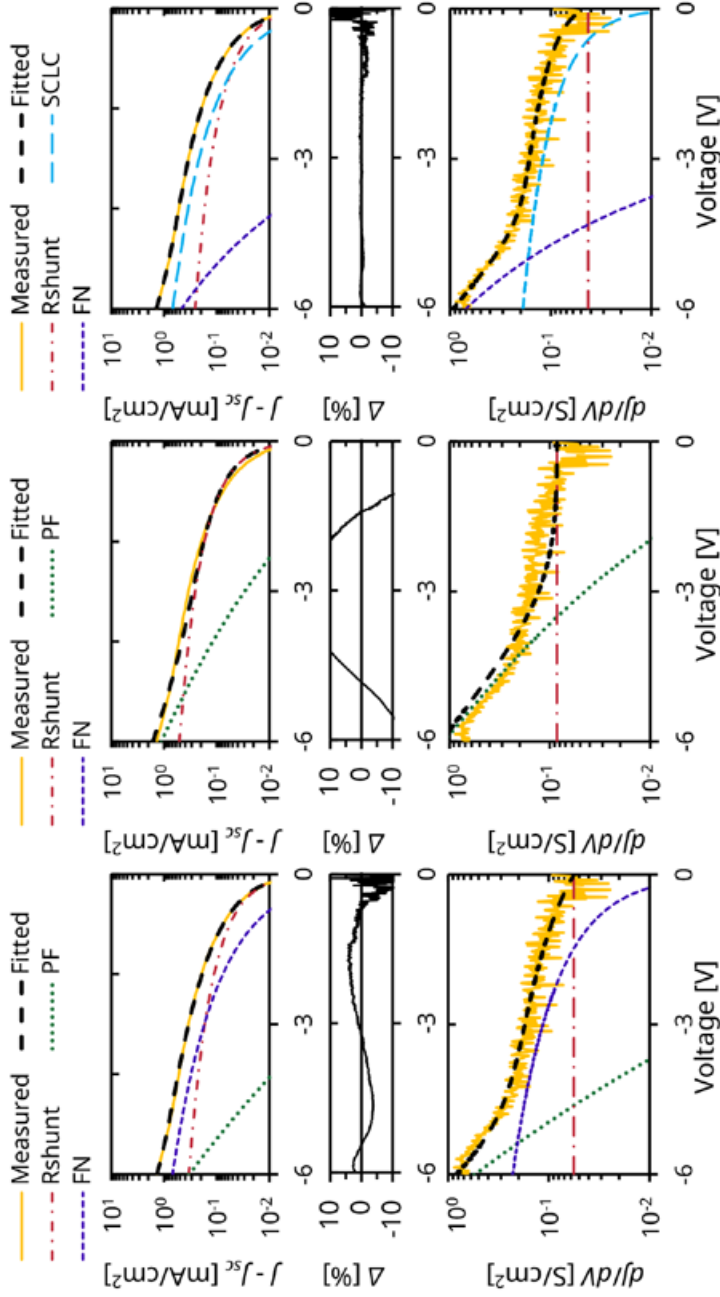


**Figure 8-2:** Dark reverse characteristic of one CIGS solar cell measured at 267 K. The same measurement is fitted with different prebreakdown mechanisms. In **(a)**, **(b)**, and **(c)**, the x-axis in all graphs is voltage, the top graph is the  $JV$  graph on a semilog scale, the middle graph is the difference ( $\Delta$ ) between measured and fitted data, and the bottom graph shows the derivative of the top graph. In **(a)** and **(b)**, a combination of  $J_{FN}$ ,  $J_{PF}$  and  $J_{shunt}$  was used. In **(a)**, the fitting routine was started with a low value for  $\Phi_{PF}$  (0.5 V), whereas in **(b)**, it was started with a high PF barrier (1.2 V). For **(c)**, the combination  $J_{FN}$ ,  $J_{SCLC}$  and  $J_{shunt}$  was used for the fitting.

### 8.3.3 High injection, parameter drift, and series resistance

In Figure 8-3, the results of two consecutive measurements are shown. The intention of these measurements was the creation of wormlike defects [Chapter 4 and Chapter 5], for which the sweep speed was set to a relatively slow 100 mV/s and the current limit was set to a very high 294 mA/cm<sup>2</sup>. Furthermore, the measurement was not aborted when the current limit was reached and the maximum current was injected into the cell till the end of the sweep. Two different features can be seen in Figure 8-3: first, the reduced voltage at high currents, and second, the non-reproducible behavior.

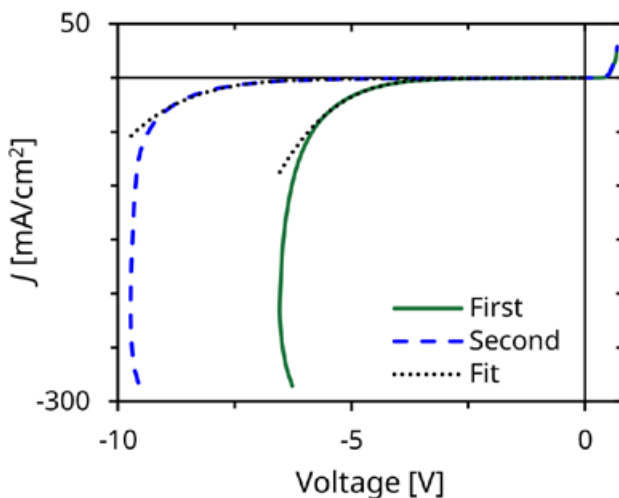


**Figure 8-3:** Dark  $JV$  characteristics of two consecutive measurements. The first measurement is displayed as a green solid line and the second as a blue dashed line. For both measurements the fit results are represented in black dotted lines.

At high current densities, the voltage over the cell is getting less negative, almost as if there was a negative series resistance. This behavior shows that the power dissipated by the cell during the measurement is causing the cell to heat up and alter the reverse characteristic during the measurement. For example, the power ( $V \times J$ ) dissipated at 50 mA/cm<sup>2</sup> is 312

and 470 mW/cm<sup>2</sup> for the first and second measurements, respectively. At higher temperatures, the transition shifts to less negative voltages. In the fitting, this behavior is taken into account by fitting  $J$ - $J_{sc}$  up to 50 mA/cm<sup>2</sup> and by setting the series resistance to 0  $\Omega \times \text{cm}^2$ .

Furthermore, there is a large discrepancy between the first and second measurement. Similar changes in the reverse characteristic caused by consecutive measurements have also been reported for CdS containing cells by Szaniawski *et al.* [41]. Also, it has been observed that temperature and light soaking have an influence on the reverse characteristic [27].

In forward bias changes in the  $JV$  curves as a result of illumination and temperature were observed [64]. These changes results in parameter drifts of mostly the open-circuit voltage ( $V_{oc}$ ) and fill factor, and are often called metastability. In order to avoid confusion, the term parameter drift is used in this study to describe the changes in reverse bias behavior. The principles behind the parameter drift are not yet understood and is something to keep in mind when studying the reverse characteristic.

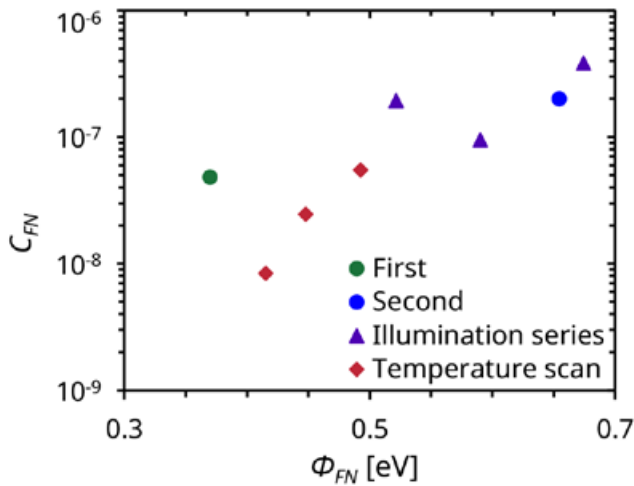


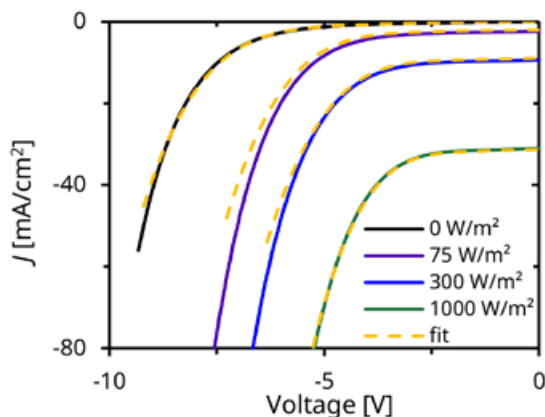
**Figure 8-4:** Fit results of comparable dark measurements, with on the x-axis the FN energy and on the y-axis the FN coefficient. The results of the initial measurements from Figure 8-3 are displayed in circles, the green and blue circles represent the first and second measurement, respectively. The results from the illumination series are displayed in purple triangles, and the results of the temperature scan are shown in red diamonds.



In order to reduce the exposure to high voltages and powers the current limit was lowered, the measurement were stopped when the current limit was reached, and faster scan speeds where used for the irradiance series and temperature scans. Figure 8-4 shows fitting results of the FN coefficient and FN energy for dark measurements at room temperature. It can be seen that there is a large difference between the first and second measurements of Figure 8-3 (see the blue and green circles in Figure 8-4) and that differences have been greatly reduced for the irradiance series and temperature scans.

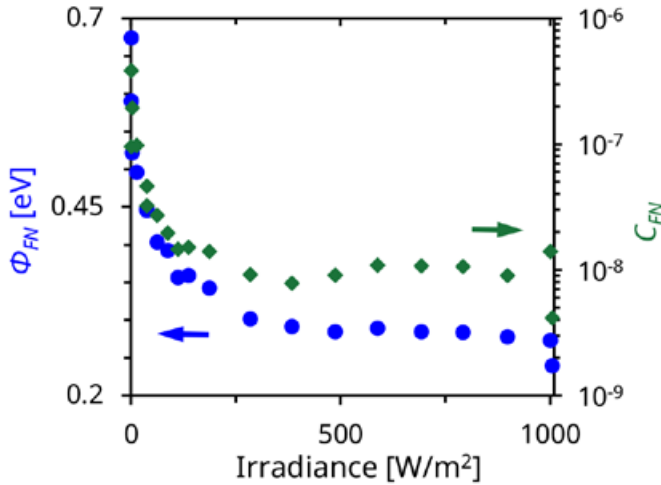
### 8.3.4 Irradiance dependence

Figure 8-5 shows the reverse  $JV$  curves of a number of irradiance dependent measurements from dark to 1 sun. It can be seen that the transition shifts to more negative voltages when the irradiance is decreased. This means that more energy is required in order for the solar cell to conduct the FN tunneling current. This can also be observed in the results of the fits using the SCLC and FN components, plotted in Figure 8-6. In Figure 8-6, a change in both FN-energy and correction factor is observed around 250 W/m<sup>2</sup>. This might be caused by a critical threshold for photoconduction in the buffer layer. This behavior is in line with Puttnins *et al.* [40], who found the threshold to be around 100 W/m<sup>2</sup>.



**Figure 8-5:** . Reverse  $JV$  curves at different illumination intensities. Solid curves represent the measured data and dashed curves show the fitted data.

With the addition of the FN correction factor this model is able to fit the light dependency of the reverse characteristic. When performing fitting to compare the different components the FN showed a better fit compared with the PF in almost all cases.



**Figure 8-6:** Fit results (SCLC and FN) of irradiance depended reverse  $JV$  characteristics. The blue circles represent the FN energy on the left y-axis, and the green diamonds show the FN coefficient on the right y-axis.

### 8.3.5 Temperature Dependence

Reducing the temperature will attenuate the FN tunneling current. The model is able to fit a very small FN contribution. However, fitting very low contributions is not very meaningful.

Therefore, the results of the dark measurements and results at temperatures below 250 K ( $0.004 \text{ K}^{-1}$ ) are not shown in Figure 8-7. Figure 8-7(a) shows the parameter drift at  $100 \text{ W/m}^2$ , probably as a result of light soaking and annealing. The results of the temperature scan at  $100 \text{ W/m}^2$  is very different compared with the scans at  $300$  and  $1000 \text{ W/m}^2$ , respectively. This might be partly explained by the fact that  $100 \text{ W/m}^2$  is in the very steep part of Figure 8-6 and partly because of conditioning of the cell. During the temperature scan, the cell is given time to reach a stable temperature before performing the  $JV$  scans. The first measurement is  $100 \text{ W/m}^2$  followed by  $300$  and  $1000 \text{ W/m}^2$ . In Figure 8-7(a) and (b), the

results of cooling below 323 K ( $0.0031 \text{ K}^{-1}$ ) have been omitted. At higher illumination intensities, the FN energy ( $\Phi_{FN}$ ) decreases linearly with temperature [see Figure 8-7(b)] and the FN coefficient ( $C_{FN}$ ) decreases logarithmical with temperature [see Figure 8-7(c)]. This logarithmic decrease has an Arrhenius like behavior and follows the general Arrhenius law, given as follows:

$$C = C_0 \exp \frac{-E_a}{k_B T} \quad (8-8)$$

In (8-8),  $C_0$  is a preexponential factor, and  $E_a$  is the activation energy. For this cell, the activation energy is approximately 0.491 eV, roughly twice the FN energy.

### 8.3.6 Wormlike Defects

The biggest challenge when studying the reverse characteristic is the formation of wormlike defects. When performing the temperature scan in the dark, even though very conservative voltage ranges were being used, several cells died. The observed temperature dependence could be partly responsible for the creation of wormlike defects. Due to local heating the reverse current will increase locally due to instantaneous heating, this increased current could lead to a critical local heating, sufficient to start the formation of wormlike defects as described in Chapter 4 and Chapter 5.

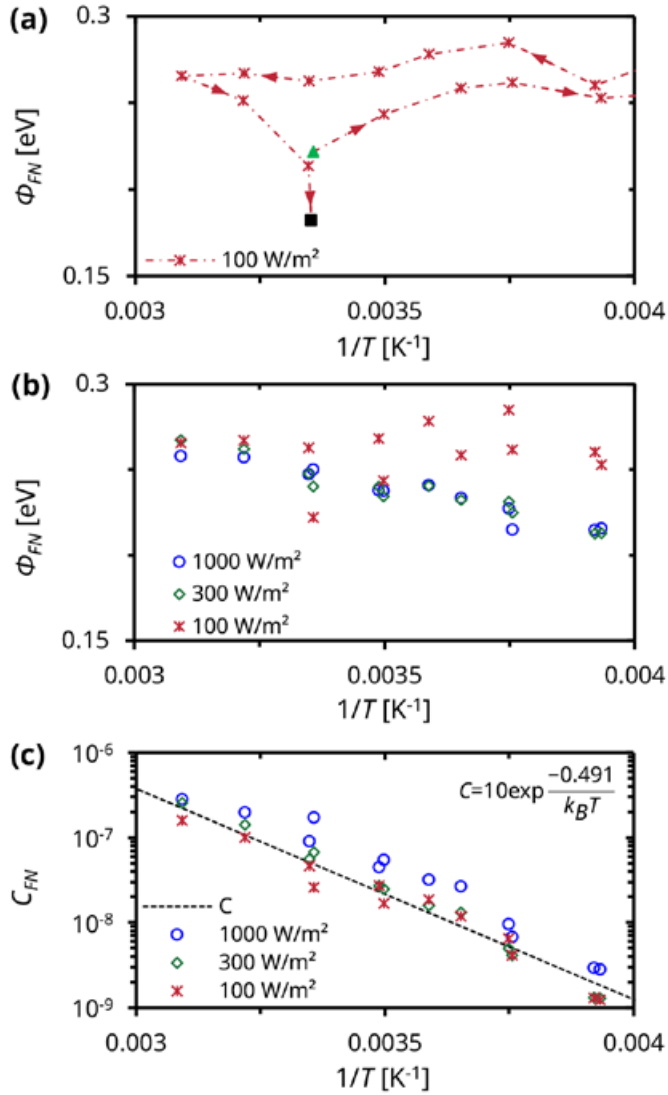


**Figure 8-7:** Fitting results of temperature scans. **(a)** shows the full hysteresis of the FN energy plotted against  $1/T$  at 100 W/m<sup>2</sup>. The measurement points are connected with a red dash dotted line with arrows indicating the scan direction. The first measurement point is indicated with a green triangle and the last measurement point is represented by a black square. In **(b)** and **(c)**, the  $\Phi_{FN}$  and  $C_{FN}$  are plotted against  $1/T$  for illumination intensities of 100 W/m<sup>2</sup> (red asterisks), 300 W/m<sup>2</sup> (green diamonds), and 1000 W/m<sup>2</sup> (blue circles). The black dashed line in **(c)** is the solution to the Arrhenius equation [see (8-8)] with an activation energy of 0.491 eV.

## 8.4 Conclusions

The reverse characteristic of CIGS cells is an important, but little studied, subject. In this Chapter, the question “what is the mechanism behind the sharp increase in current in the reverse  $J/V$  characteristic of CIGS solar cells?” is answered by introducing a model to describe the reverse characteristic. The model consists besides the shunt resistance of two components. The SCLC is responsible for a small non-Ohmic leakage current, and FN tunneling causes the sharp increase in current. In the model, the FN energy ( $\Phi_{FN}$ ) influences the transition voltage and the FN coefficient ( $C_{FN}$ ) changes the slope.

The model introduced in this Chapter is able to describe both temperature and illumination dependency of the reverse characteristic. This would enable more accurate thermoelectrical modeling of CIGS modules under partial shading conditions. Furthermore, it would allow for more accurate studies of the reverse characteristic, as this model would allow a better description of the curve.

CHAPTER 1
CHAPTER 2
CHAPTER 3
CHAPTER 4
CHAPTER 5
CHAPTER 6
CHAPTER 7
<b>CHAPTER 8</b>
CHAPTER 9



# 9

**CHAPTER**

---

## Conclusions and Outlook





# Chapter 9

## Conclusions and Outlook

### 9.1 Conclusions

The literature review presented at the start of this dissertation (Chapter 3) revealed that reverse bias induced defects can occur when monolithically interconnected modules are partly shaded. Due to their distinct appearance, these defects are often referred to as wormlike defects. Wormlike defects consist of trails of damaged material. The material inside the defects has become porous and expanded, and is protruding from the surface like a mountain range. The size of the trails can vary from less than 0.1 mm to a network of tens of centimeters, meandering and branching to cover several square centimeters of the affected CIGS cell. The trails consist of small local defects that act as shunts and permanently reduce the performance of CIGS modules. The effect of a small single defect on a large module is neglectable, however, the power output of a module can locally be severely impacted when there is a high concentration of wormlike defects. Although wormlike defects and reverse bias effects in CIGS solar cells and modules had been studied for years, little was known on the mechanisms behind wormlike defects and the reverse  $JV$  characteristic. Based on the literature review the research topics for this dissertation have been selected, and the main conclusions that can be drawn from this doctoral research are:

- Wormlike defects propagate over the surface of a CIGS solar cell as a moving hotspot. The hotspot is fueled with material from the neighboring area, and propagation occurs when the hotspot hops to a new location. In order to hop, the conditions at the new location need to be favorable, and include the material quality, temperature and electric field. (Chapter 4 and Chapter 5)
- Increasing the conductivity of the window layer reduces the electric field close to the hotspot and prevents propagation of the hotspot. However, this will not stop the formation of reverse bias induced (wormlike) defects, these defects expand rather than propagate. (Chapter 5)

- The formation of wormlike defects is a voltage driven process. The voltage required to form wormlike defects depends on the thickness and quality of the CIGS absorber layer. (Chapter 6)
- The mechanism behind wormlike defects is the decomposition of CIGS absorber material under influence of an electric field. The reaction inside the moving hotspot is very aggressive and starts with the decomposition of CIGS into copper-poor ordered vacancy complexes (OVC) and conductive  $\text{Cu}_2\text{Se}$ . (Chapter 7)
- The reverse  $J/V$  characteristic describes the electrical behavior of CIGS solar cells at negative voltages. It is characterized by a sharp rise in current, like the junction breakdown in an avalanche or Zener diode. The mechanism behind this sharp increase in current is best described by the Fowler–Nordheim mechanism. The Fowler–Nordheim mechanism is a specific tunneling mechanism, where the tunneling barrier is located in the complex stack between the AZO and the quasi-neutral bulk CIGS material. (Chapter 8)

## 9.2 Outlook

Wormlike defects can occur in CIGS modules in the field as a result of reverse bias during partial shading. These defects are caused by an unfortunate material property of the CIGS absorber, the CIGS material decomposes under the influence of an electric field. From the research presented in this dissertation no logical conclusion can be drawn to prevent wormlike defects other than avoiding exposure to reverse bias. Unfortunately, in the most commonly used module, the monolithically interconnected module, this is nearly impossible. However, the concept of monolithically interconnected modules is slowly being abandoned by the industry. It seems that the market is shifting towards concepts that use large flexible cells with bypass diodes, such as the products offered by companies Midsummer and MiaSolé. This concept is comparable to the mainstream rigid c-Si modules that dominate the market. The inclusion of bypass diodes limits the exposure to reverse bias, and thus the formation of wormlike defects. However, more research is needed in the field and in the lab to completely eliminate the formation of wormlike defects.

Another market driven change would be the introduction of tandem cells that have much higher power conversion efficiencies. The most logical

step for the first commercial flexible all thin-film tandem devices would be the combination of a CIGS bottom cell and a perovskite top cell. For this dissertation only CIGS material with a gallium content (GGI) between 0.2 and 0.4 was used, as this results in CIGS material with an optimal bandgap for single junction devices. However, tandem devices require a narrower bandgap for the bottom cell and therefore less gallium. I noticed during the PVSS summer school that the CIS device (Würth Solar 80W GeneCIS module) used for the practicum on partial shading did not develop wormlike defects despite the countless partial shading test it has been exposed to. After talking to an expert, I got to believe that there is no gallium in this module. Therefore, the impact of reverse bias might be different for tandem cells that use narrow bandgap CIGS with no (CIS) or almost no gallium. Another possible mitigating effect for tandems is that the current density is lower. The formation of wormlike defects is a voltage driven process, therefore they can still be created in tandem devices. Little is known about the effects of reverse bias on the perovskite top cell, this is a topic that has gained a lot of attention recently as this might be a potential showstopper for successful market introduction of the perovskite technology.

A large part of this doctoral research was spent in understanding the electrical behavior of the CIGS solar cell at negative voltages. This in order to find ways to manipulate the CIGS solar cell to avoid a high reverse voltage. Thus avoiding a high internal electric field over the CIGS absorber layer, and prevent the formation of wormlike defects. Manipulating the electrical behavior of CIGS solar cells requires a better understanding of the electrical conditions inside the CIGS solar cell at reverse bias. The electrical behavior of the CIGS solar cell at reverse bias is dominated by a tunneling process that occurs in a part of the layer stack close to the front electrode. Understanding the tunneling barrier's exact nature would require a combination of experiments and complex device simulations.

There are two options to reduce the internal electric field, either to avoid tunneling or to promote tunneling. The first option is to suppress the tunneling and restrict the current flow through the CIGS so no harmful field will form over the CIGS absorber. This will create the same electrical behavior as a normal diode that only allows current flow at positive voltages. The disadvantage of this option is that no energy can be harvested from a partially shaded PV device. The other option to limit the internal electric field is to reduce the tunnel barrier to have a large current

flow at small voltages. A good indication that this should be feasible, is the fact that in illuminated cells with thick absorbers the transition voltage is small and almost no defects are formed. An additional benefit of this approach would be that less power is dissipated, thus less heat generated in the shaded area.

In case the transition voltage can successfully be shifted to a small voltage in the dark, the negative temperature coefficient of the tunneling mechanism is a potential reliability risk. In case of local heating the heat will shift the transition voltage in such a way that the locally warmer region starts to conduct more current at the same voltage. This in turn will result in more heat generation, creating a loop that can result in unwanted thermal degradation.

Despite that the effect of reverse bias on CIGS cells and modules is a seemingly unsolvable problem I still foresee a bright future for the CIGS technology. Mostly because CIGS is currently the best commercial option for flexible solar cells, and a promising candidate for future flexible tandem devices with high efficiencies.

# References

- [1] "World has installed 1TW of solar capacity – pv magazine International", (n.d.). <https://www.pv-magazine.com/2022/03/15/humans-have-installed-1-terawatt-of-solarcapacity/>. (accessed July 20, 2022).
- [2] S. Philipps, W. Warmuth, "Photovoltaics report (updated 24 February 2022)", (2022). <https://www.ise.fraunhofer.de/en/publications/studies/photovoltaics-report.html>.
- [3] "Learning rates of global electricity supply technologies 2019 | Statista", (n.d.). <https://www.statista.com/statistics/457886/learning-rates-of-electricity-supplytechnologies/>. (accessed April 2, 2023).
- [4] F. Blake, K. Hanson, "The "hot spot" failure mode for solar arrays", in: *Proc. 4<sup>th</sup> Intersoc. Energy Convers. Eng. Conf.*, 1969: pp. 575–581.
- [5] First Solar, "Module Shading Guide", (2017) 8.
- [6] S. Minoura, T. Maekawa, K. Kodera, A. Nakane, S. Niki, H. Fujiwara, "Optical constants of Cu(In, Ga)Se<sub>2</sub> for arbitrary Cu and Ga compositions", *J. Appl. Phys.* 117 (2015) 195703. <https://doi.org/10.1063/1.4921300>.
- [7] W. Witte, R. Kniese, M. Powalla, "Raman investigations of Cu(In,Ga)Se<sub>2</sub> thin films with various copper contents", *Thin Solid Films.* 517 (2008) 867–869. <https://doi.org/10.1016/j.tsf.2008.07.011>.
- [8] S. Shirakata, K. Ohkubo, Y. Ishii, T. Nakada, "Effects of CdS buffer layers on photoluminescence properties of Cu(In,Ga)Se<sub>2</sub> solar cells", *Sol. Energy Mater. Sol. Cells.* 93 (2009) 988–992. <https://doi.org/10.1016/j.solmat.2008.11.043>.
- [9] K. Bakker, A. Weeber, M. Theelen, "Reliability implications of partial shading on CIGS photovoltaic devices: A literature review", *J. Mater. Res.* 34 (2019) 3977–3987. <https://doi.org/10.1557/jmr.2019.373>.
- [10] D.S. Philips, W. Warmuth, "Fraunhofer ISE: Photovoltaics Report, updated: 14 March 2019", 2019. <https://www.ise.fraunhofer.de/content/dam/ise/de/documents/publications/studies/Photovoltaics-Report.pdf>.
- [11] G. Birant, J. de Wild, M. Meuris, J. Poortmans, B. Vermang, "Dielectric-Based Rear Surface Passivation Approaches for Cu(In,Ga)Se<sub>2</sub> Solar Cells—A Review", *Appl. Sci.* 9 (2019) 677. <https://doi.org/10.3390/app9040677>.
- [12] M.A. Green, E.D. Dunlop, D.H. Levi, J. Hohl-Ebinger, M. Yoshita, A.W.Y. Ho-Baillie, "Solar cell efficiency tables (version 54)", *Prog. Photovoltaics Res. Appl.* 27 (2019) 565–575. <https://doi.org/10.1002/pip.3171>.
- [13] T. Feurer, P. Reinhard, E. Avancini, B. Bissig, J. Löckinger, P. Fuchs, R. Carron, T.P. Weiss, J. Perrenoud, S. Stutterheim, S. Buecheler, A.N. Tiwari, "Progress in thin film CIGS photovoltaics - Research and development, manufacturing, and applications", *Prog. Photovoltaics Res. Appl.* 25 (2017) 645–667. <https://doi.org/10.1002/pip.2811>.
- [14] K. Branker, M.J.M. Pathak, J.M. Pearce, "A review of solar photovoltaic levelized cost of electricity", *Renew. Sustain. Energy Rev.* 15 (2011) 4470–4482. <https://doi.org/10.1016/j.rser.2011.07.104>.

- [15] H. Ziar, B. Asaei, S. Farhangi, M. Korevaar, O. Isabella, M. Zeman, "Quantification of Shading Tolerability for Photovoltaic Modules", *IEEE J. Photovoltaics*. 7 (2017) 1390–1399. <https://doi.org/10.1109/JPHOTOV.2017.2711429>.
- [16] K. Brecl, M. Topič, "Self-shading losses of fixed free-standing PV arrays", *Renew. Energy*. 36 (2011) 3211–3216. <https://doi.org/10.1016/j.renene.2011.03.011>.
- [17] T.J. Silverman, M.G. Deceglie, C. Deline, S. Kurtz, "Partial shade stress test for thin-film photovoltaic modules", in: *SPIE Opt. + Photonics Sustain. Energy*, 2015: p. 95630F. <https://doi.org/10.1117/12.2188774>.
- [18] T.J. Silverman, I. Repins, "Partial Shade Endurance Testing for Monolithic Photovoltaic Modules", in: *2018 IEEE 7<sup>th</sup> World Conf. Photovolt. Energy Convers. (A Jt. Conf. 45<sup>th</sup> IEEE PVSC, 28<sup>th</sup> PVSEC 34<sup>th</sup> EU PVSEC)*, IEEE, 2018: pp. 3932–3937. <https://doi.org/10.1109/PVSC.2018.8547832>.
- [19] S. Wendlandt, L. Podlowski, "Influence of Near Field Shadowing on the Performance Ratio of Thin Film Modules", in: *35<sup>th</sup> Eur. Photovolt. Sol. Energy Conf. Exhib.*, 2018: pp. 1230–1235. <https://doi.org/10.4229/35thEUPVSEC20182018-5CV.1.35>.
- [20] X. Sun, J. Raguse, R. Garriss, C. Deline, T. Silverman, M.A. Alam, "A physics-based compact model for CIGS and CdTe solar cells: From voltage-dependent carrier collection to light-enhanced reverse breakdown", in: *2015 IEEE 42<sup>nd</sup> Photovolt. Spec. Conf.*, IEEE, 2015: pp. 1–6. <https://doi.org/10.1109/PVSC.2015.7355778>.
- [21] S. Dongaonkar, C. Deline, M.A. Alam, "Performance and Reliability Implications of Two-Dimensional Shading in Monolithic Thin-Film Photovoltaic Modules", *IEEE J. Photovoltaics*. 3 (2013) 1367–1375. <https://doi.org/10.1109/JPHOTOV.2013.2270349>.
- [22] T.J. Silverman, M.G. Deceglie, X. Sun, R.L. Garriss, M.A. Alam, C. Deline, S. Kurtz, "Thermal and Electrical Effects of Partial Shade in Monolithic Thin-Film Photovoltaic Modules", *IEEE J. Photovoltaics*. 5 (2015) 1742–1747. <https://doi.org/10.1109/JPHOTOV.2015.2478071>.
- [23] M.D. J. Carolus, Z. Purohit, T. Vandenbergh, M. Meuris, B. Tripathi, "Proposing an Electro-Thermal SPICE Model to Investigate the Effect of Partial Shading on CIGS PV Modules", in: *35<sup>th</sup> Eur. Photovolt. Sol. Energy Conf. Exhib.*, 2018: pp. 1343–1345. <https://doi.org/10.4229/35thEUPVSEC20182018-5CV.3.35>.
- [24] M. Gostein, L. Dunn, "Light soaking effects on photovoltaic modules: Overview and literature review", in: *2011 37<sup>th</sup> IEEE Photovolt. Spec. Conf.*, IEEE, 2011: pp. 003126–003131. <https://doi.org/10.1109/PVSC.2011.6186605>.
- [25] T.J. Silverman, R. Ingrid, "Shadows from People and Tools Can Cause Permanent Damage in Monolithic Thin-Film Photovoltaic Modules", in: *33<sup>rd</sup> Eur. Photovolt. Sol. Energy Conf. Exhib.*, 2017: pp. 1422–1426. <https://doi.org/10.4229/EUPVSEC20172017-5CO.6.6>.
- [26] C. Tzikas, G. Gomez, M. van den Donker, K. Bakker, A.H.M. Smets, W. Folkerts, "Do Thin Film PV Modules Offer an Advantage", in: *33<sup>rd</sup> Eur. Photovolt. Sol. Energy Conf. Exhib.*, 2017: pp. 1593–1596. <https://doi.org/10.4229/EUPVSEC20172017-5BV.4.21>.
- [27] P. Mack, T. Walter, R. Kniese, D. Hariskos, R. Schäffler, "Reverse Bias and Reverse Currents in CIGS Thin Film Solar Cells and Modules", in: *23<sup>rd</sup> Eur. Photovolt. Sol. Energy Conf. Exhib.*, 2008: pp. 2156–2159. <https://doi.org/10.4229/23rdEUPVSEC2008-3DO.5.3>.
- [28] T.J. Silverman, L. Mansfield, I. Repins, S. Kurtz, "Damage in Monolithic Thin-Film Photovoltaic Modules Due to Partial Shade", *IEEE J. Photovoltaics*. 6 (2016) 1333–1338. <https://doi.org/10.1109/JPHOTOV.2016.2591330>.

- 
- [29] J.E. Lee, S. Bae, W. Oh, H. Park, S.M. Kim, D. Lee, J. Nam, C. Bin Mo, D. Kim, J. Yang, Y. Kang, H. Lee, D. Kim, "Investigation of damage caused by partial shading of  $\text{CuIn}_x\text{Ga}_{(1-x)}\text{Se}_2$  photovoltaic modules with bypass diodes", *Prog. Photovoltaics Res. Appl.* 24 (2016) 1035–1043. <https://doi.org/10.1002/pip.2738>.
  - [30] P. Szaniawski, J. Lindahl, T. Törndahl, U. Zimmermann, M. Edoff, "Light-enhanced reverse breakdown in  $\text{Cu}(\text{In,Ga})\text{Se}_2$  solar cells", *Thin Solid Films*. 535 (2013) 326–330. <https://doi.org/10.1016/j.tsf.2012.09.022>.
  - [31] M. Nardone, S. Dahal, J.M. Waddle, "Shading-induced failure in thin-film photovoltaic modules: Electrothermal simulation with nonuniformities", *Sol. Energy*. 139 (2016) 381–388. <https://doi.org/10.1016/j.solener.2016.10.006>.
  - [32] E.E. van Dyk, C. Radue, A.R. Gxasheka, "Characterization of  $\text{Cu}(\text{In,Ga})\text{Se}_2$  photovoltaic modules", *Thin Solid Films*. 515 (2007) 6196–6199. <https://doi.org/10.1016/j.tsf.2006.12.065>.
  - [33] P.O. Westin, U. Zimmermann, L. Stolt, M. Edoff, "Reverse Bias Damage in CIGS Modules", in: *24<sup>th</sup> Eur. Photovolt. Sol. Energy Conf.*, 2009: pp. 2967–2970. <https://doi.org/10.4229/24thEUPVSEC2009-3BV.5.34>.
  - [34] S. Johnston, E. Palmiotti, A. Gerber, H. Guthrey, L. Mansfield, T.J. Silverman, M. Al-Jassim, A. Rockett, "Identifying Reverse-Bias Breakdown Sites in  $\text{CuIn}_x\text{Ga}_{(1-x)}\text{Se}_2$ ", in: *2017 IEEE 44<sup>th</sup> Photovolt. Spec. Conf.*, IEEE, 2017: pp. 1400–1404. <https://doi.org/10.1109/PVSC.2017.8366755>.
  - [35] E. Palmiotti, S. Johnston, A. Gerber, H. Guthrey, A. Rockett, L. Mansfield, T.J. Silverman, M. Al-Jassim, "Identification and analysis of partial shading breakdown sites in  $\text{CuIn}_x\text{Ga}_{(1-x)}\text{Se}_2$  modules", *Sol. Energy*. 161 (2018) 1–5. <https://doi.org/10.1016/j.solener.2017.12.019>.
  - [36] S. Johnston, D. Sulas, E. Palmiotti, A. Gerber, H. Guthrey, J. Liu, L. Mansfield, T.J. Silverman, A. Rockett, M. Al-Jassim, "Thin-Film Module Reverse-Bias Breakdown Sites Identified by Thermal Imaging", in: *2018 IEEE 7<sup>th</sup> World Conf. Photovolt. Energy Convers. (A Jt. Conf. 45<sup>th</sup> IEEE PVSC, 28<sup>th</sup> PVSEC 34<sup>th</sup> EU PVSEC)*, IEEE, 2018: pp. 1897–1901. <https://doi.org/10.1109/PVSC.2018.8547766>.
  - [37] M. Richter, J. Neerken, J. Parisi, "Reverse-Voltage Bias Induced Shunt Formation In  $\text{Cu}(\text{In,Ga})\text{Se}_2$  Thin Film Solar Cells an approach with three-dimensional electrothermal simulations", in: *32<sup>nd</sup> Eur. Photovolt. Sol. Energy Conf. Exhib.*, 2016: pp. 1116–1119. <https://doi.org/10.4229/EUPVSEC20162016-3CO.5.3>.
  - [38] J.P. M. Richter, M. Vrenegor, "Reverse-Breakdown Stability of  $\text{Cu}(\text{In,Ga})\text{Se}_2$  Thin-Film Solar Cells", in: *33<sup>rd</sup> Eur. Photovolt. Sol. Energy Conf. Exhib.*, 2017: pp. 1017–1019. <https://doi.org/10.4229/EUPVSEC20172017-3AO.8.5>.
  - [39] S. Puttnins, S. Jander, K. Pelz, S. Heinker, F. Daume, A. Rahm, A. Braun, M. Grundmann, "The Influence of Front Contact and Buffer Layer Properties on CIGSe Solar Cell Breakdown Characteristics", in: *26<sup>th</sup> Eur. Photovolt. Sol. Energy Conf. Exhib.*, 2011: pp. 2432–2434. <https://doi.org/10.4229/26thEUPVSEC2011-3CO.4.6>.
  - [40] S. Puttnins, S. Jander, A. Wehrmann, G. Benndorf, M. Stölzel, A. Müller, H. von Wenckstern, F. Daume, A. Rahm, M. Grundmann, "Breakdown characteristics of flexible  $\text{Cu}(\text{In,Ga})\text{Se}_2$  solar cells", *Sol. Energy Mater. Sol. Cells*. 120 (2014) 506–511. <https://doi.org/10.1016/j.solmat.2013.09.031>.
  - [41] P. Szaniawski, P. Zabierowski, J. Olsson, U. Zimmermann, M. Edoff, "Advancing the Understanding of Reverse Breakdown in  $\text{Cu}(\text{In,Ga})\text{Se}_2$  Solar Cells", *IEEE J. Photovoltaics*. 7 (2017) 1136–1142. <https://doi.org/10.1109/JPHOTOV.2017.2699860>.



- [42] S. Puttnins, M. Purfurst, M. Hartung, H.K. Lee, F. Daume, L. Hartmann, A. Rahm, A. Braun, M. Grundmann, "The influence sodium on CIGSe solar cell breakdown characteristics", in: *27<sup>th</sup> Eur. Photovolt. Sol. Energy Conf. Exhib.*, 2012: pp. 2219–2221. <https://doi.org/10.4229/27thEUPVSEC2012-3CO.2.6>.
- [43] L.M. Mansfield, K. Bowers, S. Glynn, I.L. Repins, "The Effects of Absorber Thickness on Reverse-Bias Damage in Cu(In,Ga)Se<sub>2</sub> Solar Cells", in: *2019 IEEE 46<sup>th</sup> Photovolt. Spec. Conf.*, 2019.
- [44] M. Nardone, S. Dahal, "Anomalous Reverse Breakdown of CIGS Devices: Theory and Simulation", *MRS Adv.* 2 (2017) 3163–3168. <https://doi.org/10.1557/adv.2017.345>.
- [45] M. Theelen, H. Steijvers, K. Bakker, J. Vink, S. Mortazavi, A. Mulder, N. Barreau, D. Roosen, E. Haverkamp, "The exposure of CIGS solar cells to different electrical biases in a damp-heat illumination environment", in: *2016 IEEE 43<sup>rd</sup> Photovolt. Spec. Conf.*, IEEE, 2016: pp. 0929–0934. <https://doi.org/10.1109/PVSC.2016.7749746>.
- [46] S. Mortazavi, K. Bakker, J. Carolus, M. Daenen, G. de Amorim Soares, H. Steijvers, A. Weeber, M. Theelen, "Effect of Reverse Bias Voltages on small scale gridded CIGS Solar Cells", in: *2017 IEEE 44<sup>th</sup> Photovolt. Spec. Conf.*, IEEE, 2017: pp. 2875–2880. <https://doi.org/10.1109/PVSC.2017.8366514>.
- [47] S. Kijima, T. Nakada, "High-Temperature Degradation Mechanism of Cu(In,Ga)Se<sub>2</sub>-Based Thin Film Solar Cells", *Appl. Phys. Express.* 1 (2008) 075002. <https://doi.org/10.1143/APEX.1.075002>.
- [48] N.J. Biderman, S.W. Novak, R. Sundaramoorthy, P. Haldar, J.R. Lloyd, "Insights into cadmium diffusion mechanisms in two-stage diffusion profiles in solar-grade Cu(In,Ga)Se<sub>2</sub> thin films", *Appl. Phys. Lett.* 107 (2015). <https://doi.org/10.1063/1.4937000>.
- [49] S.-H. Chen, W.-T. Lin, S.-H. Chan, S.-Z. Tseng, C.-C. Kuo, S.-C. Hu, W.-H. Peng, Y.-T. Lu, "Photoluminescence Analysis of CdS/CIGS Interfaces in CIGS Solar Cells", *ECSJ. Solid State Sci. Technol.* 4 (2015) P347–P350. <https://doi.org/10.1149/2.0041509jss>.
- [50] K. Bakker, H.N. Åhman, T. Burgers, N. Barreau, A. Weeber, M. Theelen, "Propagation mechanism of reverse bias induced defects in Cu(In,Ga)Se<sub>2</sub> solar cells", *Sol. Energy Mater. Sol. Cells.* 205 (2020) 110249. <https://doi.org/10.1016/j.solmat.2019.110249>.
- [51] H. Guthrey, M. Nardone, S. Johnston, J. Liu, A. Norman, J. Moseley, M. Al-Jassim, "Characterization and modeling of reverse-bias breakdown in Cu(In,Ga)Se<sub>2</sub> photovoltaic devices", *Prog. Photovoltaics Res. Appl.* 27 (2019) 812–823. <https://doi.org/10.1002/pip.3168>.
- [52] M. Theelen, K. Beyeler, H. Steijvers, N. Barreau, "Stability of CIGS solar cells under illumination with damp heat and dry heat: A comparison", *Sol. Energy Mater. Sol. Cells.* 166 (2017) 262–268. <https://doi.org/10.1016/j.solmat.2016.12.039>.
- [53] M. Theelen, K. Bakker, H. Steijvers, S. Roest, P. Hielkema, N. Barreau, E. Haverkamp, "In Situ Monitoring of the Accelerated Performance Degradation of Solar Cells and Modules : A Case Study for Cu(In,Ga)Se<sub>2</sub> Solar Cells", *J. Vis. Exp.* 140 (2018). <https://doi.org/10.3791/55897>.
- [54] F. Couzinié-Devy, N. Barreau, J. Kessler, "Re-investigation of preferential orientation of Cu(In,Ga)Se<sub>2</sub> thin films grown by the three-stage process", *Prog. Photovoltaics Res. Appl.* 19 (2011) 527–536. <https://doi.org/10.1002/pip.1079>.
- [55] S. Roy, P. Guha, S.N. Kundu, H. Hanzawa, S. Chaudhuri, A.K. Pal, "Characterization of Cu(In,Ga)Se<sub>2</sub> films by Raman scattering", *Mater. Chem. Phys.* 73 (2002) 24–30. [https://doi.org/10.1016/S0254-0584\(01\)00345-5](https://doi.org/10.1016/S0254-0584(01)00345-5).

- [56] V. Izquierdo-Roca, X. Fontané, E. Saucedo, J.S. Jaime-Ferrer, J. Álvarez-García, A. Pérez-Rodríguez, V. Bermudez, J.R. Morante, "Process monitoring of chalcopyrite photovoltaic technologies by Raman spectroscopy: an application to low cost electrodeposition based processes", *New J. Chem.* 35 (2011) 453–460. <https://doi.org/10.1039/C0NJ00794C>.
- [57] F. Oliva, S. Kretzschmar, D. Colombara, S. Tombolato, C.M. Ruiz, A. Redinger, E. Saucedo, C. Broussillou, T.G. de Monsabert, T. Unold, P.J. Dale, V. Izquierdo-Roca, A. Pérez-Rodríguez, "Optical methodology for process monitoring of chalcopyrite photovoltaic technologies: Application to low cost Cu(In,Ga)(S,Se)<sub>2</sub> electrodeposition based processes", *Sol. Energy Mater. Sol. Cells.* 158 (2016) 168–183. <https://doi.org/10.1016/j.solmat.2015.12.036>.
- [58] P.C. Clemmow, "An introduction to electromagnetic theory", University Press, Cambridge, U.K., 1973.
- [59] A.M. Gabor, J.R. Tuttle, D.S. Albin, M.A. Contreras, R. Noufi, A.M. Hermann, "High efficiency CuIn<sub>x</sub>Ga<sub>1-x</sub>Se<sub>2</sub> solar cells made from (In<sub>x</sub>Ga<sub>1-x</sub>)<sub>2</sub>Se<sub>3</sub> precursor films", *Appl. Phys. Lett.* 65 (1994) 198–200. <https://doi.org/10.1063/1.112670>.
- [60] K. Bakker, S. Assen, A. Rasia, N. Barreau, A. Weeber, M. Theelen, "Fundamental Mechanisms Behind the Reverse Characteristic of Cu(In,Ga)Se<sub>2</sub> Solar Cells", *IEEE J. Photovoltaics.* 12 (2022) 1412–1417. <https://doi.org/10.1109/JPHOTOV.2022.3196827>.
- [61] W. Herrmann, M.C. Alonso, "Behaviour of Thin-Film Modules Under Shading", in: *19<sup>th</sup> Eur. Photovolt. Sol. Energy Conf. Exhib.*, Paris, 2004: pp. 2685–2688.
- [62] S. Dongaonkar, J.D. Servaites, G.M. Ford, S. Loser, J. Moore, R.M. Gelfand, H. Mohseni, H.W. Hillhouse, R. Agrawal, M.A. Ratner, T.J. Marks, M.S. Lundstrom, M.A. Alam, "Universality of non-Ohmic shunt leakage in thin-film solar cells", *J. Appl. Phys.* 108 (2010) 124509. <https://doi.org/10.1063/1.3518509>.
- [63] B.L. Williams, S. Smit, B.J. Niknie, K.J. Bakker, W. Keuning, W.M.M. Kessels, R.E.I. Schropp, M. Creatore, "Identifying parasitic current pathways in CIGS solar cells by modelling dark J-V response", *Prog. Photovoltaics Res. Appl.* 23 (2015) 1516–1525. <https://doi.org/10.1002/pip.2582>.
- [64] T. Walter, "Reliability Issues of CIGS-Based Thin Film Solar Cells", in: *Semicond. Semimetals*, 1<sup>st</sup> ed., Elsevier Inc., 2015: pp. 111–150. <https://doi.org/10.1016/bs.semsem.2015.05.001>.
- [65] S. Wendlandt, S. Berendes, T. Weber, J. Berghold, S. Krauter, P. Grunow, "Shadowing Investigations on Thin Film Modules", in: *32<sup>nd</sup> Eur. Photovolt. Sol. Energy Conf. Exhib.*, 2016: pp. 2270–2276. <https://doi.org/10.4229/EUPVSEC20162016-5BV.4.33>.

**IEEE copyright/ credit notice:**

Chapter 4: © 2019 IEEE. Reprinted, with permission, from K. Bakker, H. Nilsson Ahman, K. Aantjes, N. Barreau, A. Weeber, and M. Theelen, "Material Property Changes in Defects Caused by Reverse Bias Exposure of CIGS Solar Cells," *IEEE J. Photovoltaics*, Nov. 2019.

Chapter 7: © 2022 IEEE. Reprinted, with permission, from K. Bakker, J. C. Matas, J. Bosman, N. Barreau, A. Weeber, and M. Theelen, "Determining the decomposition voltage of Cu(In<sub>x</sub>Ga<sub>x</sub>)Se<sub>2</sub>" in 2022 IEEE 49<sup>th</sup> Photovoltaics Specialists Conference (PVSC), Jun. 2022.

Chapter 8: © 2022 IEEE. Reprinted, with permission, from K. Bakker, S. Assen, A. Rasia, N. Barreau, A. Weeber, and M. Theelen, "Fundamental Mechanisms Behind the Reverse Characteristic of Cu(In,Ga)Se<sub>2</sub> Solar Cells," *IEEE J. Photovoltaics*, Nov. 2022.



# Summary

The world is in an energy transition, from fossil fuels towards renewable energy sources like solar and wind energy. Solar photovoltaic (PV) is no longer installed only on large farms or roofs, but also in more demanding applications such as vehicles. These applications often require flexible solar cells, and thin-film  $\text{Cu(In,Ga)(Se,S)}_2$  (CIGS) is an excellent candidate for these demanding applications, since it can be fabricated on flexible substrates. Because CIGS is a direct bandgap semiconductor, the solar cells can be made much thinner than the conventional crystalline silicon (c-Si) cells. However, new applications also come with an increased exposure to uncontrollable stress factors like partial shading.

During partial shading the shaded cells are forced to dissipate energy from the current generated by the non-shaded cells due to the electrical series connection. Since the current is equal for all cells in series, the polarity of the voltage over the shaded cells will be reversed. This is often referred to as reverse bias (voltage). The literature review (Chapter 3) shows that it is known that small defects are formed in CIGS cells during partial shading and under reverse bias conditions. These defects have a very distinct appearance and are therefore often named wormlike defects. Wormlike defects are small local defects that permanently degrade the power output of CIGS solar cells. Often, every consecutive shading event leads to the formation of new wormlike defects. The effect of a small single defect on a large module is neglectable. However, the power output of a module can locally be severely impacted when there is a high concentration of wormlike defects.

For this dissertation the formation and propagation of wormlike defects was studied, as well as the reverse  $J/V$  characteristics. The reverse  $J/V$  characteristic shows the electrical behavior of the CIGS solar cells at negative (or reverse) voltages. This is the voltage range of shaded cells in a partially shaded CIGS module where wormlike defects appear. The next sections will describe the results of the studies on the formation and propagation of wormlike defects, and the reverse  $J/V$  characteristic.

## Wormlike defects

During reverse bias exposure of CIGS solar cells local hotspots can occur that propagate through the cell. The propagating hotspot leaves behind local defects that act as shunts. These defects form trails that show unique visual patterns and are therefore often referred to as wormlike defects. The propagation mechanism of the defects responsible for the trails was studied in Chapter 4 and Chapter 5. The wormlike defects were been extensively studied using Scanning Electron Microscopy (SEM) with and without Energy-Dispersive X-ray spectroscopy (EDX), Raman spectroscopy, photoluminescence (PL), and (confocal) microscopy. It was shown that wormlike defects consist of individual islands of porous expanded material. The exact composition of the defect is difficult to determine, however, at the edges there are subtle differences in composition. This observation is the basis for the propagation model introduced in Chapter 4. In this model the islands are created by a chemical reaction that alters the composition and morphology of the CIGS material. This chemical reaction is responsible for the observed hotspot during propagation, and requires fuel in the form of elements from the solar cell stack in order to sustain itself. During the chemical reaction some elements are used from the surrounding CIGS absorber area, reducing the material quality outside the area of the hotspot. The reaction is finished when the hotspot hops to a next spot where the conditions are more favorable. These conditions include temperature, material quality and electric field.

The influence of the local electric field during the propagation phase of the defects was studied in Chapter 5. This was done by changing the conductivity of the current collecting window layer on top of the CIGS solar cell, thereby manipulating the voltage drop over the window layer close to the hotspot. This lateral voltage drop over the window layer is dictating the voltage over the layer stack, and thus the local electric field. This local electric field is necessary for the hotspot to hop to a new location. When the electric field close to the hotspot was reduced the hotspot remained stationary and expanded. This is in strong contrast to the large trails observed with a high electric field close to the hotspot.

The most important question; "What are the conditions require to form wormlike defects?", was studied in Chapter 6. In this chapter, the voltage and current at which wormlike defects are formed were determined for a large number of samples. From the obtained large dataset it was concluded

that the formation of wormlike defects is a voltage driven process, and that the voltage required to form a wormlike defect strongly depends on the thickness and quality of the CIGS absorber layer. Cells with an absorber layer thickness around 1800 nm on average developed wormlike defects around -6 V, where the highest voltage to start forming wormlike defects for this batch of cells was -2 V. This means that one cell should not be exposed to more than 2 V in reverse to prevent wormlike defects. This results in a maximum of two illuminated cells in series connected to one shaded cell, taking into account that the  $V_{oc}$  of CIGS cells easily exceeds 0.7 V. This is only applicable for the cells used in this dissertation and can be different for other cells. Also, the voltage required for a possible additional electronic device, like a bypass diode, is not accounted for.

The results of Chapter 5 and Chapter 6 show the strong dependency of the electric field over the CIGS absorber on both the formation and propagation of wormlike defects. Therefore, a final experiment was designed in Chapter 7 to evaluate the impact of the electric field on the CIGS absorber material. In order to do this a dedicated sample configuration was made that enabled direct electrical *IV* measurement of the CIGS absorber. Using a one-dimensional approach, it was shown that the CIGS absorber has a decomposition voltage which depends on the composition of the CIGS. The hypothesis was that the CIGS decomposes into a copper poor material, known as Ordered Vacancy Compound (OVC), and highly conductive copper selenide ( $\text{Cu}_2\text{Se}$ ). However, after the test the same material as in the wormlike defects was found, and no traces of OVC or  $\text{Cu}_2\text{Se}$  were observed. This indicates that the decomposition of CIGS in OVC and  $\text{Cu}_2\text{Se}$  is an intermediate step in a very aggressive overall reaction.

## Reverse *IV* characteristic

Chapter 8 describes the study of the fundamental mechanisms behind the reverse *IV* characteristic of CIGS solar cells. The reverse *IV* characteristic describes the electrical behavior of the solar cells at negative voltages. Electrically a CIGS solar cell behaves as an insulator at small negative voltages and will transition into a conductor at larger negative voltages. This transition is visible as a sharp increase in current in the current-voltage graph. The negative voltage at which the current starts to rise is called the transition voltage. The transition voltage strongly depends on illumination

intensity and temperature.

In Chapter 6 it was shown that the formation of wormlike defects is a voltage driven process, and that there is a difference in the probability of the formation of wormlike defects between cells in the dark and under illumination. In the dark cells have a larger transition voltage, and when exposed to reverse bias they have an extremely large probability of forming wormlike defects. This in contrast to cells exposed to reverse bias voltages under illumination, which have a much smaller negative transition voltage, and have a possibility close to zero of forming wormlike defects.

The rationale behind the experiment described in Chapter 8 is that by understanding the mechanism behind the transition, it might be possible to find ways to reduce the transition voltage in the dark to a much smaller negative voltage. In such a case the solar cell acts as if it has a built-in bypass diode. In the experiment a series of temperature and illumination dependent measurements were performed and different models were used to fit the reverse bias  $J/V$  curves obtained. Based on how well the different models were able to fit the measurements, the fundamental mechanisms behind the reverse characteristic were identified. It was found that there are three parallel mechanisms that contribute to the reverse bias current, and these are:

- Shunt resistance: a small Ohmic leakage current
- Space charge limited current: mechanism that describes the small non-Ohmic leakage current
- Fowler–Nordheim mechanism: specific tunneling mechanism that is responsible for the sharp increase in current for reverse voltages larger than the transition voltage

The current through the shunt resistance and the space charge limited current are dominant at small reverse voltages and determine the insulating behavior before the transition voltage. The Fowler–Nordheim mechanism is responsible for the conductive behavior after the transition voltage. The Fowler–Nordheim tunneling barrier is located somewhere in the complex stack between the front contact and the bulk of the CIGS absorber. More research is required to determine the exact nature of this barrier.

The measurements also confirmed the negative temperature coefficient for the transition voltage. At higher temperatures, there will be a higher

current at the same voltage. This means that ,during reverse bias operation, a small local hotspot will start to conduct more current resulting in an increase in temperature. This will increase the risk of thermal runaway, as an increase in current will lead to a rise in temperature, starting a vicious circle.

## **Concluding remarks**

Partial shading of CIGS PV modules can lead to the formation of harmful wormlike defects. This is caused by an unfavorable material property of CIGS; the CIGS absorber decomposes under the influence of the large electric field caused by partial shading. Especially the traditional monolithically interconnected modules are very susceptible to reverse bias damage. Fortunately the CIGS market is moving towards modules and applications in which large flexible cells are used. These cells can be perfectly protected against reverse bias with bypass diodes, as is common practice in c-Si modules.





# Samenvatting

De wereld bevindt zich in een energietransitie, van fossiele brandstoffen naar hernieuwbare energiebronnen zoals zon en wind energie. Fotovoltaïsche zonne-energie (PV) wordt niet alleen geïnstalleerd op grote velden of daken, maar ook steeds meer in andere toepassingen zoals op voertuigen. Deze applicaties vereisen vaak flexibele zonnecellen. Omdat de dunne-film  $\text{Cu(In,Ga)(Se,S)}_2$  (CIGS) technologie aangebracht kan worden op flexibele drager materialen is dit een uitstekende kandidaat voor deze toepassingen. CIGS is een halfgeleidermateriaal met een directe bandkloof en het kan hierdoor vele malen dunner zijn dan de traditionele kristallijn silicium (c-Si) zonnecellen. Desondanks komen de nieuwe applicaties ook met een verhoogde blootstelling aan ongecontroleerde degradatie omstandigheden zoals gedeeltelijke beschaduwing.

Tijdens gedeeltelijke beschaduwing worden de beschaduwde cellen gedwongen om energie te dissiperen die gegenereerd wordt door de niet-beschaduwde cellen, omdat de cellen elektrisch in serie met elkaar verbonden zijn. Bij een serieschakeling is de stroom door de cellen gelijk, hierdoor wordt de polariteit van de spanning over de beschaduwde cellen omgekeerd. In het Engels wordt dit aangeduid met de term “reverse bias”, wat letterlijk omgekeerde achtergrondspanning betekent. In het literatuuroverzicht (Hoofdstuk 3) staat beschreven dat kleine defecten gevormd worden in CIGS zonnecellen als ze worden blootgesteld aan gedeeltelijke beschaduwing en de resulterende reverse bias. Deze defecten hebben een erg specifiek uiterlijk en worden daardoor ook wel wormachtige defecten genoemd. Wormachtige defecten zijn kleine lokale defecten die het rendement van CIGS cellen permanent reduceren. Vaak zorgt elke opeenvolgende beschaduwingsactiviteit tot de creatie van nieuwe wormachtige defecten. Het effect van een klein defect is minimaal, maar het rendement van een PV module kan lokaal behoorlijk verminderen als er een hoge concentratie wormachtige defecten aanwezig is.

In dit proefschrift zijn de vorming en propagatie van wormachtige defecten en het negatieve deel van de  $JV$ -karakteristiek onderzocht. Het negatieve deel van de  $JV$ -karakteristiek, of de reverse  $JV$ -karakteristiek, beschrijft het elektrische gedrag van de CIGS zonnecel bij negatieve spanningen. Dit is het spanningsbereik waarin beschaduwde cellen zich

bevinden in een gedeeltelijk beschaduwde module, en waarin wormachtige defecten gevormd worden. De volgende secties beschrijven de resultaten van de studies naar de vorming en propagatie van wormachtige defecten, en het negatieve deel van de  $JV$ -karakteristiek.

### 9.2.1 Wormachtige defecten

Als een CIGS zonnecel wordt blootgesteld aan reverse bias kan er een lokale thermische hotspot ontstaan die zich voortbeweegt, of propageert, door de cel. Deze voortbewegende hotspot laat lokale defecten achter die zich als kortsluitingen gedragen. Deze defecten vormen een aaneengesloten spoor met een karakteristiek visueel patroon, en worden daarom ook wel wormachtige defecten genoemd. Het mechanisme dat verantwoordelijk is voor het propagatie patroon van de defecten staat beschreven in Hoofdstuk 4 en Hoofdstuk 5. De wormachtige defecten zijn uitgebreid bestudeerd, met behulp van onder andere Scanning Electron Microscopie (SEM) met en zonder Energy-Dispersive X-ray spectroscopie (EDX), Raman spectroscopie, fotoluminescentie (PL), en (confocale) microscopie. Het is aangetoond dat wormachtige defecten bestaan uit individuele eilanden van een poreus geëxpandeerd materiaal. Het is lastig om de exacte samenstelling van het defect te bepalen, maar aan de randen zijn er subtiele veranderingen in samenstelling waarneembaar. Deze observatie vormt de basis van een in Hoofdstuk 4 geïntroduceerd model om de propagatie te verklaren. In dit model worden de eilanden gevormd door een chemische reactie die de samenstelling en morfologie van het CIGS materiaal verandert. Deze chemische reactie is verantwoordelijk voor de voortbewegende hotspot die is waargenomen tijdens de propagatie fase. De hotspot heeft brandstof, in de vorm van elementen uit de verschillende lagen van de zonnecel, nodig om zichzelf in stand te houden. Hierdoor reageert een deel van de elementen uit het omliggende CIGS materiaal, met als gevolg dat de materiaalkwaliteit buiten de hotspot degradeert. De reactie is afgelopen als de hotspot verspringt naar een nieuwe locatie waar de omstandigheden gunstiger zijn. Deze omstandigheden zijn onder andere temperatuur, materiaalkwaliteit en elektrisch veld.

De invloed van het lokale elektrische veld op de propagatie van wormachtige defecten is beschreven in Hoofdstuk 5. Het onderzoek is uitgevoerd door de geleiding van de transparante stroom-collecterende

electrode (het voorcontact) bovenop de CIGS cel te beïnvloeden. Door dit te doen wordt de spanningsval over het voorcontact in de buurt van de hotspot gemanipuleerd. Deze laterale spanningsval dicteert lokaal de spanning over alle lagen van de zonnecel, en dus het lokale elektrische veld. Dit lokale elektrische veld is nodig voor de hotspot om naar een volgende locatie te verspringen. Als het lokale elektrische veld in de buurt van de hotspot wordt verminderd, blijft de hotspot stationair en dijt deze uit. Dit is in groot contrast met de lange sporen die zijn geobserveerd als er een groot elektrisch veld in de buurt van de hotspot aanwezig is.

De hoofdvraag: “Welke condities zijn nodig om wormachtige defecten te vormen?” wordt beantwoord in Hoofdstuk 6. In dit hoofdstuk zijn de stroom en spanning waarbij wormachtige defecten ontstaan, bepaald voor een groot aantal monsters. Uit de resultaten is geconcludeerd dat de vorming van wormachtige defecten een spanning-gedreven proces is. De spanning die nodig is om wormachtige defecten te vormen is afhankelijk van de kwaliteit en dikte van het CIGS absorber materiaal.

Bij cellen met een CIGS absorber laagdikte van rond de 1800 nm worden wormachtige defecten gemiddeld rond de -6 V gevormd, waarbij -2 V de hoogst gemeten spanning is waarbij defecten ontstaan (voor deze partij cellen). Dit betekent dat om wormachtige defecten te vermijden een cel niet mag worden blootgesteld aan een negatieve spanning groter dan 2 V. Hieruit volgt dat er een maximum van twee belichte cellen in serie mogen staan met een beschaduwde cel, rekening houdend met het feit dat de  $V_{oc}$  van een CIGS cel meer dan 0.7 V is. Dit is alleen van toepassing op de cellen gebruikt in dit proefschrift en dit kan verschillen voor andere cellen. Ook is er geen rekening gehouden met de spanning nodig voor een eventueel additioneel elektronisch component zoals een bypass diode.

De resultaten uit Hoofdstuk 5 en Hoofdstuk 6 laten de sterke afhankelijkheid van het elektrische veld over de CIGS absorber laag op zowel de vorming als propagatie van wormachtige defecten zien. Daarom is er in Hoofdstuk 7 een afsluitend experiment opgezet om de invloed van het elektrisch veld op het CIGS absorber materiaal te bestuderen. Om dit te bewerkstelligen is er een nieuw experimenteel monster ontwerp gemaakt waarmee het mogelijk is om directe elektrische IV metingen te verrichten aan de CIGS absorber laag. Met deze eendimensionale aanpak was het mogelijk om aan te tonen dat de CIGS absorber een ontledingsspanning heeft, die afhankelijk is van de samenstelling van het CIGS materiaal. De hypothese was dat CIGS ontleeft in een koperarm materiaal [Verbindingen

met geordende vacatures, of in het Engels Ordered Vacancy Compounds (OVC)], en hoog geleidend koper-selenide ( $\text{Cu}_2\text{Se}$ ). Na de testen werd er echter materiaal gevonden identiek aan de wormachtige defecten, en geen sporen van OVC of  $\text{Cu}_2\text{Se}$ . Dit is een indicatie dat de ontleding van CIGS in OVC en  $\text{Cu}_2\text{Se}$  een tussenstap is in een agressieve uitgebreidere reactie.

## 9.2.2 Negatieve $J/V$ -karakteristiek

Hoofdstuk 8 beschrijft de studie naar de fundamentele mechanismen achter de negatieve  $J/V$ -karakteristiek van CIGS zonnecellen. De negatieve  $J/V$ -karakteristiek beschrijft het elektrisch gedrag van een zonnecel bij negatieve spanningen. Elektrisch gezien gedraagt een CIGS zonnecel zich als een isolator bij kleine negatieve spanningen en gaat over naar het gedrag van een geleider bij grotere negatieve spanningen. Deze overgang is zichtbaar als een scherpe stijging van de stroom in de stroom-spanning karakteristiek. De negatieve spanning waar de stroom begint te stijgen wordt de overgangsspanning genoemd. Deze overgangsspanning is sterk afhankelijk van temperatuur en belichtingsintensiteit.

In Hoofdstuk 6 is aangetoond dat de vorming van wormachtige defecten een spanning-gedreven proces is en dat er een groot verschil is in de kans op vorming van wormachtige defecten tussen cellen in het donker of onder belichting. In het donker hebben cellen een grote overgangsspanning en als ze blootgesteld worden aan negatieve spanningen is de kans groot dat wormachtige defecten gevormd worden. Dit is in tegenstelling tot cellen die onder belichting blootgesteld worden aan negatieve spanningen. De kans om in deze cellen wormachtige defecten te vormen is nihil, omdat deze een veel kleinere negatieve overgangsspanning hebben.

De gedachte achter het experiment, beschreven in Hoofdstuk 8, is dat door het begrijpen van de mechanismen achter de overgang het mogelijk zou moeten zijn om de overgangsspanning in het donker te verlagen naar een veel kleinere negatieve spanning. In dat geval functioneert de zonnecel alsof het een ingebouwde bypass diode heeft.

Voor het experiment zijn een reeks van temperatuur- en belichtingsafhankelijke metingen uitgevoerd. Deze metingen zijn gefit aan verscheidene modellen. De fundamentele mechanismen achter de negatieve  $J/V$ -karakteristiek zijn geïdentificeerd op basis van de kwaliteit van de fits. Er is aangetoond dat er drie mechanismen in parallel bijdragen aan de stroom bij negatieve spanningen, deze zijn:

- Parallele weerstand: een kleine Ohmse lekstroom
- Space charge limited current (SCLC): stroom gelimiteerd door de ruimtelijke lading (de depletielaag). Dit is een mechanisme dat de kleine niet-Ohmse lekstroom beschrijft
- Fowler–Nordheim mechanisme: dit is een specifiek tunneling mechanisme dat verantwoordelijk is voor de scherpe stijging van de stroom bij negatieve spanningen groter dan de overgangsspanning

De stroom door de parallelle weerstand en de SCLC zijn dominant bij kleine negatieve spanningen, en bepalen het gedrag als isolator voor de transitie spanning. Het Fowler–Nordheim mechanisme is verantwoordelijk voor het gedrag als een geleider na de overgangsspanning. De Fowler–Nordheim tunnelbarrière bevindt zich in de complexe laagstructuur tussen het voorcontact en de bulk van de CIGS absorber. Er is meer onderzoek nodig om de exacte aard van deze barrière te bepalen.

De metingen hebben ook de negatieve temperatuurcoëfficiënt van de overgangsspanning bevestigd. Bij hogere temperaturen zal er een hogere stroom lopen bij een gelijke spanning. Dit betekent dat ,bij een cel onderworpen aan een negatieve spanning, een kleine lokale hotspot meer stroom zal trekken, met als gevolg een toename van de temperatuur. Dit verhoogt het risico dat de temperatuur ongecontroleerd oploopt; een verhoging van de stroom leidt tot een verhoging van temperatuur, dit kan het begin zijn van een vicieuze cirkel.

### 9.2.3 Afsluitende opmerkingen

Gedeeltelijke beschaduwning van CIGS PV modules kan leiden tot de vorming van wormachtige defecten. Dit wordt veroorzaakt door een ongunstige materiaaleigenschap van CIGS: de CIGS absorber ontleedt als het wordt blootgesteld aan een elektrisch veld dat het gevolg is van gedeeltelijke beschaduwning. Vooral de traditionele monolithisch geïntergeconnecteerde modules zijn gevoelig voor schade door reverse bias. De CIGS markt verschuift naar toepassingen en modules waarin grotere flexibele cellen worden toegepast. Deze cellen kunnen perfect worden beschermd tegen reverse bias door gebruik te maken van bypass diodes, zoals gebruikelijk is bij c-Si modules.



# Appendix A

Table that contains a list of the available literature that describes shading tests on CIGS modules

Abbreviations used in the table:

$L_{sh}$  and  $W_{sh}$ : length and width of shading mask, respectively, according to Figure 3-5, Mi: monolithically interconnected, C: non-monolithically interconnected,  $T_{mod}$ : module temperature, CIS: CuInSe<sub>2</sub>,  $I_{sc}$ : short circuit current,  $I_{mp}$ : current at maximum power point,  $\eta$ : efficiency,  $V_{oc}$ : open circuit voltage,  $FF$ : fill factor.

Notes:

<sup>a</sup>Data were anonymized in such a way that the distinction between CIGS and CdTe could not be made.

<sup>b</sup>Loss in parameters are relative to before application of stress. For example -10%  $\eta$  means that a module went from an efficiency of 20% before the test to an efficiency of 18% after the test.

<sup>c</sup>IV parameters at standard test conditions. If also low light measurements were performed, this is indicated in the last column.

<sup>d</sup>Tzikas *et al.* [15] also measured IV after several weeks of dark storage.

<sup>e</sup>Wendlandt *et al.* [10] started with stabilized modules.

<sup>f</sup>Silverman *et al.* [17] used a 100% opaque mask at a distance of 1 m outdoor that was moved in such a way that the shadow passed over the full width of the module in 20 s.

<sup>g</sup>Silverman *et al.* [14], tested the influence of real humans and cleaning tools (no artificial masks).

<sup>h</sup>In c-Si modules often breakage of glass and melting of encapsulant has been observed; therefore, a non-critical hotspot does not generate sufficient heat to break the glass or melt the encapsulant.



**Table A-1:** List of available literature that describes shading tests on CIGS modules

<b>Publication</b>	<b>Modules used</b>	<b>Sequence</b>	<b>Mask</b>
First author	Nr of modules description	Preconditioning	Scenario
Year		Stress	Opacity
Reference		Postconditioning	$L_{sh}/W_{sh}$
Herrmann	2 Commercial Mi CIS	Light soak	Typical
2004		Shading indoor	75-100%
[61]		...	Worst case/100%
Mack	1 50-cell module	...	Typical
2008		Shading indoor	100%
[27]		Light soak	1 cell/100%
Dongaonkar	1 Commercial Mi	...	Ass-Typ
2013		...	73%
[21]		...	19 cm/75%
Silverman	1 Commercial Mi	...	Typical
2015		Shading outdoor	90%
[22]		...	10 cells/50%
Silverman	3 Commercial Mi	Light soak @mpp	Typical
2015		Shading indoor	90%
[17]		Light soak @mpp	Worst case/90%
Wendlandt	3 Commercial Mi	Light soak	10 different
2016		Shading indoor	100%
[65]		...	...

<b>Repetitions / sequence</b>	<b>Relative change<sup>b</sup> in <i>IV</i> parameters<sup>c</sup></b>	<b>Impact</b>	<b>Remark</b>
...	...	...	...
1 <sup>st</sup> determine worst case. 2 <sup>nd</sup> hot spot endurance test	-4.1 and -18.2% $\eta$	Uncritical hotspots <sup>h</sup>	Deriving of "old" IEC 61646 standard
...	-6% $\eta$ loss in $V_{oc}$ and $FF$	...	Improvement with light soaking
...	...	...	Only thermal results
...	...	...	Heating from localized shunting
New mask position till 50% of module was stressed	-4.7, -6.5, -10.5% $\eta$	Local shunts in EL. Visible defects	-4.2, -6.1, -11.4 $\eta$ after light soaking. New shunts after subsequent test
10 scenarios on each module	...	Uncritical hotspots <sup>h</sup> . Visible defects	Only studied hotspots

**Table A-1:** List of available literature that describes shading tests on CIGS modules (continued)

Publication	Modules used	Sequence	Mask
Silverman	1 Commercial Mi CIGS + CdTe <sup>a</sup>	Light soak @mpp	Typical
2016		Shading outdoor	100% @ 1m <sup>f</sup>
[28]		Light soak @mpp	75 mm/90%
Silverman	6 Commercial Mi CIGS + CdTe <sup>a</sup>	Light soak @mpp	Typical
2016		Shading indoor	90%
[28]		Light soak @mpp	Worst case/90%
Lee	3 Commercial Mi	...	Typical
2016		Shading indoor	100%
[29]		...	0-100%/100%
Silverman	6 Commercial Mi CIGS + CdTe <sup>a</sup>	Light soak @mpp	Humans + cleaning tools <sup>g</sup>
2017		Shading outdoor	
[25]		Light soak @mpp	
Tzikas	6 Commercial Mi 1 Commercial C	...	Symmetric + asymmetric
2017		Shading indoor	100%
[26]		... <sup>d</sup>	0-100%/0-100%
Wendlandt	1 Commercial Mi	... <sup>e</sup>	Typical
2018		Shading indoor	10%/100%
[19]		...	100%
Silverman	6 Commercial Mi CIGS + CdTe <sup>a</sup>	Light soak @mpp	Human body and cleaning tool
2018		Shading outdoor	90 and 100%
[18]		Light soak @mpp	NA

<b>Repetitions / sequence</b>	<b>Relative change<sup>b</sup> in IV parameters<sup>c</sup></b>	<b>Impact</b>	<b>Remark</b>
...	-5% $\eta$	Local shunts in EL. Wormlike (serpentine) defects	-7% $\eta$ after light soak
New mask position till 50% of module was stressed	-3 to -11% $\eta$	Local shunts in EL.	-4 to -14% $\eta$ after light soak (2 out of 6 improved)
10 times, progressing. Cover from 0 to 100%	-2.3% $\eta$ -1.8% FF	Local shunts in EL. Wormlike defects	Only IV data for 1 out of 3 modules
>6	-25% $I_{mp}/I_{sc}$ (worst module)	Local shunts in EL.	New shunts formed every repetition
Progressing 5% increment. Cover from 0 to 100%	-2 to -8% $\eta$	Local shunts in EL. Wormlike defects	Improvement after dark storage
10 times new mask position	+0.7% $\eta$	Local shunts in EL.	-15.9% $\eta$ at 100 W/m <sup>2</sup>
33 times 7 different tests, new module each test	-2 to -27% $\eta$	Local shunts in EL.	Bigger losses at lower intensities

# Appendix B

## Additional measurements comparing fixed and auto-change current range setting

Comparison of results of measurements with SMU set to fixed current range of 100 mA and on auto-change. The main parameters of the substrate used for this comparison can be found in Table B-1. The histograms for both types of measurements for both damage current density and damage voltage can be found in Figure B-1

**Table B-1:** Parameters of additional substrate, including the average absorber thickness, solar cell efficiency and damage voltage for both the dark (DRB) reverse bias sweeps with auto-change and fixed current range. The average values are based on more than 30 measurement points per substrate, the error is the standard deviation. Also in the table is the percentage of cells that were damaged in sweeps with auto-change and fixed current range together with the number of cells (*n*) used to calculate this damage ratio.

Substrate	Absorber thickness [nm]	Efficiency [%]	<i>n</i> cell DRB auto-change	DRB auto-change damage ratio	DRB auto-change $V_{damage}$ [V]	<i>n</i> cells DRB fixed-range	DRB fixed-range damage ratio	DRB fixed-range $V_{damage}$ [V]
Additional	1774±32	13.6±0.6	48	83%	5.8±1.6	47	68%	6.2±1.4

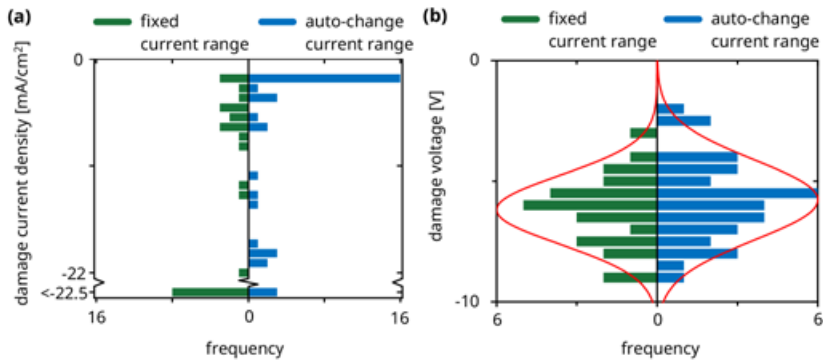


**Figure B-1: (a)** Histograms of damage current density in dark reverse bias sweeps with on the left results of fixed current range and on the right the auto-change current range results. The last bin (bottom) represents the number of cells with a damage current density smaller than 22.5 mA/cm<sup>2</sup>. **(b)** Histograms of damage voltage in dark reverse bias sweep and the normal distribution curve based on average and standard deviation for measurements performed with fixed and auto-change current range.

# Appendix C

## List of abbreviations

Al:ZnO	aluminum doped zinc oxide
AM 1.5	Air Mass 1.5
at%	atom percent
AZO	Aluminum doped Zinc Oxide
BIPV	Building Integrated PhotoVoltaics
CBD	Chemical Bath Deposition
Cd <sub>Cu</sub>	substitutional cadmium (at copper vacancy)
Cd <sub>Ga</sub>	substitutional cadmium (at gallium vacancy)
Cd <sub>In</sub>	substitutional cadmium (at indium vacancy)
CdS	cadmium sulfide
CdTe	cadmium telluride
CGI	Copper / (Gallium + Indium)
CIGS	Copper Indium Gallium diSelenide (Cu(In <sub>1-x</sub> Ga <sub>x</sub> )Se <sub>2</sub> )
c-Si	crystalline silicon
DC	Direct Current
DRB	reverse <i>J/V</i> sweep in the dark
EBIC	Electron Beam Induced Current
ECN	Energy research Centre of the Netherlands
EDX	Energy-Dispersive X-ray spectroscopy
EL/PL	ElectroLuminescence / PhotoLuminescence
FF	Fill Factor
FIB	Focused Ion Beam
FN	Fowler–Nordheim
GGI	Gallium / (Gallium + Indium)
HAc	acetic acid
HCl	hydrochloric acid
<i>I</i>	current in ampere
IEC	International Electrotechnical Commission
IR	InfraRed
<i>IV</i>	current - Voltage
<i>i</i> -ZnO	intrinsic zinc oxide

---

$J$	current density in mA/cm <sup>2</sup>
$J_{sc}$	short circuit current density in mA/cm <sup>2</sup>
$JV$	current density - Voltage
LCOE	Levelized Cost Of Electricity
LED	Light Emitting Diode
LRB	illuminated reverse $JV$ sweep
mpp	maximum power point
OVC	Ordered Vacancy Compound
P1	Patterning line 1
P2	Patterning line 2
P3	Patterning line 3
PDT	Post Deposition Treatment
PF	Poole-Frenkel
PL	PhotoLuminescence
PR	Performance Ratio
PV	PhotoVoltaic
$R$	Resistance in $\Omega$ or $\Omega\text{cm}^2$
RB	Reverse Bias
$R_{series}$	series resistance in $\Omega$ or $\Omega\text{cm}^2$
$R_{shunt}$	shunt resistance in $\Omega$ or $\Omega\text{cm}^2$
SCLC	Space Charge Limited Current
SEM	Scanning Electron Microscopy
SEM – EDX	Scanning Electron Microscopy-Energy-Dispersive X-ray spectroscopy
SLG	Soda-Lime Glass
SMU	Source Measure Unit
sr-PL	spectrally resolved PhotoLuminescence
TCO	Transparent Conductive Oxide
TNO	Netherlands organisation for applied scientific research (Nederlandse organisatie voor Toegepast Natuurwetenschappelijk Onderzoek)
$V$	Voltage in volt
VIR	Variable irradiance measurements
$V_{oc}$	open circuit voltage in volt
$V_{tr}$	transition Voltage in Volt
ZnO	Zinc Oxide
ZTO	Zinc Tin Oxide (ZnSnO)



# List of publications

## Peer review publications related to this dissertation:

**K. Bakker**, H. Nilsson Ahman, K. Aantjes, N. Barreau, A. Weeber, and M. Theelen, "Material Property Changes in Defects Caused by Reverse Bias Exposure of CIGS Solar Cells," *IEEE J. Photovoltaics*, vol. 9, no. 6, pp. 1868–1872, Nov. 2019, doi: 10.1109/JPHOTOV.2019.2940486.

**K. Bakker**, A. Weeber, and M. Theelen, "Reliability implications of partial shading on CIGS photovoltaic devices: A literature review," *J. Mater. Res.*, vol. 34, no. 24, pp. 3977–3987, Dec. 2019, doi: 10.1557/jmr.2019.373.

**K. Bakker**, H. N. Åhman, T. Burgers, N. Barreau, A. Weeber, and M. Theelen, "Propagation mechanism of reverse bias induced defects in Cu(In,Ga)Se<sub>2</sub> solar cells," *Sol. Energy Mater. Sol. Cells*, vol. 205, p. 110249, Feb. 2020, doi: 10.1016/j.solmat.2019.110249.

**K. Bakker**, A. Rasia, S. Assen, B. Ben Said Aflouat, A. Weeber, and M. Theelen, "How the absorber thickness influences the formation of reverse bias induced defects in CIGS solar cells," *EPJ Photovoltaics*, vol. 11, no. 9, Nov. 2020, doi: 10.1051/epjpv/2020006.

R. Aninat, **K. Bakker**, L. Jouard, M. G. S. Ott Cruz, P. Yilmaz, and M. Theelen, "Extraction and microscopic analysis of partial shading-induced defects in a commercial CIGS PV module," *Prog. Photovoltaics Res. Appl.*, Nov. 2021, pp. 1–14, 2022, doi: 10.1002/pip.3561.

**K. Bakker**, S. Assen, A. Rasia, N. Barreau, A. Weeber, and M. Theelen, "Fundamental Mechanisms Behind the Reverse Characteristic of Cu(In,Ga)Se<sub>2</sub> Solar Cells," *IEEE J. Photovoltaics*, pp. 1–6, 2022, doi: 10.1109/JPHOTOV.2022.3196827.

## Conference contributions related to this dissertation:

Mortazavi, S., **K. Bakker**, J. Carolus, M. Daenen, G. de Amorim Soares, H. Steijvers, A. Weeber, and M. Theelen, "Effect of reverse bias voltages on small scale gridded CIGS solar cells," in: *2017 IEEE 44<sup>th</sup> Photovoltaic Specialist Conference (PVSC)*, Washington DC, United States, June 2017, poster presentation.

**K. Bakker**, P. César Pérez Galicia, F. Lanfranchi, C. Tzikas, A. Weeber, and M. Theelen, "Small scale CIGS Solar Cells exposed to Reverse Bias Voltages," in: *33<sup>rd</sup> European Photovoltaic Solar Energy Conference and Exhibition (EUPVSEC)*, Amsterdam, the Netherlands November 2017, poster presentation.

C. Tzikas, G. Gómez, M. van den Donker, **K. Bakker**, A.H.M. Smets, W. Folkerts, "Do thin film PV modules offer an advantage under partial shading conditions," in: *33<sup>rd</sup> European Photovoltaic Solar Energy Conference and Exhibition (EUPVSEC)*, Amsterdam, the Netherlands November 2017, poster presentation.

**K. Bakker**, E. Gaona Pena, A. Weeber, and M. Theelen, "Evaluation of Different Models to Describe Reverse Breakdown Characteristics of CIGS solar cells," in: *NREL Photovoltaic Reliability Workshop (PVRW)*, Denver, United States, February 2018, poster presentation.

**K. Bakker**, H. Nilsson Åhman, K. Aantjes, N. Barreau, A. Weeber, and M. Theelen, "Propagation of reverse bias induced wormlike defects in CIGS solar cells," in: *2019 IEEE 46<sup>th</sup> Photovoltaic Specialist Conference (PVSC)*, Chicago, United States, June 2019, oral presentation.

M. Theelen, T. Weber, and **K. Bakker**, "Degradation mechanisms in CIGS solar cells and modules," in: *E-MRS Spring Meeting*, Phoenix, United States, April 2019, invited presentation.

M. Theelen, J. Kroon, T. Weber, **K. Bakker**, D. Lincot, and JF. Guillemoles, "Degradation mechanisms in PV," in: *EuroCORR*, Sevilla, Spain, October 2019, keynote presentation.

**K. Bakker**, A. Rasia, S. Assen, B. Ben Said Aflouat, A. Weeber, and M. Theelen, "How the absorber influences the formation of reverse bias induced defects in CIGS solar cells," in: *E-MRS Spring Meeting*, virtual, May 2020, poster presentation.

R. Aninat, **K. Bakker**, L. Jouard, M. Campillay, G. Gomez, and M. Theelen, "Shunting defects induced by shading on a Cd-free commercial CIGS module," in: *E-MRS Spring Meeting*, virtual, May 2020, oral presentation.

**K. Bakker**, H. Nilsson Åhman, N. Barreau, K. Aantjes, T. Burgers, A. Weeber, and M. Theelen, "Propagation mechanism of wormlike defects in CIGS solar cells," in: *EuroCORR*, virtual, September 2020, oral presentation.

M. Theelen, T. Weber, A. Kingma, R. Aninat, E. Achterberg, R. Verhagen, R. van Gestel, B. Pieters, **K. Bakker**, A. Weeber, K. Mack, M. Riedel, B. Rau, M. Rennhofer, L. Plessing, V. Huhn, and E. Sovetkin, "PEARL TF PV: The long term performance of thin film photovoltaic modules," in: *37<sup>th</sup> European Photovoltaic Solar Energy Conference and Exhibition (EUPVSEC)*, virtual, September 2020, oral presentation.

**K. Bakker**, A. Rasia, S. Assen, B. Ben Said Aflouat, A. Weeber, and M. Theelen, "How the absorber influences the formation of reverse bias induced defects in CIGS solar cells," in: *37<sup>th</sup> European Photovoltaic Solar Energy Conference and Exhibition (EUPVSEC)*, virtual, September 2020, oral presentation.

**K. Bakker**, J. Coll Matas, J. Bosman, N. Barreau, A. Weeber, and M Theelen, "Determining the decomposition voltage of  $\text{Cu}(\text{In}_{1-x}\text{Ga}_x)\text{Se}_2$ ," in: *2022 IEEE 49<sup>th</sup> Photovoltaic Specialist Conference (PVSC)*, Philadelphia, United States, June 2022, oral presentation.

# Dankwoord

Eindelijk na 6 jaar is het boekje dan klaar, ik heb dit niet alleen gedaan en wil iedereen bedanken die hier aan bijgedragen heeft.

Allereerst mijn promotoren en copromotor. **Mirjam**, het was een plezier om met jou te werken. Af en toe kreeg ik het gevoel dat je me bijna hebt opgenomen in je familie, vooral doordat ik tijdens je zwangerschapsverlof op visite kwam om publicaties en andere promotie-gerelateerde zaken door te spreken. **Arthur**, ondanks je drukke agenda heb je altijd tijd voor mij weten te maken. Je had een heel andere rol en de relatie was anders dan met Mirjam, maar jullie vulden elkaar goed aan, zowel qua persoonlijkheid als inbreng van kennis. **Miro**, je was altijd meer op de achtergrond aanwezig. Je hebt me geholpen met de grote lijnen, waarbij je mijn werk vanuit een niet iets andere invalshoek kon benaderen.

Het belangrijkste voor een onderneming zoals dit is het budget, hiervoor moet ik **Yael** (FZ Jülich) bedanken. **Yael**, thank you for initiating and writing the PEARL project proposal, especially your flexibility with the late addition of the TU Delft. This dissertation would not have been possible without the PEARL project.

De beslissing om te gaan promoveren had ik niet genomen zonder de volledige steun van het management van toen nog ECN. **Hans** het was altijd fijn om voor je te werken, vooral je “man op de maan” mentaliteit werkt erg motiverend. Ik weet zeker dat je je nieuwe avontuur bij Carbyon tot een daverend succes weet te brengen. Na de overgang van ECN naar TNO ben ik terecht gekomen in het CIGS team onder leiding van **Hans Linde**. **Hans**, jij had een duidelijke visie voor CIGS en mijn werk paste in dat toekomstbeeld. Behalve **Hans** wil ik natuurlijk ook de andere leden van het CIGS team bedanken, **Hero**, **Robbert**, **Maarten**, **Pieter-Jan**, **Karine**, **Rémi** en **Marcel**. Gedurende de vier jaar heb ik ontzettend leuk met jullie samengewerkt. Jullie hebben altijd interesse getoond in de wormpjes en ik heb van jullie alle steun en hulp gekregen die ik nodig had. Vooral de door **Marcel** op maat gemaakte CIGS processing cursus voor de Graduate School was bijzonder nuttig.

Het onderwerp van mijn onderzoek dank ik aan **Sohey** en **Erik** (RERA Solutions). Tijdens het testen van een prototype elektrische belasting, bedoelt voor het verouderen van CIGS zonnecellen, zijn zij erachter

gekomen dat CIGS cellen niet tegen grote negatieve spanningen bestand waren en waren de eerste wormpjes geboren.

Voor al de eerste twee jaar heb ik regelmatig een dag in de week in Delft gewerkt. Hier heb ik veel geweldige mensen ontmoet, helaas zijn veel promovendi van toen er nu niet meer, omdat ik al bijna vier jaar niet meer in Delft geweest ben. Eerst vanwege corona en later, omdat de vier jaar erop zaten. De CIGS gemeenschap aan de TU Delft is erg klein, **Nasim** en **Johan**, het was fijn om met jullie aan hetzelfde onderwerp gewerkt te hebben. Tijdens conferenties en zomerscholen, ben ik veel opgetrokken met de mensen uit Delft, **Thierry, Andres, David, Arno** en **Patrizio** bedankt voor de het gezelschap tijdens deze reizen. Natuurlijk wil ik ook de technici **Stefaan, Martijn** en **Remco** bedanken voor de vele gesprekken, ik heb met jullie vanwege mijn achtergrond meer gemeen dan met de meeste promovendi. Behalve studenten en technici wil ik ook **Olindo, Rudi, Mark, René, Hesam, Robin, Luana, Paul, Carlos, Paula, Juan Camilo, Guangtao, Can, Gianluca, Jonathan** en **Manvika** bedanken.

Ook heb ik veel te danken aan alle studenten die ik heb begeleid tijdens de promotie, bijna allemaal zijn zij medeauteur van een artikel of conferentiebijdrage. **Paulo** you were my first intern and maybe your mentality is a little too laid back. **Christophe**, I really saw you come to life as your English evolved during your time here, your contribution was very valuable even though it didn't make it into a publication. **Eduardo**, you reminded me that Colombia is more than the legacy of Pablo Escobar. **Alix**, you're a very clever girl. **Hanna** and **Suzanne**, I wish you both a lot of success with your own PhD research. **Basma**, you have a cheerful personality and it was a pleasure having you around. **Kees**, over jou heb ik me nooit zorgen hoeven maken, jij redt het wel. **Joaquin**, too bad the corona ended your stay prematurely, however, without your contribution I would never have finished the chapter on the decomposition voltage.

Verder zijn er ook studenten die ik niet begeleid heb maar die wel een bijdrage hebben geleverd aan mijn onderzoek. **Andrea**, you are very talented and I'm sure you use your talents well at the TU/e. You started the CV measurement and in the end this turned out to be a dead end. **Gabriela** you're work on the modules also didn't make it into this dissertation, however, we had a lot of fun destroying the modules. **Yassine** jouw metingen waren bijzonder nuttig, net als jouw kennis over Marokko en de mensen daar.

Naast studenten hebben ook andere mensen een bijdrage geleverd aan de publicaties in dit boekje, en ook die verdienen een bedankje. **Nicolas**, you where indispensable for this work, I could not have done this without your cells and your valuable knowledge and ideas. **Johan**, bedankt voor het mooie laserwerk, en **Teun** voor de fraaie formule.

Mijn promotie viel binnen twee projecten, PEARL en BIPVPOD, binnen beide projecten was ik een beetje een vreemde eend in de bijt omdat het academisch onderzoek niet helemaal in de projecten paste. Binnen de projecten is mijn onderwerp altijd goed ontvangen en ik vond het belangrijk om ook betrokken te zijn bij het grotere plaatje, de toepassing van PV. Bij deze wil ik alle projectpartners bedanken.

Voor dit promotietraject begon had ik natuurlijk al een lange carrière op het gebied van onderzoek naar zonne-energie. Ik heb met te veel mensen gewerkt die van invloed zijn geweest op mijn passie voor zonne-energie om iedereen persoonlijk te bedanken.

Ik ben begonnen bij ECN in Petten en heb daar veel gepassioneerde mensen ontmoet die hun enthousiasme voor zonne-energie op mij hebben overgedragen. Daar werkte we aan de technologie van de toekomst, met het idee dat PV ooit een grote bijdrage zou leveren aan de energiemix, en nu na bijna 25 jaar begint dit langzaam werkelijkheid te worden. Daarom wil ik iedereen met wie ik in Petten samengewerkt heb bedanken.

Na de verhuizing van ECN naar Eindhoven was er veel meer samenwerking; met TNO, de promovendi van de universiteit Utrecht en de Solliance partners, met name de CIGS groep van IMEC. Jullie hebben allemaal bijgedragen aan mijn beslissing om aan dit avontuur te beginnen, en binnen de samenwerking is er altijd ruimte geweest voor mijn promotieonderzoek. Hier wil ik vooral **Jorne** en **Michaël** van U Hasselt bedanken, het IR filmpje dat ik aan het begin van mijn promotie bij jullie geschoten heb wordt nog regelmatig gebruikt. In Eindhoven heb ik de PV activiteiten zien groeien van het kleine groepje ECN medewerkers uit Petten tot de 44 mensen die vandaag in de STA groep onderzoek doen aan alle aspecten van de zonne-energie. Het is een grote eer om dagelijks met jullie te mogen werken en de passie voor PV te delen.

**Dong** en **Maarten** jullie hebben laten zien dat ware vriendschap onder collega's mogelijk is. **Veronique**, jij bent een beetje de schaduwkoningin van dit boekje. In bijna elk hoofdstuk zijn jouw verbeteringen wel te vinden. Jij en **Suus** hebben me er regelmatig aan moeten herinneren dat het best wel belangrijk was om het boekje af te maken.

Ik ben altijd graag terug gegaan naar Wijdenes, een totaal andere omgeving, even weg van de wormpjes. Lekker biertjes drinken op het terras in Hoorn, of F1 kijken. Ik wil hiervoor mijn vrienden in Wijdenes en omstreken bedanken.

Natuurlijk heb ik ook veel steun gehad van mijn familie, het is altijd goed om weer thuis te zijn. Ondanks dat we daar ook moeilijkere tijden hebben gehad, maar ik weet zeker dat moeders trots zou zijn geweest op dit resultaat. **Pa**, **Thijs** en **Chris**, jullie waren er altijd voor mij, en dat is heel bijzonder.

Klaas Bakker  
Eindhoven juli 2023

# Curriculum Vitae

Klaas Bakker is op 9 juli 1976 geboren in Wijdenes. In 1999 studeerde hij af aan de Hogeschool Alkmaar als ingenieur in de elektrotechniek. Onderdeel van zijn studie was een stage bij het Zuid-Afrikaanse energiebedrijf ESCOM. Na zijn studie kwam Klaas terecht bij het Energie onderzoek Centrum Nederland (ECN) in Petten, waar hij werkte aan het aan onderzoek naar kleurstofzonnecellen. In 2007 heeft hij zich gespecialiseerd in de zonne-energie, en behaalde hij een Master of Engineering Science in Photovoltaic Engineering aan de University of New South Wales in Sydney. Hierna keerde hij terug naar ECN, waar hij naast het werk aan kleurstofzonnecellen zijn werkzaamheden ook uitbreidde naar andere PV technologieën, voornamelijk gericht op meer geavanceerde analyse technieken. Bij de verhuizing van de ECN dunne-film activiteiten in 2010 naar Eindhoven voor het Solliance samenwerkingsverband was Klaas verantwoordelijk voor het opzetten van de karakteriseringsfaciliteiten. In Eindhoven hield Klaas zich voornamelijk bezig met de karakterisering van dunne-film PV, ook heeft hij bijgedragen aan onder andere de realisatie van de eerste vier terminal tandem module en de eerste laminatieproeven van kleine CIGS cellen. Deze werkzaamheden zijn de basis van twee van de pijlers van het huidige onderzoeksprogramma van TNO partner in Solliance, namelijk de onderzoekslijn naar tandem PV technologie en het mass customisation programma. In 2017 is hij begonnen met zijn promotiewerk, waarvoor hij twee dagen per week in dienst was bij de TU Delft. De resultaten van zijn promotieonderzoek staan beschreven in dit proefschrift en zijn gepresenteerd op diverse internationale conferenties. Tegenwoordig werkt Klaas nog steeds bij TNO partner in Solliance. Hij is betrokken bij de ontwikkeling van dunne-film PV, en daarnaast past hij zijn ervaring met reverse bias op CIGS uit dit proefschrift nu toe op perovskiet cellen en modules.





